ABSTRACT

Title of dissertation: Characterization and Application of Angled Fluorescence Laminar Optical Tomography

Chao-Wei Chen, Doctor of Philosophy, 2013

Directed By: Professor Yu Chen,
Fischell Department of Bioengineering

Angled fluorescence laminar optical tomography (aFLOT) is a modified fluorescence tomographic imaging technique that targets the mesoscopic scale (millimeter penetration with resolution in the tens of microns). Traditional FLOT uses multiple detectors to measure a range of scattered fluorescence signals to perform 3D reconstructions. This technology however inherently assumes the sample to be scattering. To extend the capability of FLOT to cover the low scattering regime, the oblique illumination and detection was introduced. The angular degree of freedom for the illumination and detection was theoretically and experimentally investigated. It was concluded that aFLOT enhanced resolution 2.5 times and depth selectivity compared to traditional FLOT, and that it enabled the stacking representation, a process that skips the computationally-intensive reconstruction usually needed to render the tomogram. Because stacking is enabled, the necessity of a reconstruction process is retrospectively discussed. aFLOT systems were constructed and applied in tissue engineering. Phantoms and engineered tissue models were successfully imaged. The aFLOT was shown to perform non-invasive *in situ* imaging in biologically

relevant samples with 1mm penetration and 9-400 micron resolution, depending on the scattering of samples. aFLOT illustrates its potential for studying cell-cell or cell-material interactions.

Characterization and Application of Angled Fluorescence Laminar Optical Tomography

By

Chao-Wei Chen

Dissertation submitted to the Faculty of the Graduate School of the
University of Maryland, College Park, in partial fulfillment
of the requirements for the degree of
Doctor of Philosophy
2013

Advisory Committee:
Professor Yu Chen, Chair
Professor Chi H. Lee
Professor Christopher Davis
Professor Pamela Abshire
Professor John Fisher
Professor Julius Goldhar

Preface

Chapter 1 introduces fluorescence imaging, and 3 common parameters for evaluating a mesoscopic imaging system. Chapter 1 also covers the previous study, the first OCT-FLOT integration, which was done exclusively in Dr. Chen's lab back in early 2009.

Chapter 2 walks through the linear theory of aFLOT. Only the details necessary to understand my contribution are covered. For example, the expectation-maximization, one non-linear algorithm for the reconstruction, is not covered even though I still implemented it during my PhD training. I will show a brief comparison that both the linear and non-linear reconstruction gave comparable tomogram, justifying the linear approach is applicable. Chapter 2 is intended to be self-contained. In the end, I hope I can provide a comprehensive starting point for the reader.

Having described the basics of aFLOT, I add my own contribution in Chapter 3, which explores the angular degree of freedom in the illumination and detection of the optics. I will discuss the optimization of the angle FLOT (aFLOT) using Monte-Carlo simulation and singular value analysis. Chapter 3 also covers the instrumentation and data acquisition of aFLOT.

Chapter 4 details the experimental characterization of aFLOT images. Well-designed phantoms were fabricated and imaged. Resolution, penetration depth, and sensitivity against scattering and penetration depth were characterized.

Chapter 5 details the application of aFLOT in tissue engineering. aFLOT successfully resolved 3D human mesenchymal stem cell (hMSC) distribution in engineered tissue models. This advance demonstrates the potential of aFLOT to perform a non-invasive in situ imaging, compared to laborious and destructive cryo-sectioning of an imaged sample.

Chapter 6 concludes the thesis by summarizing the keynote about aFLOT. My contribution is shortly repeated and itemized in section 2. Section 3 closes the thesis by laying out some future directions.

Dedication

To my parents, Kuo-Lieh Chen and Yu-Huei Chen.

Acknowledgements

I have to thank my girlfriend, Hui-En Chen, for her firm belief that I must pursue my PhD in the United States and for her unintermittent company. The path we chose together is proven right in that I grew maturely both in doing research and responding properly to people and things. I have to thank my parents for their unconditional support. My Mom is a believer of “no news is good news”. For that, I have to specially thank my Dad for taking care of Mom for me. I thank Dr. Chi-En Yin for being a foxy older brother. His critical thinking made me doubt EVERY thing, turning my world so twisted, complicated, yet interesting!

I have to thank Dr. Yu Chen for being an adviser who tolerates my absent-minded errors, who pays attention to student’s personal need, who is responsive to questions, who is willing to help students build their career, and who is bold to let students manage multiple projects. Trying to be productive in every project was once frustrating, but I gained so much experience in managing time and resource. (I truly hope no huge delay has occurred.) The training I received in the Fischell department of bio-engineering is the emphasis on the interdisciplinary connection among the basic sciences, academia, industry and the clinics. That was one of the America image I acquired. I thank Dr. Shuai Yuan for paving the early work of FLOT. His establishment brought me comfort, confidence, and belief so today I can establish my contribution.

In the project of tissue engineering, I thank Dr. John Fisher for his generous, continuous support in meeting our imaging need. Dr. Martha Betz, Dr. Andrew Yeatts, Dr. Emily

Coats, Martha Wang, Bao Nguyen, Kimberly Ferlin, Dr. Jianting Wang and I were a team play undoubtedly.

In the project of PSF characterization, I was fortunately able to intern at FDA, thanks to Dr. Chen. Dr. Joshua Pfefer, Anant Agrawal, Anthony Fouad, and Jigesh Baxi, exemplified the rare experience of regulatory sciences.

I thank the committee of my defense: Dr. Yu Chen, Dr. Chi Lee, Dr. Julius Goldhar, Dr. Christopher Davis, Dr. Pamela Abshire, and Dr. John Fisher. Your comments complete this thesis and will inspire the future.

Table of Contents

Preface ii
Dedication iv
Acknowledgements v
Table of Contents vii
List of Figures x
1 Introduction 1

1.1 Resolution, contrast, and penetration depth 1
1.2 Fluorescence imaging 4
1.3 Multi-modal OCT-FLOT system 8

1.3.1 Result: Phantom Experiments 9
1.3.2 Result: Subsurface Cancer Imaging 10

2 Theory of Fluorescence Laminar Optical Tomography and Local Image Reconstruction 12

2.1 Radiance and the Radiative transport equation 12

2.1.1 Radiance $\boldsymbol{L}$ is the unknown to solve for 12
2.1.2 Radiative transfer equation (RTE) 14
2.1.3 Diffusion equation 16
2.1.4 Examples: Impulse responses in an infinite scattering medium 17
2.1.5 Units 19

2.2 Modes of operations: TD vs. FD 19
2.3 Linear image reconstruction 20

2.3.1 Linear relationship between fluorescence and fluorophore distribution 20
2.3.2 The method of least squares 25
2.3.3 Discrepancy principle and L-curve 27
2.3.4 The hard constraint 30
2.3.5 Stacking representation 31
2.3.6 Revisit RTE: the angular degree of freedom 37

2.4 Monte-Carlo simulation 39

2.4.1 Introduction 39
2.4.2 Implementing the weight matrix using MC simulation 40

2.5 Comparing different reconstruction approaches 43
2.6 Formation of the tomogram 44
2.7 Summary 46

3 The Angular Degree of Freedom: Simulation and Implementation 48

3.1 Qualitative explanation of the effect of oblique illumination/collection 48
3.2 Measurement Configurations 51
3.3 Singular Value Analysis (SVA) 53
3.4 PSF simulation 58
3.5 Instrumentation 60
3.6 Data acquisition 64
3.7 Other measurement configurations 66
3.8 Summary 68

4 Experimental Characterization of aFLOT 70

4.1 Capillary tube phantom in 1% Intralipid: comparing aFLOT with FLOT 71
4.2 Capillary in homogeneous medium (Intralipid) 72
4.3 Layered PEG hydrogel 76
4.4 Capillary in homogeneous PEG 78
4.5 Capillary in macroporous PEG 80
4.6 PSF phantoms 82

4.6.1 Scattering effect on resolution and intensity 85
4.6.2 The effect of the iris opening on resolution and intensity 86

4.7 Summary 87

5 Application of aFLOT: Tissue Engineering 89

5.1 hMSCs embedded in PEG 89
5.2 hMSCs seeded on macroporous (heterogeneous) PEG 92
5.3 hMSCs sandwiched between two macroporous (heterogeneous) PEGs 94
5.4 hMSCs in alginate beads 97
5.5 Summary 101

6 Conclusion 103

6.1 A unified system 103
6.2 Contribution 104
6.3 Future work 105

Appendix 106
1 Interface of aFLOT data acquisition 106
2 Achieving tomographic imaging through out of focus aberration and apodization 108

2.1 Motivation 108
2.2 Physics understanding 109
2.3 Mathematics formulation 110
2.4 Examples 114

2.4.1 Verify the prediction of geometric optics. 114
2.4.2 Out-of-focus aberration and sufficiently large aperture....114
2.4.3 Fourier transform pair (in sufficiently large aperture)....115
2.4.4 4f configuration with sufficiently large aperture. Planar object in focus. .116
2.4.5 4f configuration with finite aperture. Planar object in focus 116
2.4.6 4f configuration with sufficiently large aperture. Planar object out-of-focus116
2.4.7 4f configuration with finite aperture. Planar object out-of-focus 117
2.4.8 Two point objects at different depths....117
2.4.9 Useful formula 118

2.5 Conclusion....118

Bibliography 119

List of Figures

Figure. 1 Multi-scale biomedical imaging modalities and platforms for multimodal imaging (indicated by "⇔"). [7].....2
Figure. 2 Co-registration of OCT and line-scan FLOT of a capillary tube filled with fluorescence dye. [8].....10
Figure. 3 OCT/FLOT of subcutaneous human breast tumor xenograft on mouse model in vivo. [7].....11
Figure. 4 Illustration of Equ.9.....23
Figure. 5 Illustration of the best regularization parameter using the L-curve criterion. [2]30
Figure. 6 Geometrical determination of the depth of fluorescence object.....35
Figure. 7 Example of dictating depth from 2D image. 36
Figure. 8 Comparison between stacking representation (A, C) and the reconstruction (B, D). 37
Figure. 9 The line illumination simulated by MCX.....42
Figure. 10 Monte-Carlo simulated measurement sensitivity distribution of FLOT measurements (log scale). [8] 43
Figure. 11 Compare stacking, Tikhonov, SIRT, and EM. 44
Figure. 12 Illustration of illumination (solid lines) and collection (dashed lines) cones for normal- and oblique-incidence geometries. 50
Figure. 13 Sensitivity maps (in log10 scale) for source-detector pair with 0^o (top row) and 30^o (bottom row) incidence/detection angles. [4] 56
Figure. 14 Comparison of singular value (SV) distributions among different incidence/detection angles. [4].....57
Figure. 15 the peak intensity and iterquartile range of PSFz verses depths. 60
Figure. 16 Schematic and photo of two aFLOT systems.....64
Figure. 17 30° configuration vs. 0° and angle compounding configurations.....68
Figure. 18 Comparing the reconstructed capillary cross-section using aFLOT (A,C) and conventional FLOT (B,D). [6] 72
Figure. 19 detectability of the capillary cross-section vs. scattering and depth. 76
Figure. 20 Cross-section of a layered PEG hydrogel.....77
Figure. 21 Co-registration of OCT and line-scan aFLOT of a capillary tube filled with fluorescence dye ICG.....80
Figure. 22 Imaging capillary tube through heterogeneous PEG.....82
Figure. 23 Unstructured fluorescent microsphere distribution. 84
Figure. 24 Resolution (FWHM) and intensity vs. depth, scattering, and iris opening. 85
Figure. 25 3D aFLOT imaging of PEG hydrogels with stem cells embedded at top layers.92
Figure. 26 hMSCs on the macroporous PEG.....94
Figure. 27 Diffused fluorescence.....96
Figure. 28 hMSCs sandwiched between two macroporous PEGs.....97
Figure. 29 Alginate beads at day 0 and day 21 100
Figure. 30 compare the image by fluorescence microscopy (A) and aFLOT (B). 101

1 Introduction

In the field of imaging, resolution, contrast, and penetration depth are among the most common parameters for evaluating imaging systems. In section 1.1, I summarize the history, definition, and measurement of those parameters. In section 1.2, I briefly state the history, advantages, disadvantages, and principles of fluorescence imaging. Sections 1.1 and 1.2 outline a way to categorize the fluorescence imaging according to the size of the objects being observed. Historically, imaging has focused on microscopy and later on macroscopy. The mesoscopic middle ground is rarely explored, yet is important because it provides a link between extreme local fragmentation and global unity. The application in chapter 5 shows its unique advantage in studying the cell-cell or cell-material interactions. In section 1.3, the previous work done in our lab by Dr. Yu Chen and Dr. Shuai Yuan was briefed; one aim of this thesis is to improve upon the previous work.

1.1 Resolution, contrast, and penetration depth

Resolution and contrast have been the two most critical parameters for evaluating 2D imaging systems. It was not until 1895, the year in which Wilhelm Röntgen discovered and systematically studied X-rays, that the need for 3D imaging became apparent. Clinical motivations such as the desire to avoid invasive medical procedures into the human drove the development. The first 3D imaging technique was X-ray computed tomography, which was intensively developed in the early 1900s. Since then, other 3D

imaging techniques prospered, such as MRI and ultrasonic tomography, both of which were developed in the 1950s. Tomography refers to imaging by sections, through the use of any kind of penetrating wave. The range of depth sectioning, termed penetration depth, became the third most important parameter for evaluating (3D) imaging systems. Depending on their resolution and penetration depth, imaging technologies can now be categorized into macroscopic, mesoscopic, and microscopic scales. Figure. 1 illustrates some multi-scale biomedical imaging modalities and platforms.

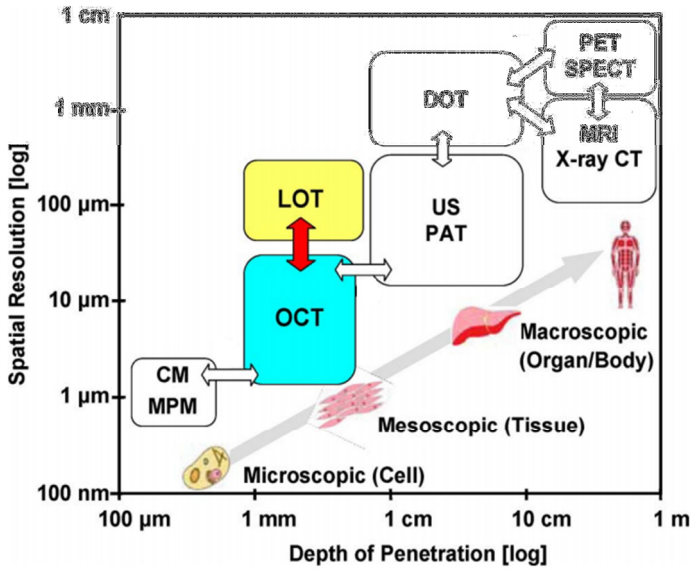

Figure. 1 Multi-scale biomedical imaging modalities and platforms for multimodal imaging (indicated by "⇔"). [7]

PET: positron emission tomography; SPECT: single-photon emission computerized tomography; MRI: magnetic resonance imaging; X-ray CT: X-ray computerized tomography; DOT: diffuse optical tomography; US: ultrasound; PAT: photo-acoustic tomography; OCT: optical coherence tomography; LOT: laminar optical tomography; CM: confocal microscopy; and MPM: multi-photon microscopy.

Resolution describes the ability of an imaging system to resolve detail in the object that is being imaged. Resolution is usually measured by the point-spread function (PSF) of the imaging system. The most common historical criterion (as the focus was on 2D microscopes) was suggested by Rayleigh. Rayleigh's criterion states "two point sources are regarded as just resolved when the principal diffraction maximum of one PSF coincides with the first minimum of the other." As a result, the dip formed by the two separated PSFs is about 26% and the corresponding separation (resolution) is $0.61\frac{\lambda}{\mathrm{NA}}$. The formula, involving the wavelength and the numerical aperture, is a diffraction-limited estimate of resolution.

An alternative to estimate resolution is to use full-width-half-maximum (FWHM) of the PSF. It disregards the imaging scale and is more general because in fact some PSFs do not have first minimum and because the PSF is a summary of both diffraction and aberration. At macroscopic and mesoscopic scales, where diffraction is irrelevant, it appears that only this FWHM alternative is a well-defined measure of resolution. At microscopic scales where diffraction dominates, the FWHM of a PSF is comparable to Rayleigh's criterion. Furthermore, for current imaging technologies such as super-resolution, many of which break down the diffraction limit, the FWHM of a PSF is repeatedly used in the literature.

One another measure of resolution is inter-quartile range (IQR), which represents the range that bounds an area of 50% centered around the maximum value under the PSF

curve. IQR provides a more stable estimate of spread than FWHM in the presence of a long tail distribution [9]. In this thesis, I use the FWHM or IQR of a PSF as the resolution.

Contrast is the difference among luminance, phase, wavelength (color), and polarization of electromagnetic light that makes an object representing in an image distinguishable. There are several origins of optical contrast. Bright field illumination obtains contrast from absorbance of light in the sample. Cross-polarized light illumination obtains contrast from rotation of polarized light through the sample. Dark field illumination obtains contrast from light scattered by the sample. Phase contrast illumination obtains contrast from interference of different path lengths of light through the sample. In this thesis, a fluorescence technique is used to obtain contrast. Fluorescence technique essentially recognizes that the wavelength of signal can be exclusively designed and selected.

Penetration depth was introduced after the advent of 3D imaging techniques. Current convention considers a good 3D imaging system to be one which maintains depth-to-resolution ratio >100. [10]

1.2 Fluorescence imaging

The history of fluorescence is as long as that of optics, dating back to the 15th century. It was however not until the 20th century that fluorescence and optics were combined. In 1911-1913, the first auto-fluorescence microscope was developed by Otto Heimstaedt and Heinrich Lehmann.

In addition to absorption, scattering, phase, and polarization, fluorescence takes a fundamentally different approach to provide contrast. Although the intensity of fluorescence is usually 1000 times lower than that of reflection, an emission filter able to reject unwanted wavelengths by 6 orders makes this alternative possible. What makes this approach useful is the variety of available fluorescent dyes that target particular components of complex biomolecular assemblies and functions. In 1994, when M. Chalfie et al. succeeded in expressing a naturally fluorescent protein, the now-famous green fluorescent protein (GFP), in living organisms, a whole new class of labeling methods makes fluorescence imaging indispensable[11]. On the other hand, photobleaching and phototoxicity are two limitations of fluorescence imaging. After a long exposure to incident light, photobleaching denatures fluorophores, which then lose their ability to fluoresce. This phenomenon may severely limit the time over which a sample can be imaged. Phototoxicity is an adverse effect due to exposure to the intensive light. Fluorescent molecules may further generate reactive chemical species when under illumination which enhances the phototoxic effect.

All fluorescence imaging techniques follow similar principles. A sample is illuminated with light of a wavelength which excites fluorescent molecules in the sample. The relaxation of the excited molecules releases energy that is either thermally dissipated or radiatively emitted. The latter is recognized as either fluorescence (spin transition allowed) or phosphorescence (spin transition forbidden). The remitted energy must be smaller than the exciting energy. Therefore, fluorescence is at a longer wavelength than

the illumination source. After passing an emission filter that exclusively select the fluorescing wavelength, fluorescence is detected by the detector.

If categorized by scales, fluorescence microscopes use techniques including confocal, multi-photon, structured light illumination, temporal focusing, and selective plane illumination to achieve and improve sub-micron resolution and sub-millimeter penetration depth. Fluorescence confocal microscopy (FCM) uses a pinhole to reject off-axis focused signals. Multiphoton microscopy (MPM) uses high intensity light to generate an appreciable nonlinear effect to excite fluorophores, further enhancing both resolution and penetration depth, compared to CM, because of the typically lower scattering in biological samples in near infrared light. Common CM and MPM techniques rely on scanning an optical probe point to form a tomogram, which limits the acquisition speed. Structured light illumination projects grid patterns onto the objects by recognizing that optical sectioning strength depends on particular spatial frequency. Temporal focusing uses a pulse laser to achieve optical sectioning. Light-sheet/selective plane illumination takes an instrumentation approach by separating the illumination arm from the detection arm.

Macroscopically, diffuse optical tomography (DOT) captures the multi-scattered fluorescence from the sample surface and uses it to reconstruct the intensity and distribution of fluorophores within the sample, typically yielding 3D spatial resolution on the order of millimeters and penetration depths of several centimeters.

Based on the same idea, a family of fluorescent mesoscopic imaging technologies has been designed, including fluorescence molecular tomography [12], mesoscopic epi-fluorescence tomography [13], and fluorescence laminar optical tomography (FLOT) [14-16], each targeting a slightly different regime of resolution and penetration depth. Unlike CM, FLOT uses an array of detectors with different separation from the source, each of which simultaneously records scattered fluorescence, which is weighted differently at each depth. FLOT uses reconstruction, a post-processing procedure, to render depth-resolved information. However, the typical source-detector separations in FLOT are much shorter (typically a few millimeters) than those in DOT. FLOT can therefore yield higher resolution than DOT. FLOT established a >2mm penetration depth and a 100-200 micron resolution when imaging a rat cortex. Capillary phantoms have also been used to characterize FLOT, showing that the FWHM of the axial PSF increases as depth increases. Previous work in Dr. Chen's lab indicates an axial FWHM of 400-500 micron at 1-mm depth.

In this thesis, I focus on using the angular degree of freedom to improve resolution and penetration depth, theoretically in chapter 3 and experimentally in chapter 4. The framework of traditional FLOT is however required and is described in chapter 2. Before proceeding, it is worthwhile to mention our previous work in the next section. Dr. Chen's lab is the first lab that developed the multi-modal optical coherence tomography (OCT) - FLOT system in 2009 [8]. My angle FLOT improves upon this previous work.

1.3 Multi-modal OCT-FLOT system

Multi-modal optical imaging techniques offer a more comprehensive understanding about the imaged subject. The development has been focused on tomographic imaging, co-registering tomograms, and performing simultaneously combined imaging. Usually, one modality performs high resolution structural imaging, and the other monitors the molecular, biochemical, or metabolic function. Being able to simultaneously acquire such complementary information about the imaged subject is beneficial because the merged imaging procedure would simplify the patient/hospital workflow. More, complementary information provides more accurate diagnosis and therapy.

The synergy has evolved from offering complementary information to refining image reconstruction. For biomedical applications, by interpreting the structural and functional images simultaneously, one is able to attain a diagnostic accuracy which may be not achievable by each individual modality. For example, in animal studies, fluorescence-guided OCT demonstrated that the specificity of fluorescence detection of transitional cell carcinoma was significantly enhanced (53% vs. 93%), and the sensitivity of fluorescence detection also improved by combination with OCT (79% vs. 100%) [17].

In this section, the combination of OCT and FLOT as a mesoscopically co-registered structural and molecular imaging platform is introduced (the red "⇔" in Figure. 1). OCT is primarily based on contrasts from the scattering, birefringence, and refractive index variations of the tissue, providing resolution of 1-10 μm and penetration depth of 1-2mm within tissue micro-structures. Complementarily, FLOT provides highly-sensitive

molecular information through the use of fluorescence contrast agents [16, 18]. Their comparable imaging scales and complementary contrast mechanisms motivated the integration of OCT and FLOT.

1.3.1 Result: Phantom Experiments

The performance of the OCT-FLOT system was first demonstrated by imaging a tissue phantom[8], which consisted of a capillary tube suspended in a scattering medium. The capillary tube (100 μm inner diameter and 125 μm outer diameter) was filled with fluorescent dye (10 μM Cy5.5). The scattering medium was 2% Intralipid with Indian ink ($\mu_a = 0.2\ \mathrm{mm}^{-1}$, $\mu_s = 7.2\ \mathrm{mm}^{-1}$ at 670 nm, anisotropy factor $g = 0.9$), which is similar to human skin tissue. This tissue phantom was designed to provide contrasts for both OCT and FLOT. For OCT, the contrast was from the scattering medium and the glass walls of the capillary tube; for FLOT, the contrast was from the Cy5.5. The wavelengths of the illumination source, dichroic mirrors, and filters in FLOT were chosen based on the optical properties of Cy5.5. They can be adapted to other fluorescent dyes.

Figure. 2 shows the comparison of OCT and FLOT images of the capillary tube phantom. OCT readily imaged the 3D structure of the tube as shown in (A). Figure. 2 (B, C, D) show the comparison of OCT cross-sectional image (YZ) and FLOT image at location "1", "2", and "3" denoted in (A) respectively. Observations include: First, the FLOT image of the capillary cross-section at deeper location was larger in size, indicating the resolution degraded. Second, the FLOT image (XZ) revealed a similar contour of the capillary tube as that shown by OCT. OCT and FLOT images were well co-registered at

least deep to 1mm. Third, the reconstructed intensity was nearly constant, which agrees with the fact that fluorophore concentration in the capillary should be uniform.

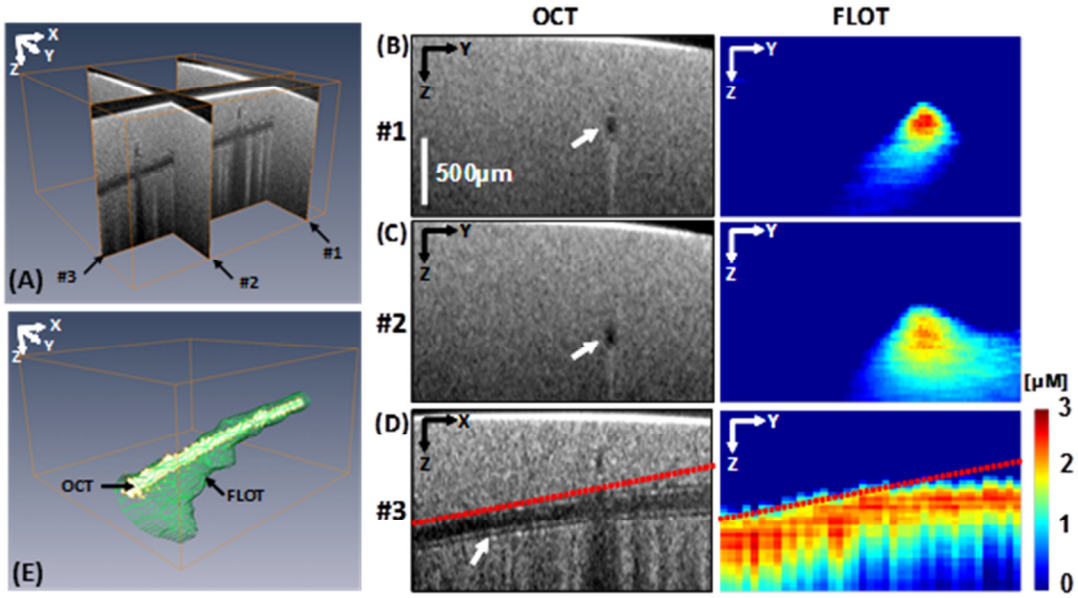

Figure. 2 Co-registration of OCT and line-scan FLOT of a capillary tube filled with fluorescence dye. [8]

1.3.2 Result: Subsurface Cancer Imaging

Using the same system, a human breast cancer xenograft animal model of cell line, MDA-MB-231, was labeled by tdTomato dye for *in vivo* OCT-FLOT imaging. [7]

Figure. 3(A, E) show an OCT cross-sectional image of the breast tumor. The high scattering of mouse skin layer limited the penetration depth. The boundary between the skin and the tumor remained visible in A while the boundary was less well-defined in E indicating tumor invasion. (B, F) show the co-registered FLOT image revealing the subcutaneous tumor with exclusively high sensitivity at least 1.5mm below the surface. (C, G) show the fused OCT-FLOT image which shows the relative position and

distribution of tumor regions underneath the skin. (D, H) show the corresponding histology confirming the presence of a tumor. (I) shows the 3D view of mouse skin (from OCT) and subsurface tumor (from FLOT).

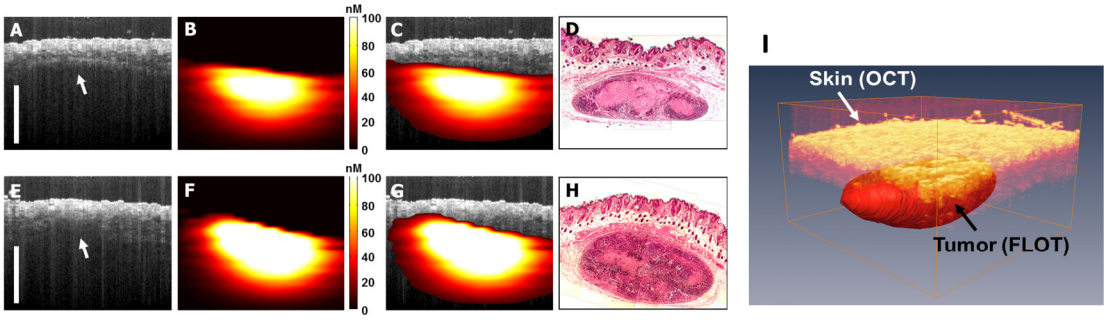

Figure. 3 OCT/FLOT of subcutaneous human breast tumor xenograft on mouse model in vivo. [7]

Breast cancer cells (MDA-MB-231) were constitutively labeled with tdTomato red fluorescence protein. Bar: 1 mm.

In sum, the OCT image provided the structural information of the phantom and the FLOT reconstructed image provides the fluorescence fluorescence-dye-targeted molecular information. Together, the hybrid OCT-FLOT system showed the concurrent depth-resolved tissue-structural and molecular imaging.

2 Theory of Fluorescence Laminar Optical Tomography and Local Image Reconstruction

The radiative transport equation (RTE)[1] is derived, as is its frequency domain application under monochromatic light operation. In addition, linear image reconstruction is discussed. Two extreme cases (high and low scattering) are considered first. Simplification of linear image reconstruction can be made for each. Then I will cover the general case where Monte-Carlo simulation comes into the picture. The developed theory is general for 3D reconstructions. Because line illumination was implemented, the reconstruction process was simplified to generate 2D images representing ZX local cross-sections of the sample. The formation of the global 3D tomogram was accomplished by a tiling process.

Two good references are Chapters 5 and 11 in Dr. Li-Hong Wang's Biomedical Optics: Principles and Imaging, and Dr. David Boas' PhD thesis.

2.1 Radiance and the Radiative transport equation

2.1.1 Radiance *L* is the unknown to solve for

For general purposes, physicists like to define fundamental physical quantities such as the density of a material rather than the particular mass of a material because the latter requires one to specify the amount of the material, while the former is a constant. A

[1] Also known as radiative transfer equation or Boltzmann equation.

quantity that can be kept more constant is more desirable. In the RTE, the most fundamental quantity is spectral radiance L_v, defined as the energy flow per normal area per unit solid angle per unit time per unit temporal frequency bandwidth. In practice, since experiments are usually performed with specific range of wavelength Δv, radiance $L = L_v \Delta v = \frac{dE}{dA\, d\Omega dt}$ (unit = $W/m^2 sr$) is a scalar quantity that is more accessible. In fact, the RTE is all about solving for L. When facing challenging differential problems such as RTE, a routine trick is to decompose/expand L by a convenient basis, in a hope that the analysis becomes feasible. In the mesoscopic regime, light propagates in scales of tens to hundreds of mm while the size of fluorophores is measured in microns. That fluorophores are relatively sparse and light propagates isotropically makes spherical coordinates the best description for RTE. Therefore, one can decompose *L* by spherical harmonics:

$$L(\vec{r}, \hat{s}, t) = \lim_{l \to \infty} \sum_{n=0}^{l} \sum_{m=-n}^{n} L_{n,m}(\vec{r}, t) Y_{n,m}(\hat{s})$$

where $\hat{s} = (sin\theta cos\phi, sin\theta sin\phi, cos\theta)$ in Cartesian coordinates. The zero-th and first moments are of particular interests at least for one reason that they, by themselves, sufficiently describe the diffusion approximation. Because the diffusion approximation goes up to the first order moment, it is also known as the P_1 approximation[2]. The zero-th moment is called fluence rate (or intensity) ϕ, and the first moment is called current

[2] P means Legendre polynomials.

density $\vec{J}$. While both have the same unit (W/m^2), ϕ is scalar and $\vec{J}$ is a vector. The operational formula needed to extract ϕ and $\vec{J}$ from L is

$$\begin{cases} \phi(\vec{r},t) = \int_{4\pi} L(\vec{r},\hat{s},\mathrm{t})\, d\hat{s} = \int_{\theta=0}^{\pi}\int_{\phi=0}^{2\pi} L(\vec{r},\hat{s},\mathrm{t}) sin\theta d\theta d\phi \\ \vec{J}(\vec{r},t) = \int_{4\pi} \hat{s}L(\vec{r},\hat{s},\mathrm{t})\, d\hat{s} = \int_{\theta=0}^{\pi}\int_{\phi=0}^{2\pi} \hat{s}L(\vec{r},\hat{s},\mathrm{t}) sin\theta d\theta d\phi \end{cases}$$

Under the diffusion approximation,

Equ.1 $$L(\vec{r},\hat{s},t) \approx \left(L_{0,0}(\vec{r},t)Y_{0,0}(\hat{s})\right) + \left(L_{1,-1}(\vec{r},t)Y_{1,-1}(\hat{s}) + L_{1,0}(\vec{r},t)Y_{1,0}(\hat{s}) + L_{1,1}(\vec{r},t)Y_{1,1}(\hat{s})\right) = \frac{1}{4\pi}\phi(\vec{r},t) + \frac{3}{4\pi}\vec{J}(\vec{r},t)\cdot\hat{s}$$

As alternatives to $L(\vec{r},\hat{s},\mathrm{t})$, other equivalent quantities include

1. $L(\vec{r},\hat{s},\mathrm{t})/v$ (Jm^{-3}): Energy density, the propagating energy per unit volume per unit solid angle. v is the speed of light the media.
2. $L(\vec{r},\hat{s},\mathrm{t})/vh\nu$ (m^{-3}): Photon density, the number of propagating photons per unit volume. Note however this expression is valid only if light is monochromatic.

2.1.2 Radiative transfer equation (RTE)

The change in energy in every volume element within the solid angle element per unit time is $\mathrm{dP} = \frac{\partial L(\vec{r},\hat{s},\mathrm{t})/v}{\partial t} dV d\hat{s}$. Energy conservation requires that this change equal the balance of 4 other factors:

Equ.2 $$dP = -dP_{div} - dP_{ext} + dP_{sca} + dP_{src}$$

$dP_{div} = \hat{s} \cdot \nabla L(\vec{r}, \hat{s}, \mathrm{t}) d\Omega dV = \nabla \cdot [L(\vec{r}, \hat{s}, \mathrm{t})\hat{s}] d\hat{s} dV$ addresses the divergence of the local photon beam. $dP_{div} = 0$ if the beam is collimated. $dP_{div} > 0$ if the beam diverges, and $dP_{div} < 0$ if the beam converges.

$dP_{ext} = (\mu_t ds)[L(\vec{r}, \hat{s}, \mathrm{t}) dA d\hat{s}] = \mu_t L(\vec{r}, \hat{s}, \mathrm{t}) dV d\hat{s}$ addresses the extinction of photons, or the energy loss. $\mu_t ds$ represents the probability of extinction (by either scattering or absorption) in a distance ds. $dP_{ext} > 0$ means energy is lost.

$dP_{sca} = (\mu_s dV) d\hat{s} \int_{4\pi} L(\vec{r}, \hat{s}', \mathrm{t}) P(\hat{s}', \hat{s}) d\hat{s}'$ addresses the energy incident on the volume element dV from any direction $\hat{s}'$ and scattered into $d\hat{s}$ around direction $\hat{s}$. $P(\hat{s}', \hat{s})$, the so-called phase function, is a probability density function: $\int_{4\pi} P(\hat{s}', \hat{s}) d\hat{s}' = 1$. If the phase function only depends on the angle between $\hat{s}$ and $\hat{s}'$, $P(\hat{s}', \hat{s}) = P(\hat{s}' \cdot \hat{s})$, where $\hat{s}' \cdot \hat{s}$ is the directional cosine. Physically, this means scattering depends only on the change in direction of the photon. The scattering anisotropy is $\int_{4\pi} (\hat{s}' \cdot \hat{s}) P(\hat{s}' \cdot \hat{s}) d\hat{s}' \equiv g$, which ranges from -1 to 1. $g = 1$ means photons simply travel forward (from $\hat{s}'$to $\hat{s}'$) as if they were not scattered. $g = -1$ means photons travel backward (from $\hat{s}'$to -$\hat{s}'$). $g = 0$ means photons scatter evenly in every direction, or isotropically.

$dP_{src} = S(\vec{r}, \hat{s}, \mathrm{t}) dV d\hat{s}$ accounts for the energy produced by a source in certain volume element within the solid angle element per unit time. $S(\vec{r}, \hat{s}, \mathrm{t})$ has units $\mathrm{W/m^3}sr$

Dividing Equ.2 by $dV d\hat{s}$ gives

Equ.3

$$\frac{\partial L(\vec{r},\hat{s},t)/v}{\partial t} = -\hat{s}\cdot\nabla L(\vec{r},\hat{s},t) - \mu_t L(\vec{r},\hat{s},t) + \mu_s \int_{4\pi} L(\vec{r},\hat{s}',t)P(\hat{s}',\hat{s})d\hat{s}' + S(\vec{r},\hat{s},t)$$

This is the so-called radiative transfer function.

2.1.3 Diffusion equation

Under the diffusion approximation ($\mu_s' \gg \mu_a$), the RTE degenerates into the diffusion equation. In Equ.1, $L(\vec{r},\hat{s},\mathrm{t})$ is decomposed to $\phi(\vec{r},t)$ and $\vec{J}(\vec{r},t)$. Here, the source $S(\vec{r},\hat{s},\mathrm{t})$ is decomposed to the same order: $S(\vec{r},\hat{s},\mathrm{t}) = \frac{1}{4\pi}S_0(\vec{r},\mathrm{t}) + \frac{3}{4\pi}\overrightarrow{S_1}(\vec{r},\mathrm{t})\cdot\hat{s}$. Therefore, after substituting Equ.1 into Equ.3, one may intermediately obtain

Equ.4 $$\frac{1}{v}\frac{\partial\phi(\vec{r},t)}{\partial t} + \mu_a\phi(\vec{r},t) + \nabla\cdot\vec{J}(\vec{r},t) = S_0(\vec{r},t)$$

Equ.5 $$\frac{1}{v}\frac{\partial\vec{J}(\vec{r},t)}{\partial t} + (\mu_a+\mu_s')\vec{J}(\vec{r},t) + \frac{1}{3}\nabla\phi(\vec{r},t) = \overrightarrow{S_1}(\vec{r},t)$$

Where $\mu_s' = \mu_s(1-\mathrm{g})$ is referred to as the reduced scattering coefficient. Because $\phi(\vec{r},t)$ and $\vec{J}(\vec{r},t)$ appear in both Equ.4 and Equ.5, it is intended to decouple Equ.4 and Equ.5 for $\phi(\vec{r},t)$. Strategically, one can differentiate Equ.4 with respect to t and substitute $\frac{\partial\vec{J}}{\partial t}$ using Equ.5 to obtain:

$$-\nabla\cdot\left[\vec{J} + \mathrm{D}\nabla\phi\right] = -\underbrace{\frac{3D}{v}\left[\mu_a\frac{\partial\phi}{\partial\mathrm{t}} + \frac{1}{v}\frac{\partial^2\phi}{\partial\mathrm{t}^2}\right]}_{\sim 0\ if\ \mu_s'\gg\mu_a} + \underbrace{\frac{3D}{v}\left[\frac{\partial S_0}{\partial\mathrm{t}} - v\nabla\cdot\overrightarrow{S_1}\right]}_{=0\ if\ S\ is\ isotropic}$$

Where $\mathrm{D} = \frac{1}{3(\mu_a+\mu_s')}$ is referred to as the diffusion coefficient. All terms on the right-hand side are small under the diffusion approximation. Note the special case $\vec{J} + \mathrm{D}\nabla\phi = 0$ is Fick's law, and using Equ.4:

$$-\nabla \cdot \left[\vec{J} + \mathrm{D}\nabla\phi\right] = \frac{1}{v}\frac{\partial\phi}{\partial \mathrm{t}} + \mu_a\phi - \nabla \cdot [\mathrm{D}\nabla \cdot \phi] - \mathrm{S}_0$$

Therefore, if $-\nabla \cdot \left[\vec{J} + \mathrm{D}\nabla\phi\right] = 0$, we arrive at the diffusion equation:

Equ.6 $$\frac{1}{v}\frac{\partial\phi}{\partial t} + \mu_a\phi - \nabla \cdot [D\nabla \cdot \phi] = S_0$$

If the diffusion coefficient D is spatial-invariant, $\nabla \cdot [\mathrm{D}\nabla \cdot \phi] = D\nabla^2\phi$. Hereafter we assume this case.

2.1.4 Examples: Impulse responses in an infinite scattering medium

Examples in this section repeatedly use the Helmholtz wave equation and its Green function:

$$\begin{cases} (\nabla^2 + k^2)G(\vec{\mathrm{r}}) = -\delta(\vec{\mathrm{r}}) \\ \mathrm{G}(\vec{\mathrm{r}}) = \dfrac{1}{4\pi r}e^{ikr} \end{cases}$$

Where k can take complex values. Besides, the integrals of Gaussian are also useful.

$$\int_{x=-\infty}^{\infty} \mathrm{e}^{-(\mathrm{ax}^2+\mathrm{bx}+\mathrm{c})}dx = \sqrt{\frac{\pi}{a}}\mathrm{e}^{\frac{\mathrm{b}^2-4ac}{4a}}$$

$$\int_{x=-\infty}^{\infty} \mathrm{e}^{-(\mathrm{ax}^2+\mathrm{bx}+\mathrm{c})}xdx = \frac{b}{2a}\sqrt{\frac{\pi}{a}}\mathrm{e}^{\frac{\mathrm{b}^2-4ac}{4a}}$$

For an infinitely short-pulsed ($\delta(t)$) point source ($\delta(\vec{r})$), the source term is modeled as $S_t(\vec{r},t) = S_0\delta(\vec{r},t) = S_0\delta(\vec{r})\delta(t)$. The diffusion equation and answer pair is:

$$\begin{cases} \frac{1}{v}\frac{\partial\phi(\vec{r},t)}{\partial t} + \mu_a\phi(\vec{r},t) - D\nabla^2\phi(\vec{r},t) = S_0\delta(t)\delta(\vec{r}) \\ \phi(\vec{r},t) = S_0\frac{v}{(4\pi Dvt)^{\frac{3}{2}}}e^{-\frac{r^2}{4Dvt}-\mu_a vt} \equiv \phi_t(\vec{r},t) \end{cases}$$

For constant power S_0, monochromatic (e^{-iwt}) and point source ($\delta(\vec{r})$), the source term is modeled as $S_f(\vec{r},t) = S_0 e^{-iwt}\delta(\vec{r})$. The diffusion equation and answer pair is:

$$\begin{cases} \frac{1}{v}\frac{\partial\phi(\vec{r},t)}{\partial t} + \mu_a\phi(\vec{r},t) - D\nabla^2\phi(\vec{r},t) = S_0 e^{-iwt}\delta(\vec{r}) \\ \phi(\vec{r},t) = S_0\frac{1}{4\pi Dr}e^{ikr-iwt} \equiv \phi_f(\vec{r},t) \end{cases}$$

Where $k^2 = -\frac{\mu_a}{D} + i\frac{w}{vD}$ is a function of w. Note also that because ϕ is driven by $S(\vec{r},t)$, it has the same factor e^{-iwt}. Intuitively, one can show $\phi_f(\vec{r},t)|_{w=0} = \int_{t=0}^{\infty}\phi_t(\vec{r},t)dt$.

One trick (though practical) when modeling the source is that the spatial and temporal components have been independent and decoupled. This allows us to apply separation of variables ($\phi(\vec{r},t) = \phi_r(\vec{r})\phi_t(t)$) to simplify the equations. For example, here, by writing $S(\vec{r},t) = e^{-iwt}\delta(\vec{r})$, we also write $\phi(\vec{r},t)$ of the form $\phi(\vec{r},t) = \phi(\vec{r},w)e^{-iwt}$. Therefore, Equ.6 becomes

$$\left[-\frac{iw}{v} + \mu_a\right]\phi(\vec{r},w) - D\nabla^2\phi(\vec{r},w) = \delta(\vec{r})$$

It is obvious to link the form to the Helmholtz equation and its Green function:

$$\begin{cases} (\nabla^2 + k^2)G(\vec{\mathrm{r}}) = -\delta(\vec{\mathrm{r}}) \\ \mathrm{G}(\vec{\mathrm{r}}) = \dfrac{1}{4\pi r} e^{ikr} \end{cases}$$

One immediately identifies $\mathrm{k}^2 = -\frac{\mu_a}{D} + i\frac{w}{vD}$, and $\mathrm{G}(\vec{\mathrm{r}}) = D\phi(\vec{\mathrm{r}}, w)$.

2.1.5 Units

It is good to keep in mind the units of these quantities. D is has units of m. S_0 has units of W. $\delta(\vec{\mathrm{r}})$ has units of m^{-3}. $\phi_{\mathrm{f}}(\vec{\mathrm{r}}, t)$ has units of W/m^2. $\phi_{\mathrm{t}}(\vec{\mathrm{r}}, t)$ has units of $W/m^2 s$. Finally, $\mathrm{S}_{\mathrm{t}}(\vec{\mathrm{r}}, t)$ has units of $W/m^3 s$ and $\mathrm{S}_{\mathrm{f}}(\vec{\mathrm{r}}, t)$ has units of W/m^3.

2.2 Modes of operations: TD vs. FD

L is the solution to the RTE. As a general solution to a differential equation, L contains homogeneous and inhomogeneous solutions. A homogeneous solution is the natural response describing how radiance evolves/propagates without a driving force S during the observation time window. It does however depend on initial condition that may be caused by a source that happens before the observation window. Investigating the homogeneous solution is the main subject if operating in the time-domain as its source would be modeled as $\delta(\vec{r})\delta(\mathrm{t})$ where the source is off after $t = 0$. On the other hand, the inhomogeneous solution of L is the response to the continuous excitation source S. If S operates with frequency ω, $S = \delta(\vec{r})e^{j\omega t}$, L will also respond in the same frequency, meaning L is of the form of $L_{\vec{r}}e^{j\Delta(\vec{r})}e^{j\omega t}$. This is the frequency domain operation, the most mature and dominant to date. Because L is expected to respond in the same frequency, narrowband detection can be implemented to enhance the SNR. However,

usually the experiment is carried out in one single frequency. The information obtained is less complete than that obtained in time-domain operation. To bring the missing information back (for example, to be able to separate absorption μ_a from scattering μ_s, rather than a lump sum as extinction $\mu_t = \mu_a + \mu_s$), mathematics gives a clue by observing that $\delta(t) = \frac{1}{2\pi}\int_{-\infty}^{\infty} e^{j\omega t} d\omega$, meaning as long as multiple and sufficient frequencies are used, the same amount of information can be recovered.

2.3 Linear image reconstruction

2.3.1 Linear relationship between fluorescence and fluorophore distribution

In section 0, we see the equivalence of time-domain and frequency-domain mode operations. I continue to develop the linear image reconstruction in the following two sections. In this section, I derive the linear relationship between the measured fluorescence and the fluorophore distribution, which is the tomography of interest to solve. In the next section, I explicitly express the fluorophore distribution in terms of the measured fluorescence.

The frequency-domain result in section 2.1.4 is

Equ.7

$$\begin{cases} (\nabla^2 + k^2)\phi(\vec{r}, w) = -\delta(\vec{r})S_0 \\ \phi(\vec{r}, w) = S_0 \frac{1}{4\pi D r} e^{ikr} \end{cases}$$

Where $k^2 = -\frac{\mu_a}{D} + i\frac{w}{vD}$, and $\phi(\vec{r}, t) = \phi(\vec{r}, w)e^{-iwt}$.

The optical contrast of FLOT is fluorescence. The fluorescence intensity F depends on multiple factors, including the detector's quantum efficiency, the detector's geometry, the fluorophores' quantum efficiency, and the number of photons absorbed. The fact that the fluorescence intensity is proportional to the absorption [19], suggests that we can apply the perturbation theory to μ_a, one of which is Born approximation[3]. The aim of the linear image reconstruction is to relate the measured fluorescence intensity distribution to the local change $\Delta\mu_a = \Delta\mu_a(\vec{r}) = \Delta\mu_a(x, y, z)$.

By perturbation, $\Delta\mu_a \ll \mu_a$ is assumed. Mathematically, we replace $\mu_a \to \mu_a + \Delta\mu_a(\vec{r})$. $\phi(\vec{r}, w)$ must accommodate this change to be a legitimate solution to Helmholtz equation. Therefore, we replace $\phi(\vec{r}, w) \to \phi(\vec{r}, w) + \Delta\phi(\vec{r}, w)$and obtain:

$$Equ.8 \qquad \left(\nabla^2 \underbrace{-\frac{\mu_a}{D} + i\frac{w}{vD}}_{k^2} - \frac{\Delta\mu_a(\vec{r})}{D}\right)[\phi(\vec{r}, w) + \Delta\phi(\vec{r}, w)] = -\delta(\vec{r})S_0$$

The idea of the perturbation theory is to require Equ.7 and Equ.8 hold true simultaneously. Also, as a first-order approximation, $\frac{\Delta\mu_a(\vec{r})}{D}\Delta\phi(\vec{r}, w)$ is ignored. After simplified by Equ.7, Equ.8 becomes

$$(\nabla^2 + k^2)\Delta\phi(\vec{r}, w) = \frac{\Delta\mu_a(\vec{r})}{D}\,\phi(\vec{r}, w) = -\delta(\vec{r}) * [-\frac{\Delta\mu_a(\vec{r})}{D}\,\phi(\vec{r}, w)]$$

---

[3] Perturbation has been approached in two ways. Born approximation models the small fluctuation linearly ($\mu_a \to \mu_{a0} + \Delta\mu_a(\vec{r})$), which is the approximation implemented in this thesis. Alternatively, Rytov approximation models the small fluctuation exponentially.

Therefore,

$$\Delta\phi(\vec{r},w) = \underbrace{G(\vec{r})}_{\frac{1}{4\pi r}e^{ikr}} * \left[-\frac{\Delta\mu_a(\vec{r})}{D}\ \underbrace{\phi(\vec{r},w)}_{\frac{S_0}{4\pi D r}e^{ikr}}\right]$$

Where $*$ stands for convolution. This is the solution when the source is placed at the origin. If the point source is at $\vec{r_s}$,

Equ.9
$$\Delta\phi(\vec{r},w) = G(\vec{r}) * \left[-\frac{\Delta\mu_a(\vec{r})}{D}\ \phi(|\vec{r}-\vec{r_s}|,w)\right]$$

$$= \int d^3\vec{r'} \cdot \underbrace{G(\vec{r}-\vec{r'})}_{\frac{1}{4\pi\left|\vec{r}-\vec{r'}\right|}e^{ik\left|\vec{r}-\vec{r'}\right|}} \cdot -\frac{\Delta\mu_a(\vec{r'})}{D} \cdot \underbrace{\phi\left(\left|\vec{r'}-\vec{r_s}\right|,w\right)}_{\frac{S_0}{4\pi D\left|\vec{r'}-\vec{r_s}\right|}e^{ik\left|\vec{r'}-\vec{r_s}\right|}} \equiv \Delta F(\vec{r_s},\vec{r_d})$$

$\Delta\phi(\vec{r},w) \equiv \Delta F(\vec{r_s},\vec{r_d})$, $\vec{r_d} = \vec{r}$ is denoted to emphasize that the fluorescence difference is measured by placing source at $\vec{r_s}$ and detector at $\vec{r_d}$. It is reasonable to assume that both $\vec{r_s}$ and $\vec{r_d}$ point towards the surface of the sample. The surface may not be flat, but the emphasis is that we use the fluorescence light that escapes from the sample surface to estimate fluorophore (the origin of the local change $\Delta\mu_a$) distribution deep within the sample.

Equ.9 is instructive. First of all, it shows that $\vec{r}$ and $\vec{r_s}$ are interchangeable. This is more than a coincidence; this has a physical significance and is referred as principle of reciprocity: exchanging the source and observation points does not affect the solution. Here, it means the detected fluorescence intensity remains the same. Secondly, Equ.9

illustrates that what the detector at $\vec{r}$ receives is the summed-up fluorescence intensity propagating to $\vec{r}$ from every possible $\vec{r'}$, while the strength of the fluorescence also depends on how much the source power can deliver from $\vec{r_s}$ to every possible $\vec{r'}$. Here we reserve the flexibility of $G(\vec{r}-\vec{r'})$ and $\phi\left(\left|\vec{r'}-\vec{r_s}\right|,w\right)$, which are equal to a spherical wave as a result of the diffusion approximation. In section 2.3, we will take the advantage of Monte-Carlo simulation to enrich their content.

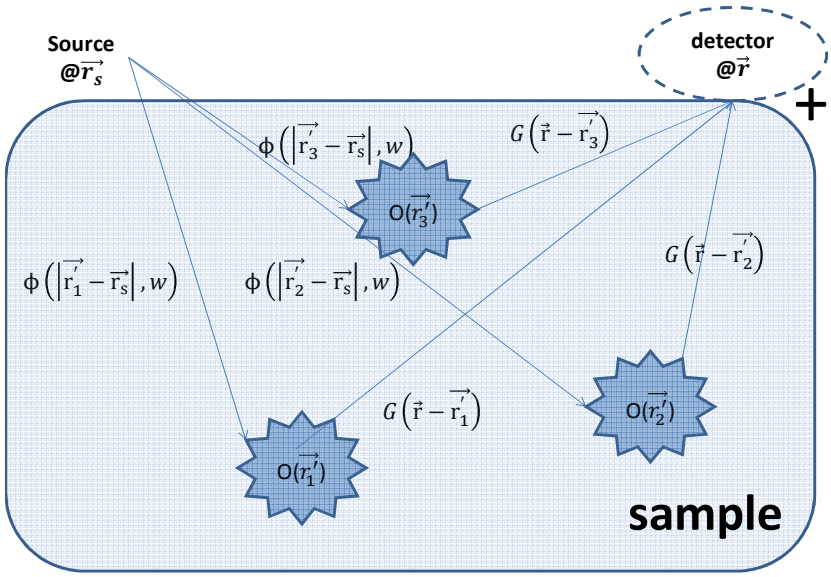

Figure. 4 Illustration of Equ.9

Figure. 4 is a graphical illustration, where $O(\vec{r'})=-\frac{\Delta\mu_a(\vec{r'})}{D}d^3\vec{r'}$ stands for a fluorophore object at $\vec{r'}$. The general principle of LOT families is now clear. Since we are able to physically vary the detector's position and even its viewing angle, we can modulate the weighting of $O(\vec{r'})$, which is $G(\vec{r}-\vec{r'})\phi\left(\left|\vec{r'}-\vec{r_s}\right|,w\right)$. In principle, this indicates that it

is possible to recover $O(\overrightarrow{r'})$ from $\Delta F(\overrightarrow{r_s}, \overrightarrow{r_d})$. For example, in Figure. 4, if we know there are only 3 fluorescence objects in the sample for sure, then we know we can acquire $\Delta F(\overrightarrow{r_s}, \overrightarrow{r_d})$ at least at 3 different positions $\overrightarrow{r_d} = \overrightarrow{r_1}, \overrightarrow{r_2}, \overrightarrow{r_3}$ to recover $O\left(\overrightarrow{r_1'}\right), O\left(\overrightarrow{r_2'}\right), O\left(\overrightarrow{r_3'}\right)$ because

$$\begin{cases} \Delta F(\overrightarrow{r_s}, \overrightarrow{r_1}) = W_{11} O\left(\overrightarrow{r_1'}\right) + W_{12} O\left(\overrightarrow{r_2'}\right) + W_{13} O\left(\overrightarrow{r_3'}\right) \\ \Delta F(\overrightarrow{r_s}, \overrightarrow{r_2}) = W_{21} O\left(\overrightarrow{r_1'}\right) + W_{22} O\left(\overrightarrow{r_2'}\right) + W_{23} O\left(\overrightarrow{r_3'}\right) \\ \Delta F(\overrightarrow{r_s}, \overrightarrow{r_3}) = W_{31} O\left(\overrightarrow{r_1'}\right) + W_{32} O\left(\overrightarrow{r_2'}\right) + W_{33} O\left(\overrightarrow{r_3'}\right) \end{cases}$$

Equ.10 $$W_{mn} \equiv G\left(\overrightarrow{r_m} - \overrightarrow{r_n'}\right) \phi\left(\left|\overrightarrow{r_n'} - \overrightarrow{r_s}\right|, w\right)$$

Where W_{mn} is of unit $\mathrm{W/m^3}$. $O\left(\overrightarrow{r_n'}\right)$ is of unit m.

However, practically, we don't know the number of fluorophores within the sample. Moreover, they may even be grouped. So it is preferred to acquire as many different $\Delta F(\overrightarrow{r_{sm}}, \overrightarrow{r_{dm}})$ values as possible, and understand $O\left(\overrightarrow{r_n'}\right)$ as the relative unit-less fluorophore concentration at $\overrightarrow{r_n'}$. As a result, in the discrete form of Equ.9, we arrive at

Equ.11 $$F \equiv \begin{bmatrix} \Delta F(\overrightarrow{r_{s1}}, \overrightarrow{r_{d1}}) \\ \Delta F(\overrightarrow{r_{s2}}, \overrightarrow{r_{d2}}) \\ \vdots \\ \Delta F(\overrightarrow{r_{sM}}, \overrightarrow{r_{dM}}) \end{bmatrix} = \begin{bmatrix} W_{11} & \cdots & W_{1N} \\ \vdots & \ddots & \vdots \\ W_{M1} & \cdots & W_{MN} \end{bmatrix} \begin{bmatrix} O\left(\overrightarrow{r_1'}\right) \\ O\left(\overrightarrow{r_2'}\right) \\ \vdots \\ O\left(\overrightarrow{r_N'}\right) \end{bmatrix} \equiv WO$$

Equ.11 implies that M different measurements are used to attempt to reconstruct $O\left(\overrightarrow{r'}\right)$, which is described by N pixels. $O\left(\overrightarrow{r'}\right)$ is generally applicable to represent a 3D

tomogram, but in my thesis, it will represent a ZX cross-section of the sample. $W = [W]_{\mathrm{M\times N}}$ is referred to as the weight matrix, sensitivity matrix, or Jacobian matrix. Each row of the matrix is a vectorized sensitivity profile indicating the probability density of photons delivered to each location by the source and captured by the detector.

2.3.2 The method of least squares

By solving $F = WO$, the task is to estimate **an** O such that WO matches F as closely as possible. This process is called a forward problem. Alternatively, the backward problem focuses on how to derive O. A well-established mathematical tool, known as the method of least squares, has been widely applied. Using this tool, the mathematical question is to look for **an** O such that it minimizes $\|F - WO\|_2^2 \equiv \Sigma_{\mathrm{m}} |F_m - \Sigma_n W_{mn} O_n|^2$.

This question has the analytical answer. One approach is to perform singular value decomposition (SVD) on W, namely $[W]_{M\times N} = [U]_{M\times M}[S]_{M\times N}[V]_{N\times N}^T$. The beauty of singular value decomposition is that both U and V are unitary matrices, and that $[S]_{M\times N}$ is effectively a min(M,N)-by-1 vector (its off-diagonal elements are all zero). The idea of SVD is to bring F and O to the common space through U and V, respectively. In other words, $\mathrm{U}^{\mathrm{T}}F$ and $\mathrm{V}^{\mathrm{T}}O$ are in the same space where manipulation could probably be the simplest. Through the aid of SVD, we can reformulate our task again: to look for **an** $\mathrm{V}^{\mathrm{T}}O$ such that it minimizes

$$\|U^T F - SV^T O\|_2^2 \equiv \Sigma_{\mathrm{m}} |[U^T F]_m - \Sigma_n S_{mn}[V^T O]_n|^2 = \Sigma_{\mathrm{m}} ([U^T F]_m - S_{mm}[V^T O]_m)^2.$$

The last equality is because $S_{mn} = S_{mm}\delta_{mn}$. It is clear that the minimum is achieved by setting $[V^T O]_m = \frac{1}{S_{mm}}[U^T F]_m, \forall \mathrm{m} = \min(\mathrm{M}, \mathrm{N})$. If $\mathrm{N} < \mathrm{M}$, $F = WO$ is an over-determined system. There are not enough degree of freedom of $V^T O$ to set to meet $[U^T F]_m, \forall \mathrm{m} = \mathrm{N}+1 \sim \mathrm{M}$. Nevertheless, $V^T O$ and therefore O is certain. This is however a rare case because a fine tomography is always desirable, meaning that N is normally huge and $\mathrm{N} > \mathrm{M}$. This is an under-determined system, meaning the choice of O is not unique because every such candidate minimizes $\|F - WO\|_2$ as well as any others. The physical explanation of non-uniqueness of O is that the depth selectivity and resolution degrades as the depth of fluorescent object increases. To extreme, whether a very deep fluorophore is present or not does not change the measurement. Therefore, O is not unique.

In order to make O unique, we have to add additional assumptions about O. We will focus on the most common assumption, the L_2 norm, to develop the solution O. In the sense of L_2 norm, it is assumed that O is smooth. The task is modified as to look for **the** (smoothest) O such that it minimizes $\|F - WO\|_2^2 + \lambda^2\|O\|_2^2$. Because U and V are unitary, $\|F - WO\|_2^2 + \lambda\|O\|_2^2 = \|U^T F - SV^T O\|_2^2 + \lambda\|V^T O\|_2^2$. The solution is $[V^T O]_m = \frac{S_{mm}}{S_{mm}^2 + \lambda^2}[U^T F]_m, \forall \mathrm{m} = \min(\mathrm{M}, \mathrm{N})$. For $\mathrm{N} > \mathrm{M}$, although there are still many solutions to O that can give the minimal $\|F - WO\|_2^2$, there is only one O among others that is the smoothest (having the minimal $\|O\|_2^2$). λ is known as the regularization parameter. The selection of λ will be discussed in section 2.3.3. In the L_2 norm, this is known as Tikhonov regularization. The solution is now clear:

Equ.12 $$O = V\left[\frac{S}{S^2+\lambda^2}\right]_{N\times M} U^T F = V\left[\frac{S^2}{S^2+\lambda^2}\cdot\frac{1}{S}\right]_{N\times M} U^T F$$

Note again that $S_{mn} = S_{mm}\delta_{mn}$ are the entries in matrix S.

While Equ.12 suggests that O is uniquely determined (even if we deal with an under-determined system), caution should be exercised. The uniqueness of O comes from the modeling of W. In other words, one adds an additional expectation or assumption on the measured F. One is therefore able to infer the content of higher dimensioned O from lower dimensioned F. Moreover, the measured F is always corrupted by noise. The reconstructed O based on this noisy F is also noisy. Tikhonov regularization in fact reflects such process. Its preference on the minimal L_2 form of O expects/prefers a smooth object.

2.3.3 Discrepancy principle and L-curve

The measurement in general is corrupted by noise. One way to remove the noise is to apply a filter. In fact, the coefficients $\frac{S^2}{S^2+\lambda^2}$ that appear in Tikhonov regularization in the previous section 2.3.2 are the Wiener filter weights. The strength of the filter is controlled by λ. Among others, discrepancy principle and L-curve are two criteria needed to select λ. First, instead of $F = WO$, the reconstruction scheme has to be modified as

Equ.13 $$F = WO + \varepsilon$$

Where ε models the noise. The discrepancy principle [20] states that if we have an estimate on the magnitude of noise, then any solution that produces a measurement with

error of the same magnitude as noise is acceptable. For example, if $\varepsilon \in \mathrm{R}^{\mathrm{M}}$ satisfying $\varepsilon_i \sim \mathrm{N}(0, \sigma^2)$, then O is acceptable if $\|F - WO\|_2^2 \leq \|\varepsilon\|_2^2 = M\sigma^2$. Along with Tikhonov regularization, the λ is the unique root of the function

$$\mathrm{f}(\lambda^2) = \left[\sum_{j=1}^{\min(M,N)} \left(\frac{\lambda^2}{S_{jj}^2 + \lambda^2}\right) F_j^2\right] + \left[\sum_{j=\min(M,N)+1}^{\mathrm{M}} F_j^2\right] - \|\varepsilon\|_2^2$$

Alternatively, the L-curve criterion [21] is to find the λ that minimizes the curvature $\mathrm{k}(\lambda^2)$ of the L-curve:

$$\mathrm{k}(\lambda^2) = \frac{\xi''\eta' - \eta''\xi''}{(\xi'^2 + \eta'^2)^{3/2}}$$

where the superscripts $'$ and $''$ denotes respectively the first and second derivatives with respect to λ, and $\|F - WO\| \equiv \xi(\lambda^2)$ and $\|O\| \equiv \eta(\lambda^2)$. Both ξ and η are functions of λ because O is influenced by λ, as shown in Equ.(12). Also see Figure. 5.

The L-curve is given its name due to the appearance of the plot (η, ξ). Remembering that the task is to minimize $\|F - WO\|_2^2 + \lambda^2\|O\|_2^2$, to plot (η, ξ) is therefore understandable and intuitive. The fact that the plot of (η, ξ) shows a L shape[4] indicates that the corner of the L-curve is a good balance between minimization of the sizes of ξ and η. If λ is too small, the demand of smoothness is eased and O tends to be over fitted, resulting in a

[4] It can be shown the plot (η, ξ) will always have an L-shaped appearance. [93_hansen_Oleary]

noisy O, small ξ, and large η. On the other hand, in the reverse case, O would be over-smoothed, giving large ξ and small η. The distinct L-shaped corner indicates exactly where O changes in nature. One remark is that ξ and η may be replaced by $\ln(\xi)$ and $\ln(\eta)$ to emphasize the "flat" parts of the L-curve. [2, 21]

In my experience, I used either the discrepancy principle or the L-curve criteria, depending on the level of noise, ξ, which in turn is determined by how well the fluorescence signal stands out from the background noise, or signal-to-noise ratio SNR. If the SNR is high, λ shall be small to prevent O from over-smoothing, satisfying the L-curve criterion. Alternatively, If the SNR is low, λ has to be large, satisfying the discrepancy principle criterion. Because $\lambda_{\mathrm{DP}} > \lambda_{\mathrm{LC}}$, it can be foreseen that O_{DP} is usually much smoother than O_{LC}, and this is often the criticism of the discrepancy principle criterion.

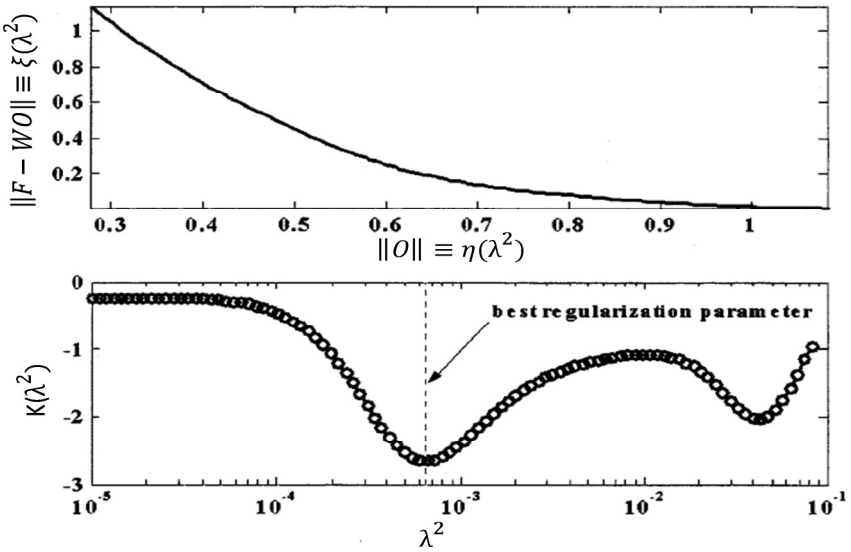

Figure. 5 Illustration of the best regularization parameter using the L-curve criterion. [2]

2.3.4 The hard constraint

Equ.9 shows that the origin of the contrast is from absorption. The hard constraint is that the absorption coefficient $\mu_a(\vec{r}) = \mu_{a0} + \Delta\mu_a(\vec{r})$ is always a positive quantity. (Note that the perturbed part $\Delta\mu_a$ can be either positive or negative.) This means that the magnitude of $\Delta\mu_a$ should always be smaller than that of μ_{a0}. When performing the reconstruction using the preceding matrix inversion method, Equ.12, negative absorption coefficients can however occur. The rigorous way to solve for O is therefore to additionally abide by the non-negativity of O. This can be done analytically, for example, using Matlab's built-in function *lsqlin*. However, it is a time-consuming process (Without the hard constraint, the inversion takes 0.06 sec; with the hard constraint, the inversion solving by *lsqlin* takes

700 sec when solving $[\mathrm{W}]_{4900\times4900}$ using a dual-core 2.53GHz CPU, 32bit-Windows XP, and 3.5GB RAM)

The convenient way is to set those negative elements in O to zero afterwards, where O is obtained using the normal inversion as if there is no hard constraints.

Because of the hard constraint (HC), the feasible domain of O is reduced, increasing the size of $\|F - WO\|$. The rigorous way searches the best O (in the sense of the smallest $\|F - WO\|$) within the feasible domain. The convenient way picks a good one from within. Empirically, (probably can be mathematically proven),

$$\|F - WO\|_{without\ HC} < \|F - WO\|_{with\ HC} < \|F - WO\|_{convenient}$$

This again reminds us that importance of high SNR measurements. In fact, in a special case, the matrix inversion can be simply skipped while the hard constraint is naturally satisfied.

2.3.5 Stacking representation

For the high scattering applications where diffusion approximation is valid, Equ.9 and Equ.10 have revealed the analytical form of W, where the impulse response of both G and ϕ from a point source is a spherical wave. Modeling illumination source as a point source is also justifiable because the high scattering nature destroys the directionality of incident photons quickly after photons enter the sample. The weight matrix W summarizes how photons distribute themselves in the scattering medium. Numerical

implementations of W for general scattering cases will be mentioned in section 2.3. It is however worthwhile to explore the other extreme, the no scattering case.

For no scattering applications, such as when the background of the sample is air or water, the diffusion approximation is invalid. While in general RTE can be applied, the tomogram O in fact can be geometrically determined from the measurement F. [22] The stacking representation simply renders F in an attempt to represent as much as possible the tomogram O. Figure. 6 explains the procedure to infer the depth from raw measurements. The acquired reflection and fluorescence images showed a distinct shift in distance. A simple application of Snell's law determined the depth of the capillary tube. In other words, a 2D image can include the 3D depth information. See Figure. 7 as an example. Note however that the enabling of stacking, oblique illumination/collection has been assumed.

The simple relation $F \cong O$ is actually not a surprise. The fact is that between the image plane/volume and the object plane/volume there exists more or less point-to-point mapping, depending on the PSF of the optical system. This is in fact the fundamental of geometric optics. In one ideal situation, the PSF is the delta function, and therefore $F(\overrightarrow{r_d}) = O * PSF = \int O(\vec{r})\delta(\vec{r} - \overrightarrow{r_d})d^3\vec{r} = O(\overrightarrow{r_d})$. Even though the PSF is not a delta function, it does not (should not) deviate significantly from the delta function. Many optical systems achieve δ-like PSFs for the sake of higher resolution.

Between the low and high scattering extreme, one question is when the stacking representation remains valid? According to the simulation in section 3.3, I will show that

it does when photons travel within one the mean free path (MFP), the reciprocal of reduced scattering coefficient. Within one MFP, $F \cong O$. Beyond, the inversion of $F = WO$ should be necessary.

Comparing $F \cong O$ and $F = WO$, we draw several observations.

1. It is found that W is more or less an identity matrix $[I]_{\mathrm{M\times N}}$.[5] Every single row of W has one distinct large entry and every other entries are close to 0. Physically, the large entry at index k means the optic system probes at $\overrightarrow{r_k}$.
2. It is expected that if the scattering gradually increases, W would deviate from the identity matrix gradually, de-emphasizing the weighting at the entry k, and slightly emphasizing the neighbors of the entry k.
3. The inversion of $F = WO$ is like a PSF-de-convolution process, trying to replace each measured PSF pattern with a point. Because $F = WO$, rendering F gives the PSF-convolved image of O. A comparison between the stacking and the reconstruction is shown in Figure. 8.
4. If $F \cong O$, simply rendering F can give a reasonable understanding about O. Take the most common microscope as an example: the user places the specimen under the

[5] W being the identity is an ideal but not the only ideal situation. In optical coherence tomography, $\mathrm{W_{ideal,mn}} = \mathrm{e}^{\mathrm{i}\frac{4\pi}{\lambda_m}\mathrm{z_n}}$ is apparently different from the identity, but one can reconstruct O because $\mathrm{F} = \mathrm{WO}$ is discrete Fourier transform of O. Therefore,O obtained by the inverse transform.

microscope and is ready to see the magnified image of the specimen through the eye piece. The optics setup simply performs a relay and a magnification.

5. The PSF in a broader sense depends on both imperfection of the optical system itself and the characteristics of the specimen. The power of using W is in that one can bring additional information about the specimen, described in W, into the system, thus resolving O.
6. Especially in mesoscopic 3D optical imaging, the PSF evolves along the axial direction (because of either the optics or the scattering of the specimen). A more accurate system should use many PSFs, instead of a single PSF. One may take advantages of these abundant yet distinct PSFs to perform tomographic imaging. In appendix 2, a primitive idea about using aberration and apodizaiton to achieve tomographic imaging is described. The content however is limited to the no scattering case, which means the scattering from the sample plays no part in distorting the PSFs of the optical system. The PSFs of aFLOT were experimentally demonstrated in section 4.6.
7. Because the measurement F is fluorescence intensity, F by nature is positive. Therefore, if $F \cong O$ holds, O satisfies the hard constraint.
8. The possible meaningful stacking representation gives the optician an important tool. If PSFs have been similar to the δ function, it may be unnecessary to perform the inversion or the de-convolution because performing de-convolution is usually difficult. On the other hand, if W is far different from the identity matrix, the inversion may become prerequisite to recovering O. Ultimately, one realizes that

there are two ways to reduce the size of PSFs: One is to modify optics, such as to introduce the oblique illumination, one main body of this thesis that will be discussed in chapter 3; the other is through the aid of de-convolution signal processing.

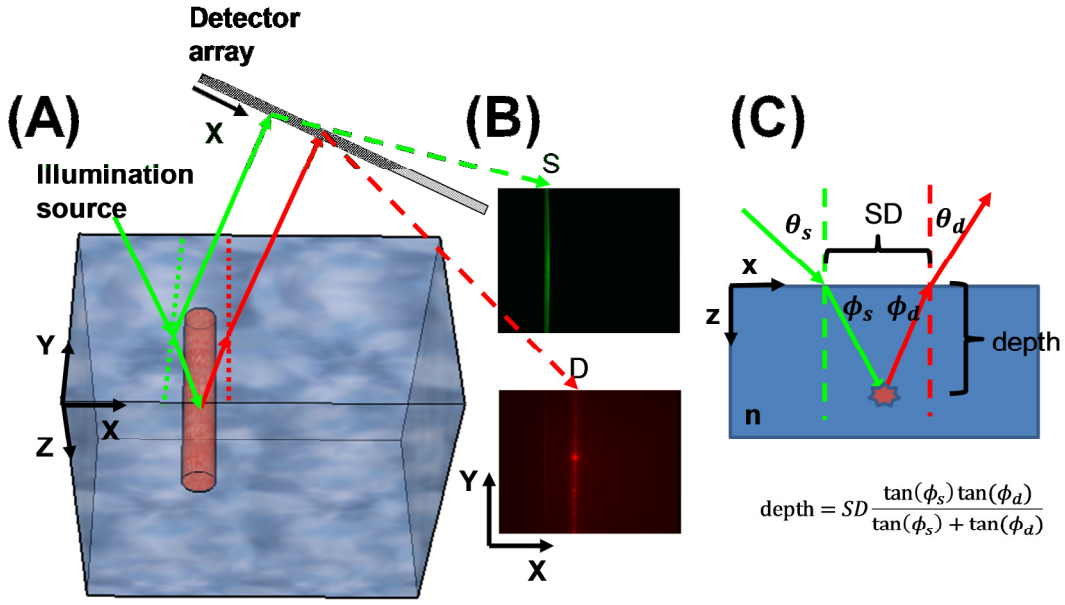

Figure. 6 Geometrical determination of the depth of fluorescence object.

The Rd6G fluorescent dye was injected into a capillary tube which was immersed in water. (A) Perspective view. (B) Experimental image. Green signal is the reflected excitation light. Red signal is the emission fluorescence from the capillary tube buried in water. (C) Cross-section view and also the formula for determining depth from the SD distance.

Note that interpreting the depth from SD fails when the source and the detector are normal.

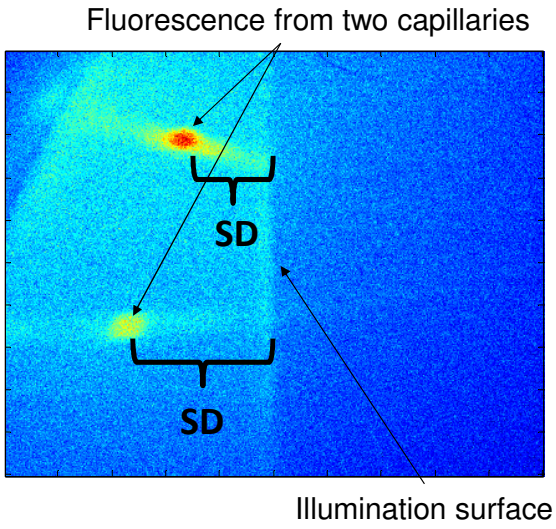

Figure. 7 Example of dictating depth from 2D image.

Oblique line sheet was shone on the PEG hydrogel, a semi-transparent sample, in which two capillaries were embedded. SD , the distance between the fluorescing spot and illumination surface, infers the depth of the capillaries.

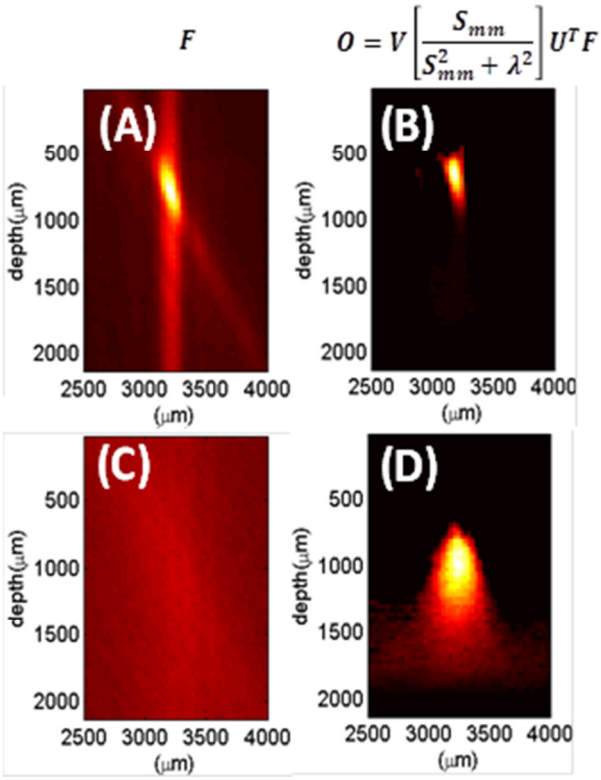

Figure. 8 Comparison between stacking representation (A, C) and the reconstruction (B, D).

The object was a capillary cross-section. The top row shows the capillary placed at 700 micron. The bottom row shows the capillary placed at 1000 micron. The PSF pattern of aFLOT is an oblique star, as is clear in (A).

2.3.6 Revisit RTE: the angular degree of freedom

Equ.9 and Equ.11 are arrived at by assuming that the diffusion equation and first-order perturbation (or Born approximation) apply, but $F = WO$ may still hold in a broader scheme. Essentially, Equ.9 reveals this relationship:

$$\Delta F(\vec{r_s}, \vec{r_d}) = \int G(\vec{r_d} - \vec{r'}) \cdot O(\vec{r'}) \cdot \phi(\vec{r'} - \vec{r_s}, w) d^3\vec{r'}$$

According to the derivation in [23][6], it appears that one may not need to assume an isotropic source (as is here) before arriving such relationship. The fluorescence signal with angular dependence $\mathrm{F}\left(\overrightarrow{r_d}, \widehat{\Omega}_\mathrm{d}; \overrightarrow{r_s}, \widehat{\Omega}_s\right)$ ($\mathrm{Wm^{-2}sr^{-2}}$) can be similarly expressed as:

$$\mathrm{F}\left(\overrightarrow{r_d}, \widehat{\Omega}_\mathrm{d}; \overrightarrow{r_s}, \widehat{\Omega}_s\right) = \int \mathrm{G}\left(\overrightarrow{r'} - \overrightarrow{r_d}; \widehat{\Omega}_\mathrm{d}\right) \mathrm{O}\left(\overrightarrow{r'}\right) \phi\left(\overrightarrow{r'} - \overrightarrow{r_s}; \widehat{\Omega}_s\right) d^3\overrightarrow{r'}$$

Or

$$Equ.14 \qquad \begin{cases} F\left(\overrightarrow{r_d}, \widehat{\Omega}_d; \overrightarrow{r_s}, \widehat{\Omega}_s\right) = \int W(\vec{r}; \overrightarrow{r_s}, \widehat{\Omega}_s, \overrightarrow{r_d}, \widehat{\Omega}_d) O(\vec{r}) d^3\vec{r} \\ W\left(\vec{r}; \overrightarrow{r_s}, \widehat{\Omega}_s, \overrightarrow{r_d}, \widehat{\Omega}_d\right) = G\left(\vec{r} - \overrightarrow{r_d}; \widehat{\Omega}_d\right) \phi\left(\vec{r} - \overrightarrow{r_s}; \widehat{\Omega}_s\right) \end{cases}$$

Where $\widehat{\Omega}_\mathrm{d}$ and $\widehat{\Omega}_\mathrm{s}$ stand for the detection and illumination direction, respectively. Therefore, $F = WO$ is still applicable. More importantly, one is able to design and describe the system more flexibly, which is the angular degree of freedom. A side remark is that the unit of $\mathrm{F}\left(\overrightarrow{r_d}, \widehat{\Omega}_\mathrm{d}; \overrightarrow{r_s}, \widehat{\Omega}_s\right)$ is now $Wm^{-2}sr^{-2}$. Physically, one still needs to integrate $\mathrm{F}\left(\overrightarrow{r_d}, \widehat{\Omega}_\mathrm{d}; \overrightarrow{r_s}, \widehat{\Omega}_s\right)$ over a small range of angles around $\widehat{\Omega}_\mathrm{d}$ and $\widehat{\Omega}_\mathrm{s}$, but preservation of the angular directionality is certain.

The question now is how to describe $\mathrm{G}\left(\vec{r} - \overrightarrow{r_d}; \widehat{\Omega}_\mathrm{d}\right)$ and $\phi\left(\vec{r} - \overrightarrow{r_s}; \widehat{\Omega}_s\right)$. We have seen that they have analytic forms in Equ.9, but the form is arrived at by assuming the diffusion approximation. Alternatively, Monte-Carlo simulation provides numerical description of photon distribution.

---

[6] Specifically around Equ.3-7 in page 6514 in the reference

2.4 Monte-Carlo simulation

Extremely high and low scattering cases have been reviewed in previous sections. The lesson is that if considering the no scattering case, one may render a simple stacking result to represent the tomography. In the high scattering case, one may write the sensitivity matrix W in the analytical form, which is derived from the diffusion approximation. In the middle ground, Monte-Carlo (MC) simulation is another option for attaining a more accurate description of W, given additional optical properties about the sample.

2.4.1 Introduction

MC simulation is a statistically-based method designed to simulate time-resolved photon transport in a 3D turbid media. Unlike most model-based techniques which produce solutions by solving a set of differential equations, such as the RTE in section 2.1.2, MC simulation generates solutions by modeling photon migration and distribution in turbid media after launching a large number of independent random trials.

As we have seen, solving RTE is non-trivial, especially in arbitrarily complex media. When an analytical solution is not possible or finite-element modeling of the RTE becomes unreasonable, MC simulation should be considered. Regarding its accuracy, one study has shown that the solution to the diffusion equation and the MC solution are comparable for highly scattering media.

Other reasons why MC simulation became popular include its generality and capability of handling arbitrary media, the simplicity of its implementation, avoiding the mesh

generation as in finite-element modeling, and the recent advent of parallel computing techniques[24]. MC simulation used to be an intensive computing task due to the large amount of photons needing to be simulated. For a typical domain size in the human head, over an hour or more of computational time is required [25] in comparison to a few seconds for solving the DE [26] or a few minutes for solving the RTE [27]. In recent years, Graphical Processing Units (GPU) based on massively parallel computing techniques have been applied, dramatically enhancing the computational efficiency. MC simulation therefore advances to be a practical method for data analysis in a wide range of diffuse optical imaging applications, such as human brain or small-animal imaging.

2.4.2 Implementing the weight matrix using MC simulation

In Equ.7, Equ.9, and Equ.10, we see that $\mathrm{W} = \mathrm{G}\left(\vec{\mathrm{r}} - \overrightarrow{\mathrm{r'}}\right)\phi\left(\left|\overrightarrow{\mathrm{r'}} - \overrightarrow{\mathrm{r_s}}\right|, \mathrm{w}\right)$. That G and ϕ have an analytical form is a result of the diffusion approximation. In Equ. 14 , $W\left(\vec{r}; \overrightarrow{r_s}, \widehat{\Omega}_\mathrm{s}, \overrightarrow{r_d}, \widehat{\Omega}_\mathrm{d}\right) = \mathrm{G}\left(\vec{r} - \overrightarrow{r_d}; \widehat{\Omega}_\mathrm{d}\right)\phi\left(\vec{r} - \overrightarrow{r_s}; \widehat{\Omega}_s\right)$ where G and ϕ do not have simple analytical forms, MC simulation numerically generates G and ϕ. While ϕ is the source photon distribution and G is the probability density or positional importance, the difference is in scalar units. Therefore, very often, one uses Monte-Carlo simulation to generate both ϕ and G.

Because how photons distribute themselves directly relates to the optical properties of the sample, MC simulation requires the user to specify (1) the index of refraction of the sample, (2) the scattering coefficient μ_s of the sample, (3) the absorption coefficient μ_a of the sample, and (4) the anisotropy g of the sample.

In this thesis, Monte-Carlo-Extreme (MCX), developed by Dr. Qianqian Fang, was used.[24] 10^7 photons were routinely simulated for one sensitivity profile, or a row in W. To achieve a fine tomogram, the voxel size was usually around $6^3 \mu m^3$. This means a typical field of view (FOV) describing the 3D photon distribution in cubes of size 2.4 mm required about $400 \times 400 \times 400$ voxels. The position and incidence angle of the illumination source can be specified by the user. Because aFLOT was implemented using line-illumination (line along Y), photon distribution in the Y direction was summed up (instead of picking the central cross-section). Note however this step is valid only when assuming the sample is homogeneous. Line illumination reduced the computation significantly and allows us to represent the photon distribution in 2D, since it is homogeneous along Y.

One question was that since the line illumination only requires a 2D photon distribution, would it be necessary to simulate a 3D photon distribution in advance? The answer is yes. For example, if a volume of $400 \times 1 \times 400$ (in XYZ) voxels is simulated, it will be different from the simulated volume of $400 \times 400 \times 400$ voxels, whose Y dimension is later projected. The volume required is the volume where the photon distribution is observed, but not the volume which confines the photons.

One example of the 3D oblique line illumination is shown in Figure. 9. As illustrated, the 2D representation suffices. Figure. 10 gives 6 examples of measurement configurations of FLOT (The definition of configuration will be given in section 3.2) Figure. 13 gives 3

examples of configurations for both FLOT and aFLOT. Each configuration after vectorized corresponds to a row in W.

Lastly, to prevent the case in which one configuration is superior to one another, W is normalized. In this thesis, the normalization is done by

1. weighting the elements in O according to the sum of each column of W, and
2. weighting the elements in M according to the sum of each row of W.

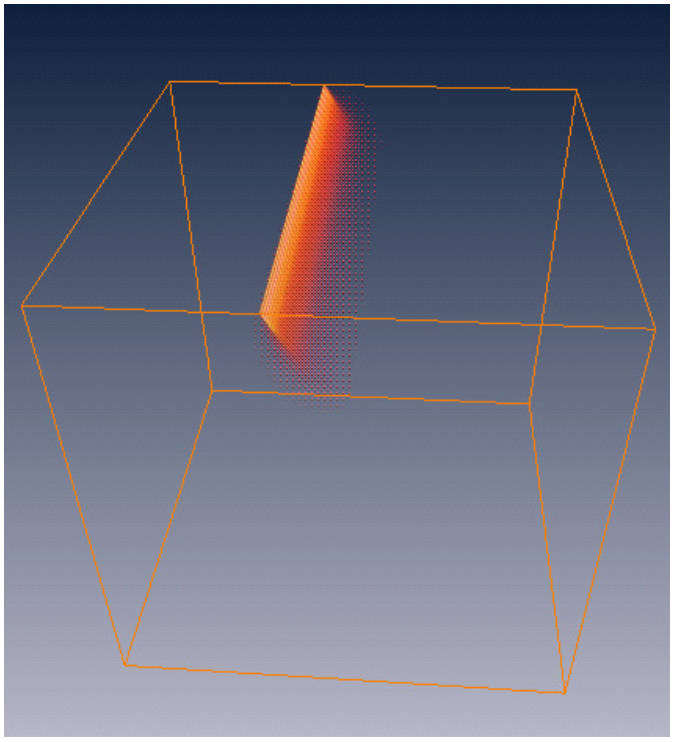

Figure. 9 The line illumination simulated by MCX.

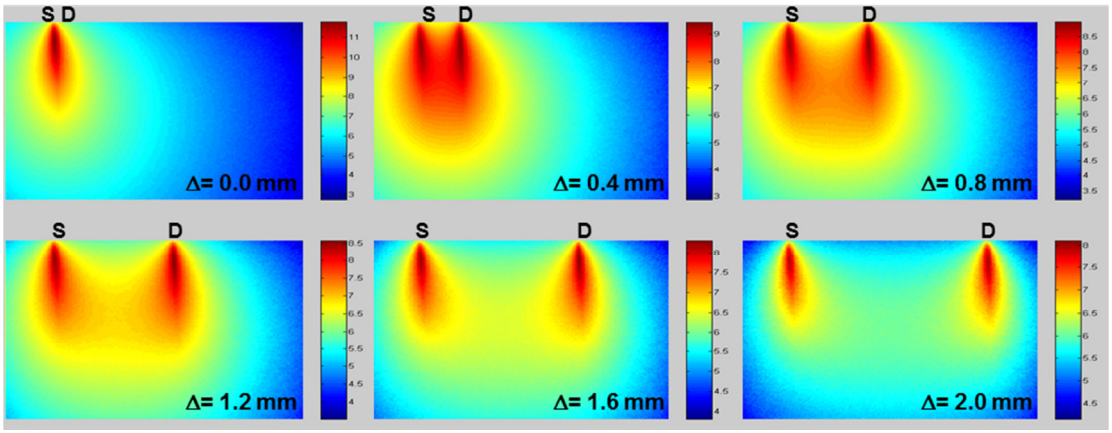

Figure. 10 Monte-Carlo simulated measurement sensitivity distribution of FLOT measurements (log scale). [8]

Tissue geometry was 3 mm (lateral) by 2 mm (depth) with scattering coefficient $\mu_s = 8\ \mathrm{mm}^{-1}$ for excitation and $7\ \mathrm{mm}^{-1}$ for emission ($g = 0.9$).

2.5 **Comparing different reconstruction approaches**

Comparing different reconstruction approaches was briefly investigated. Figure. 11 compares 4 different approaches. Stacking is the fastest approach to represent the tomogram because no W is involved. Tikhonov and SIRT are two linear approaches. EM is one non-linear approach. One lesson that all approaches gave similar results is that it is as critical to take good, reliable measurement as to perform any reconstruction approaches.

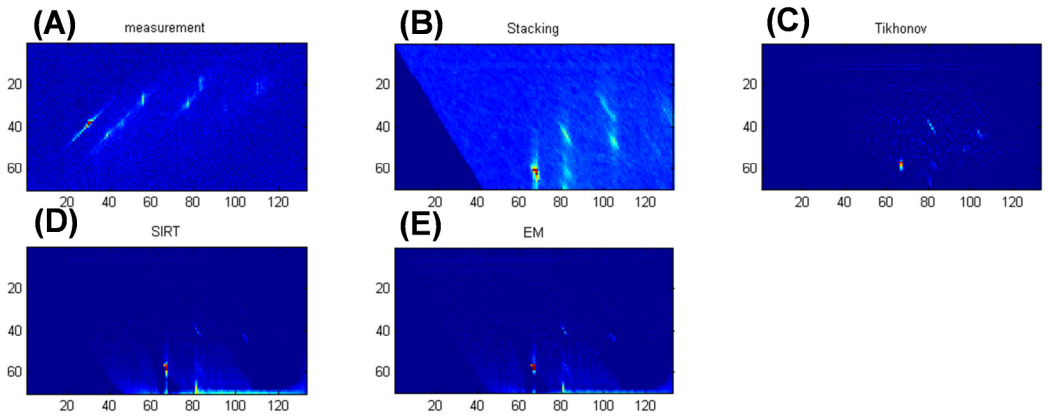

Figure. 11 Compare stacking, Tikhonov, SIRT, and EM.

(A) One raw measurement. (B) Stacking. (C) Least square inversion using Tikhonov regularization. (D) SIRT: Simultaneous iterative reconstruction technique. (E) EM: Expectation-Maximization.

2.6 **Formation of the tomogram**

The theory is developed for 3D reconstruction. However, in this thesis, because the line illumination is implemented, 3D photon distributions as well as sensitivity profiles are later projected to 2D. The reconstructed image represents a local 2D ZX cross-section of the sample as shown in Figure. 11. Tiling these 2D cross-sections formulates the 3D tomogram. This section details the tiling process and the specification of each local 2D tiles.

With the convention that illumination line (wavefront) is along Y axis, or illumination direction lying in ZX plane (See Figure. 6), the acquired data cube is a series of YX images. More specifically, Y represents vertical columns and X represents horizontal

rows. Because the sample is translated[7], the illumination position is still in certain columns[8]. Each row records a light distribution consisting of the intensities of a confocal spot and other peripheral neighbors, which can be reconstructed into one depth-resolved profile of the sample, or an A-scan, representing a depth (Z) profile at certain (x,y) position. Since the sample is scanned along X, a series of A-scans forms a B-scan image representing a ZX cross-section. Finally, all other rows lie at different Y positions. Juxtaposing all B-scan images constitute the C-scan image, volumetrically represents a tomogram of the sample.

It is possible to use multiple light distributions to directly reconstruct B-scan or even C-scan images, depending on the computation memory. In this thesis, where line-scan aFLOT was constructed, 70 line distributions, each of which is also 70 pixels long, were used simultaneously to reconstruct a 2D local tile. In other words, $70 \times 70 = 4900$ measurements were used to reconstruct a ZX cross-section. The size of this ZX cross-section can be arbitrarily specified. For example, the ZX cross-section can be described using 100 or 10000 pixels. However, only a certain amount of pixels can be rendered meaningfully. Other pixels merely represent noise. Whether a pixel represents a meaningful fluorescence or meaningless noise depends on which spatial location the

[7] As long as illumination light and the illuminated sample have relative motion, aFLOT will work. Alternative to this instrumentation, another way is to translate the illumination beam, such as [MEFT, JBO 046005]

[8] It is fixed if the surface of the sample is flat. If not, the illumination position shifts correspondingly. In this sense, aFLOT is naturally a topography technique. More aggressively, aFLOT also intends to resolve information below the sample surface.

pixel represents. In this thesis, the reconstructed ZX cross-section was represented by a grid map. Each pixel represented the fluorescence intensity in an equally-distant area. The pixel size and the number of pixels are predefined. For example, one may choose the pixel to have size of 40μm and 70×70 pixels to form a ZX FOV of $2.8 \times 2.8\ \mathrm{mm}^2$.

However, apparently, FLOT (and other optical systems) is more sensitive to fluorescence close to the surface than underneath, and the penetration depends on the scattering of the sample. It is therefore wiser to address the region within penetration depth using more pixels. Also, fewer pixels should be used to describe regions beyond. One future work can be to implement the mesh method. As a result, the reconstruction can benefit from dynamically assigning the size for each meshed area and allocating the required number of pixels.

2.7 **Summary**

The goal of this chapter was to derive Equ.14. Equ.14 gives us a clue about how to relate the fluorescence measurements F to fluorophore distribution O through a sensitivity matrix W. One can transcribe the information about the optical properties of the imaged subject into W. More importantly, one also has the freedom to design, configure, or manipulate the system about how the measurements are taken. (Again, one can transcribe the information of such design into W). The purpose of the next chapter is to explain how to maximize the amount of information in W that can be gained by the angular degree of freedom.

In this thesis, once the configuration of the system and optical properties of the sample were known, Monte-Carlo simulation generated W numerically. W was normalized so that each measurement is equally important. The SVD decomposed W into USV^T. The reconstruction was performed under the scheme of Tikhonov regularization. A regularization parameter was estimated using criteria of either the L-curve or discrepancy principle. Then the solution O, representing a local ZX cross-section, was calculated using Equ.12. The hard constraint was post-imposed by replacing all pixels with negative values with zeros. Lastly, all local cross-sections were tiled to form a global tomogram.

3 The Angular Degree of Freedom: Simulation and Implementation

A qualitative explanation about the effect of the oblique illumination/collection is given in section 3.1. To establish a quantitative description, the concept of the measurement configuration is defined in section 3.2. In section 3.3, based on the concept, theoretical singular value analysis (SVA) was performed to evaluate the ability of an optic system to acquire the amount of information about the imaged sample. In section 3.4 the PSF of the proposed system, aFLOT, was estimated using Monte-Carlo simulation to support the result from SVA. Instrumentation of aFLOT is given in section 3.5. Data acquisition is given in section 3.6. Other degrees of freedom are discussed in section 3.7. A summary is given in section 3.8.

3.1 Qualitative explanation of the effect of oblique illumination/collection

In FLOT, both source and detectors are arranged perpendicular to the sample surface. The degree of freedom that can be manipulated is the distance between the source and detector, known as source-detector (SD) separation. The wider the SD is, the longer the photons on average travel, the deeper the fluorescence origin is probed. One assumption is that the sample must scatter. If the sample is otherwise transparent, FLOT would fail to infer the depth of fluorescence origins in principle. In other words, FLOT has poor depth selectivity in low scattering cases because the probing depth is insensitive to SD. Again,

one can see that in Figure. 6, interpreting the depth from SD fails when the source and the detector are normal, which is the configuration of FLOT.

The key reason for the counter-intuitive inability is that its source and detection paths do not intersect. Except SD=0 where source and detector paths are fully overlapped, in every other SD≠0, source and detector paths are parallel. FLOT relies on the uncontrollable scattering of the sample to perform the reconstruction.

Oblique illumination/collection effectively tackles the problem of poor depth selectivity in low scattering applications. The idea was firstly proposed and implemented in confocal theta microscopy (CTM) in 1994 by Ernst Stelzer [28] in an attempt to improve resolution. The spirit of CTM is the following observation: "The PSF of the pinhole is an ellipsoid, several times as long as it is wide. This limits the axial resolution of the microscope. In CTM the cone of illuminating light and detected light are at an angle to each other (best results when they are perpendicular[9]). The intersection of the two PSFs gives a much smaller effective sample volume." Later, work in optical spectroscopy also suggested that using angled illumination-collection fiber design would enhance the depth selectivity of epithelium tissues [29-33]. Recently, systems that take advantage of oblique illumination/collection including confocal theta line-scanning microscopy and selective plane illumination microscopy (SPIM) were developed [22, 34]. Both resolution and

[9] Because of the possible scattering of the sample, the symmetry of PSF may be destroyed axially. As a result, a 60° intersection angle gives the best performance according to our simulation.

depth selectivity were explicitly recognized. Figure. 12 illustrates the depth selectivity obtained by the oblique illumination/collection. "…normal incidence case tends to collect fluorescence originating from a range of depths … yet when light is delivered or collected at an oblique angle, the cone overlap volume shrinks to a region close to the surface. [3]" More clearly, comparing (c,f), one can see that the depth is selected by selecting the SD.

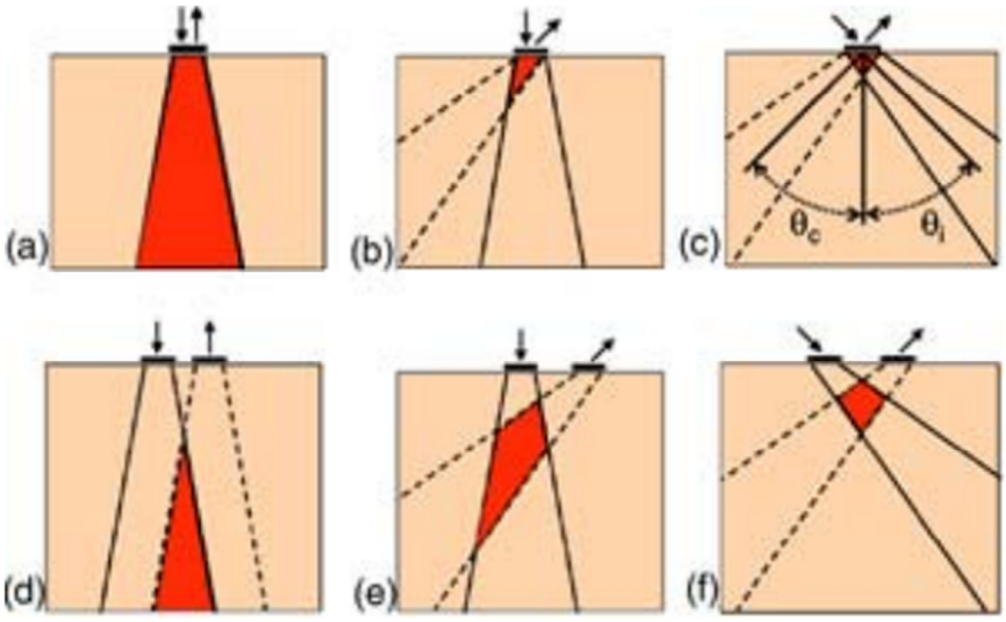

Figure. 12 Illustration of illumination (solid lines) and collection (dashed lines) cones for normal- and oblique-incidence geometries.

Darkened areas indicate the regions of overlap, and thus maximum sensitivity. Reproduced from [3]

In this thesis, the idea of the oblique illumination and detection is introduced to FLOT. The source and detection paths intersect intentionally. As a result, aFLOT combines several advantages and wisdom from other optic systems. First, as in CTM, the size of

PSF reduces, so the resolution is improved. Second, as in SPIM, the fluorescence signal is spatially selectively excited, so the depth selectivity is improved. Because of this feature, the stacking representation is enabled (section 2.3.5). Third, as in FLOT, scattering is another mechanism to estimate the depth of fluorescence origins using the SD. One can transcribe the information of scattering of the sample into the reconstruction process.

3.2 Measurement Configurations

To evaluate the ability of an optic system to acquire the amount of information about the imaged sample, the concept of measurement configurations is defined here. One measurement configuration is referred to as a scalar measurement of light intensity per source position per source angle per detector position per detector angle. In this thesis, only the positions and angles of the source and detectors are considered. Other degrees of freedom are not considered but possible. See section 3.6.

Each unique source-detector arrangement is considered as a measurement mode. One designs where to place the source (illumination light), where to place the detector, what the source's incident angle is, and what the detector's detection angle is. Conducting multiple measurements using the same arrangement is equivalent to increasing the exposure time. Therefore, it is not considered a different source-detector arrangement.

The number of measurement configurations is physically limited. For example, [15] used 7 individual fiber channels as detectors, meaning intensities from 1 confocal spot and 6 neighboring spots can be acquired per illumination position. If there are 100 illuminations

positions, $7 \times 100 = 700$ measurement configurations are established. (Remember the positions of the source and detector can be separately configured, thereby having 2 degrees of freedom.) EM-CCD was used as a detector array where each pixel is considered a detector. In this thesis, even though the EM-CCD was a 2D array ($1002 \times 1003\ pixels$), only 70 pixels in X direction were used to record the confocal and peripheral fluorescence intensities. Along with 70 illumination positions (by translating the sample), 4900 measurement configurations were used for the Tikhonov reconstruction. (See section 2.6)

Compared to the approach of using multiple fiber channels to form a detector array, EM-CCD has the advantage that the number of pixels (or SD) is usually more than sufficient (7 vs. 70). However, it appears that 1002 SDs in our EM-CCD are available per illumination position and/or angle. Why only 70 SDs were used? This is limited by the computation memory for the Tikhonov reconstruction. After multiplying the number of illumination positions, 4900 measurement configurations require the manipulation of matrices having size of 4900×4900, for example, singular value decomposition. However, if the reconstruction is not necessary or the stacking suffices, one is not limited by 70 SDs.

Given the condition that the number of measurement configurations is limited, the design of source-detector arrangements becomes important. The goal of designing the arrangements is to acquire as much information as possible. Singular value analysis is an approach to measure the amount of information obtainable.

3.3 **Singular Value Analysis (SVA)**

SVA is an approach to quantitatively measure a linear system's ability to acquire the information about the imaged sample. SVA has been demonstrated in the optimization of DOT to achieve a favorable image resolution [35, 36].

After designing the source-detector arrangements, the ZX sensitivity profile (such as Figure. 10) of each arrangement is generated using Monte-Carlo simulation. If the profile is described using 3000 pixels (section 2.6), the vectorized profile is therefore a row having size of 3000 entries. 4900 measurement configurations constitute 4900 rows and therefore a sensitivity matrix W having size of 4900×3000 (Equ.11).

The procedure of SVA is to singular value decompose W, yielding a triplet of matrices: $[W]_{M\times N} = [U]_{M\times M}[S]_{M\times N}[V]^{T}_{N\times N}$ where the diagonal entries of $[S]_{M\times N}$ is the singular value spectrum of the system, which provides a measure of the relative effects of these image-space modes on the detected signal. The singular values are arranged in magnitude-decreasing order with increasing image-space mode indices. The spectrum is therefore a signature of the system.

By saying one system is better than one other, one shows that the spectrum is generally higher in magnitude than the others'. One should however normalize W before the comparison. For example, a W that is simulated by using 10^{10} photons is different from one by using 10^{8} photons. The number of photons used is equivalent to how long a sample is exposed under illumination during measurement. The effect of longer exposure

is to shift the spectrum upwards. In other words, every singular values is multiplied by a constant factor. Therefore, the comparison emphasizes the shape of the spectrum.

The W however should not be normalized by keeping the number of photons (or the energy shone on the sample) constant because adjusting the illumination power is usually flexible. In this thesis, the normalization is to divide all singular values by the first singular value so that the normalized spectrum has 1 in its first entry. As a simple example,

$$\begin{cases} W_{system\ 1} = \begin{bmatrix} 1 & 0 \\ 0 & 0 \end{bmatrix} \rightarrow \ normalized\ diag(S_1) = [1\ 0] \\ W_{system\ 2} = \begin{bmatrix} 2 & 0 \\ 0 & 0 \end{bmatrix} \rightarrow \ normalized\ diag(S_2) = [1\ 0] \\ W_{system\ 3} = \begin{bmatrix} 1 & 0 \\ 1 & 0 \end{bmatrix} \rightarrow \ normalized\ diag(S_3) = [1\ 0] \\ W_{system\ 4} = \begin{bmatrix} 1 & 0 \\ 0 & 1 \end{bmatrix} \rightarrow \ normalized\ diag(S_4) = [1\ 1] \end{cases}$$

System 1 and 2 acquires the same amount of information except that the exposure time of system 2 is doubled. System 3 performs duplicated measurements, effectively the same as system 2. Designs of system 1 to 3 essentially take advantage of only 1 measurement configuration even though 2 are available. Only system 4 fully uses 2 measurement configurations. With this understanding, an optimized system should have a spectrum whose shape is as uniform as possible. This task is however non-trivial. Singular values usually span several orders of magnitude [21], meaning the spectrum can be steep. (Remember that the spectrum is monotonically non-increasing.) During the reconstruction, the inversion of $F = WO$ involves dividing F by singular values. It is therefore foreseeable that if some singular values are small, some pixels in the

reconstructed O would be unstably large. This is exactly the reason to apply regularization to avoid the division by any small singular values. (Equ.12) For the same reason, a threshold corresponding to the dynamic range of the detector array will be set to cut off any singular values below the threshold. In our EM-CCD, the dynamic range is 12 bit. The threshold was set to be $2^{-12} = 10^{-3.6}$.The useful singular values are singular values above the threshold. The number of useful singular values is collected and is a measure of the amount of information obtainable.

The SVA applied in this thesis focuses on the enhancement due to the oblique illumination incidence angle and the detector's detection angle. Therefore the spectrum of aFLOT is compared with that of FLOT. The source incidence angle and detector detecting angle were varied. Even though in practice both angles may vary independently, because the sample can rotate freely, what's more important is the intersect angle between the illumination and detection axis. Without loss of generality, I studied systems where both angles are equal.

Figure. 13 shows the 3 representative sensitivity profiles of FLOT and aFLOT under different background scattering (μ_s= 5, 10, and 15 mm^{-1}). Configurations with 0^o (top row) and 30^o (bottom row) incidence and detection angles showed distinct sensitivity patterns. 30^o is the angle for both illumination and detection, giving a 60^o intersection. Photon paths can be seen more ballistic for low-scattering medium (μ_s= 5 mm^{-1}) but became more scattered in high-scattering medium ($\mu_s = 15\, mm^{-1}$). The intersection can be seen clearly for the 30^o aFLOT system below $\mu_s = 15\, mm^{-1}$. Beyond, the

intersection was destroyed by high scattering. The disappearance of the intersection breaks down the stacking representation.

To be general, the criterion for enabling the stacking was speculated to be one mean (reduced scattering) free path (MFP). Under the background ($\mu_s = 15\ \mathrm{mm}^{-1}$, g=0.9), the $\mathrm{MFP} = \frac{1}{\mu_s'} = \frac{1}{\mu_s(1-g)} = 0.67\mathrm{mm}$. In Figure. 13, one can qualitatively see that the penetration depth was indeed about one MFP long.

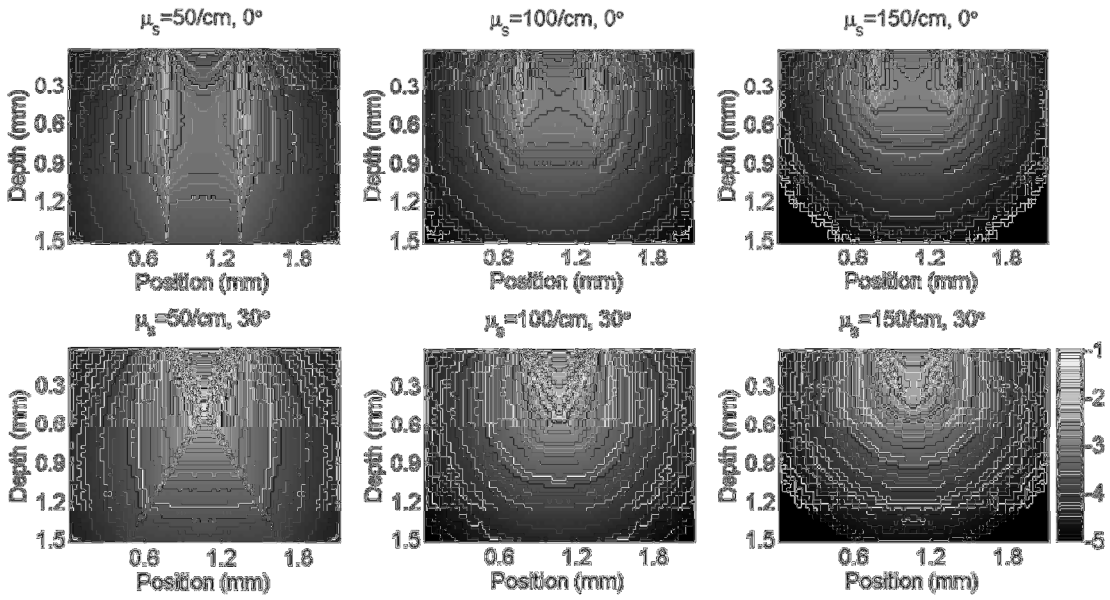

Figure. 13 Sensitivity maps (in log10 scale) for source-detector pair with 0° (top row) and 30° (bottom row) incidence/detection angles. [4]

For each configuration, different scattering coefficient is specified for the medium (left to right). The sensitivity map indicates the probability density of photons delivered to the location by the source and captured at the location by the detector.

Besides, to answer which angle performs best, singular value spectra were generated for each angle from 0^o to 50^o with 10^o increment and plotted in Figure. 14. (A-C) correspond

to different background scattering coefficients (μ_s= 5, 10, 15 mm^{-1}, respectively). Note the dash line was plotted at $10^{-3.6}$ to represent the threshold. Figure. 14(D) plots of the number of useful singular values against angles and scattering coefficients. 30° aFLOT exceled among other configurations, especially in low scattering medium. It also showed that the angular advantage diminished with increasing scattering. Again, this is because photons lose directionality faster in highly scattering medium. Therefore, both source and detector become more isotropic. Besides, going higher than 30° angle did not give more useful singular values is understandable. To extreme, if both illumination and detector are 90°, facing each other, no photons enter the sample and so the system probes simply no information.

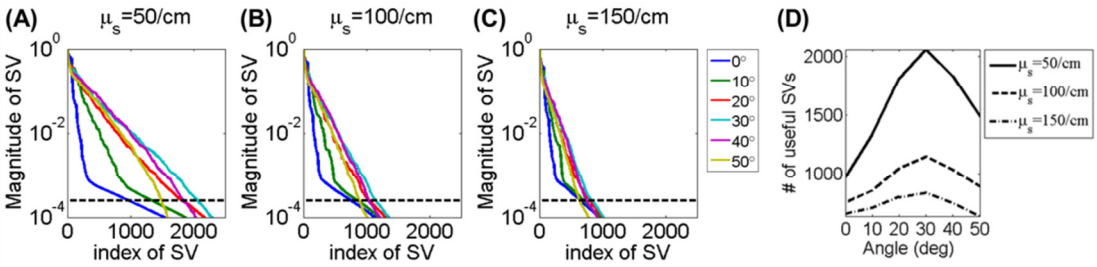

Figure. 14 Comparison of singular value (SV) distributions among different incidence/detection angles. [4]

For convenience, same incidence and detection angels are specified. (A) SV distribution for μ_s=50 cm^{-1}; (B) SV distribution for μ_s=100 cm^{-1}; and (C) SV distribution for μ_s= 150 cm^{-1}. Detection threshold was specified as $10^{-3.6}$ (dotted horizontal lines in A-C). Only SV above the threshold was considered carrying useful information for image reconstruction. (D) Plot of the number of SV above the threshold. FLOT arranged in 30° exceled from other arrangements. It also showed the decrease of the angular advantage with increasing scattering.

3.4 **PSF simulation**

To independently validate the results from SVA, image reconstruction of a point object (with intensity equal to 1) was performed under different configurations. The simulated measurement was added with 1.5% Gaussian-distributed noise[10]. The point spread function along axial (z) direction through the position of point object was quantified at every depth of the object. The details of PSF_z were further analyzed using two parameters: 1) the reconstructed peak intensity (or depth sensitivity); and 2) the interquartile range (IQR).

Figure. 15(A-D) shows the PSF_z peak intensity (or depth sensitivity) verses depth for different configurations. In general, at a given depth, the 30^o configuration had higher peak intensity (sensitivity) than 0^o configuration, especially in the shallower depth region. The difference becomes less prominent for a highly scattering medium. It is interesting, however, that when normalizing these sensitivity curves in units of MFP ($1/\mu_s'$) (i.e., replacing d with $\mu_s' d$ in *x*-axis of the plot), only 30^o configurations grouped together, as shown in Figure. 15(D). The result that curves of FLOTs were not unified indicates that the underlying mechanism of depth selectivity between aFLOT and aFLOT was different. One speculation is that photons significantly rely on backscattering to travel from source to detector in FLOT, while aFLOT can additionally rely on the intersection of the incidence and detection paths. When normalized to MFP, that curves unified in aFLOT

[10] Because the measurement is fluorescence intensity, to satisfy that it must be non-negative, measurements that are negative caused by the added noise are set to zero.

when MFP<1 indicates depth selectivity due to the geometrical intersection is a linear process, and that curves not unified in FLOT indicates depth selectivity due to the (multiple) scattering is a non-linear process. [4]

Figure. 15 (E-H) plot the IQR of PSF_z against depth. In general 30^o configuration had smaller IQR (higher axial resolution) than 0^o configuration. This agrees with the theory of CTM or SPIM. Especially, in low scattering medium, IQR for 30^o configuration remained 30 μm up to 1 mm, and remains <100 μm up to 1.5 mm. In contrast, IQR for 0^o configuration increased rapidly to ~400 μm at 1 mm. Note that 30 μm was the pixel size. So the estimated size of true PSF_z might even be smaller. However, the difference between these two configurations becomes less prominent as the background scattering increased, and the IQRs for both configurations were almost identical for high scattering medium. Again, when normalized to MFP as shown in Figure. 15(H), unified curves were observed. However, different from the sensitivity, unified IQR curves occurred for both FLOT and aFLOT. This result indicated that IQR and sensitivity provide inherently different measures. [4]

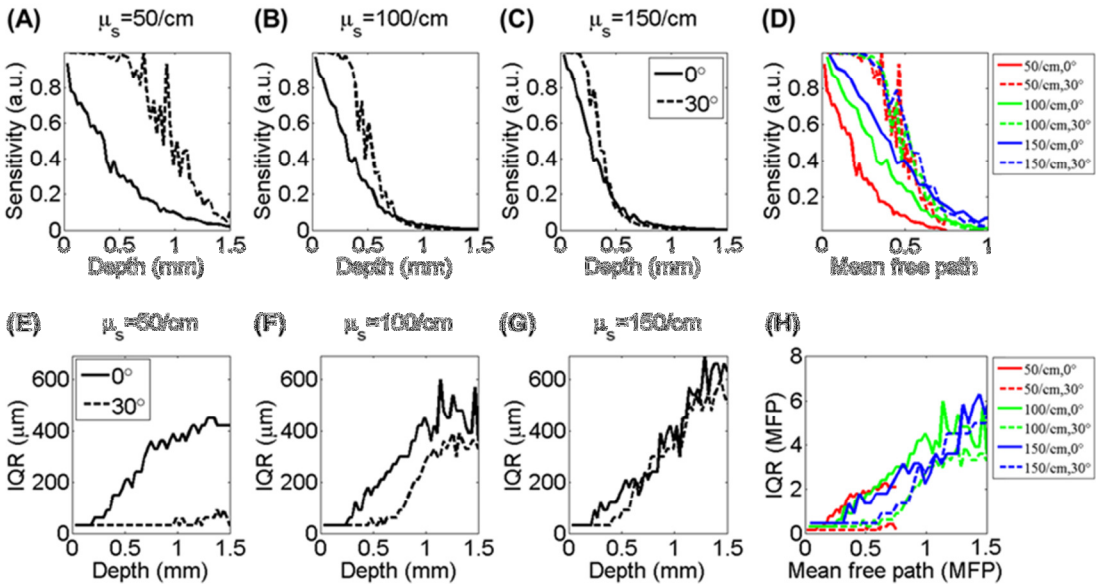

Figure. 15 the peak intensity and iterquartile range of PSFz verses depths.

(A-D) PSFz peak intensity verses depth for different source/detector angle configurations and background scattering. (E-H) PSFz interquartile range (IQR) verses depth for different source/detector angle configurations and background scattering.

3.5 **Instrumentation**

The critical component for FLOT and aFLOT is the array of detectors. That the array acquires a fluorescence distribution, not only scalar fluorescence intensity, enables the 3D reconstruction. In this thesis, the EM-CCD (sensicam em, Cooke, Germany) was used to satisfy this requirement. Though expensive, it provided several advantages. First, it had size of $8.03 \times 8.02\ \text{mm}^2$. The large size is one approach to simplify the mechanism of image formation. For example, one can simply use a 2D camera to form an image, or one can use a photodiode paired with 2 galvanometers to form an image. Second, because each detector/pixel reads signal simultaneously, it provides higher imaging speed,

compared to raster scanning a point across the image. Third, individual small detector/pixel (8 μm in our EM-CCD) preserves the sub-millimeter resolution. While CM and CTM may use an even smaller pinhole, for example 100μm, to reject off-focused light to appreciate obtainable sub-micron resolution, the common size of each individual pixel in the EM-CCD is sufficient for mesoscopic resolution.[11] Fourth, scattered fluorescence emerged from sub-surfaces requires the detector to have high dynamic range (DR). The EM-CCD had 12 bit DR. In chapter 4, I will point out that one future work is to implement evener higher DR. For this 12 bit DR EM-CCD, it was characterized in chapter 4 that 1mm penetration depth can be routinely achieved in biological relevant samples. Fifth, the EM-CCD had quantum efficiency above 45% between 450-800nm, sufficient for common fluorescence imaging. Sixth, the architecture of EM-CCD has the gain register before the analog-to-digital converter reduces the readout noise from common $5e^-$ to less than $1e^-$. Also, because of the gain register, one can locate a better DR window to fully use the 12 bits of the EM-CCD.

The other novelty of aFLOT over FLOT is the implementation of the oblique illumination/detection, which further improves resolution and depth selectivity for each

---

[11] To see why the size of pixel or pinhole affects resolution, one can hypothetically consider a huge pixel having size of 100 μm for example, which is 10 times larger than the typical. With such a large pixel, there is no need to optically design small PSFs because a significant amount of off-focused signal is integrated with the focused/targeted signal. The inability to differentiate focused from off-focused signal reflects the blurring. Equivalently, resolution degrades.

individual detector. It is possible to implement the task using a single objective [34]. However, to obtain an appreciable angle, the implementation here separated the illumination and detector arms. The separation demanded additional optics but saved a dichroic mirror. Both arms are implemented in the 4f structure.

Figure. 16 shows the schematic diagram and the photo of two aFLOT systems, which only had the different detection angles. In the illumination arm, the excitation light source (laser diodes, wavelengths varied) was collimated using a spherical lens (f=60mm, AC254-060-C, Thorlabs), passed through a polarizer (P), and expanded into line-field illumination using a cylindrical lens (CL, f=75mm, LJ1703L1, Thorlabs); in the detector arm, the fluorescence signal passed through an objective (varied), another polarizer, an emission filter (F, varied, depending on fluorophore spectrum), an eye-piece (varied), and reached the EM-CCD. A stage (CMA-25CCCL, Newport) was used to translate sample. This design was similar to the early development of confocal microscopes. It was mainly for simplifying the optics.

The purpose of the pair of polarizers was to reject the specular excitation light that may leak through the emission filter. By fixing the orientation of one polarizer, the other polarizer was rotated to minimize the detected intensity. Because fluorescence was spontaneously emitted, the polarization state was partly different from that of excitation light.

To improve the quality of line illumination, an iris and a diffuser can be used. In the illumination arm, both were placed immediately after the fiber output couple. The iris

improved the shape of the line. The diffuser made the illumination uniform (flat topped instead of Gaussian) along the line.

To improve the quality of measured signal (precisely to reduce the out of focus aberration) another iris placed between the objective and the eye-piece in the detection arm can help. Excited fluorophores away from the focused plane suffered from out of focus more. Reducing the size of the iris also reduced the size of PSF. More, the size of PSF away from the focused plane reduced faster than that close to the focused plane. For one reason, reducing the size of iris improved the resolution. For the other, acquiring multiple measurements using different sizes of the iris is an approach to modulate the PSFs of aFLOT. The drawback of reducing the size of the iris is the reduced fluorescence signal. If one can modulate the PSFs, one may be able to combine the advantages of high signal from a large opening and high resolution from a small opening. (Appendix 2)

Lastly, 3 optional translation stages are helpful. The sample was placed additionally on a z stage, which was able to adjust the height of the sample so the sample was focused under the objective. The place a focused illuminating line on and sample and within the FOV of the objective, the illumination arm was also mounted on an xz stage.

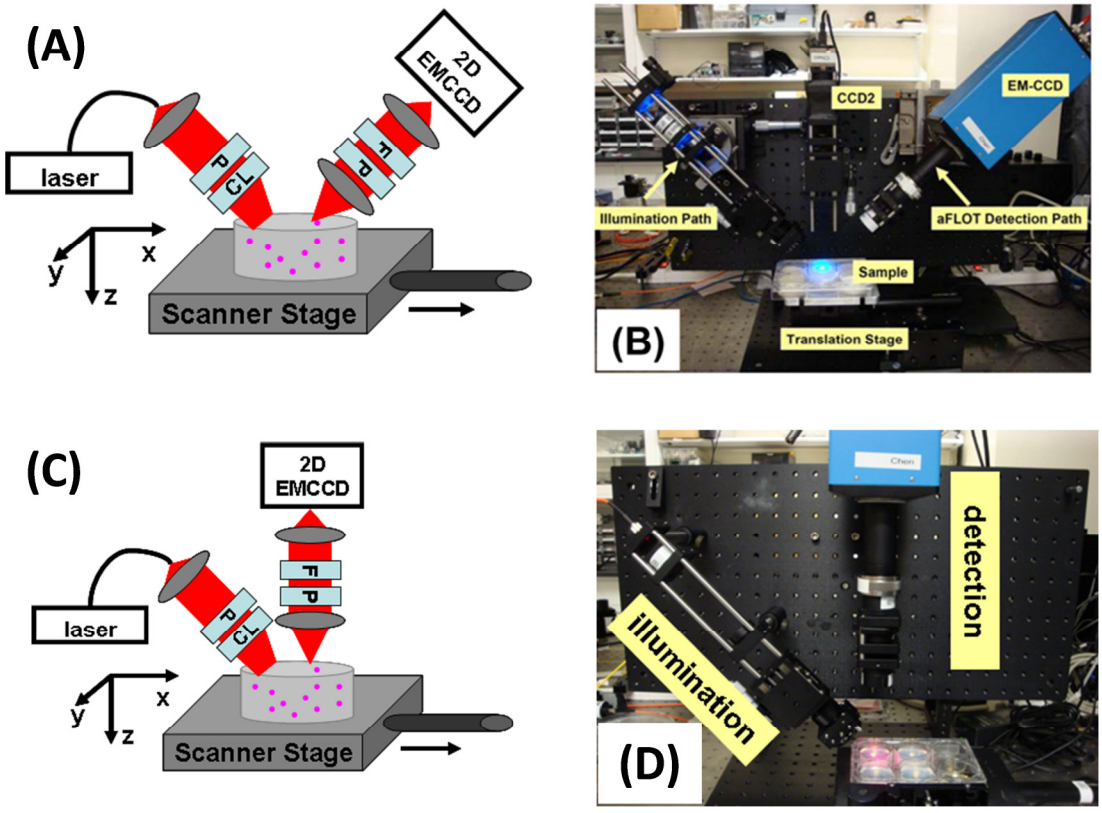

Figure. 16 Schematic and photo of two aFLOT systems.

CL: cylindrical lens. F: filter. P: Polarizer. CCD2 is used as the reflectometry to estimate the reduced scattering coefficient of the sample.[6] (A, B) the illumination/detection arms are arranged at 45° in air (or 30° inside the sample assuming an index of refraction of 1.4), suitable for low scattering applications. (C, D) Only the illumination arm is at 45° in air, suitable for high scattering applications.

3.6 **Data acquisition**

Before the data acquisition, the sample was placed under the objective and focused by adjusting the height of the z stage. The excitation power was controlled around 10-20 mW. The illuminating line was translated so that the line was focused on the sample surface and in the central FOV of the objective. Image preview was turned on to adjust

the polarizer so the specular excitation was minimized. The EM-CCD gain was adjusted so that the 12-bit DR was used as much as possible. Yet, it is critical for the reconstruction not to saturate the EM-CCD (section 4.2). Gain between 2-20 was typically used, depending on the fluorophores used. Lastly, data acquisition was in the dark room to avoid any light interfering with the fluorescence signal.

Two datasets were acquired. One was fluorescence signal and the other was reflection. These two were co-registered. To achieve co-registration, a script was designed for the automation. The routine of the script was

1. to translate the sample constantly in X-direction,
2. to record a sequence of YX images, and
3. after recording, to save data and translate the sample back to the original position.

To record the reflection (for the structural information of the sample and for estimating the reduced scattering coefficient), the emission filter was removed. The high illumination power usually saturated the EM-CCD. Both gain and illumination power were reduced before starting the script again.

The scanning speed was determined by the image pixel size[12] and the exposure time. For example, if the image pixel size is 20 μm and the exposure time for each frame is 0.2s,

[12] The pixel size of the EM-CCD is 8μm. The optics usually provided additional magnification M. Therefore, the image pixel size is the mapped size $8 \times M$ μm on the sample.

then the scanning speed is 20/0.2 = 40 $\mu m/s$. EM-CCD recorded a sequence of YX frames. The raw measurement was therefore a 3D data cube structured as YXS. The "S" dimension corresponds to the line scanning during translating the sample. Typically, each YX frame had size of 500×500 pixels and 300-700 frames (scans, or S) were acquired, so YXS had size of $500 \times 500 \times (300\sim700)$ voxels. Because the scanning speed was specified in the above convention, the voxel size was isotropic.

If only the stacking is required, the reflection measurement can be omitted. If the reconstruction is required, 70 pixels that covered the excitation position on the sample in X direction was extracted (so the processed YXS had size of $500 \times 70 \times (300\sim700)$). For example, if the procedure above is followed so that the illuminating line is in the central FOV, then the extracted 70 pixels are from pixel 250 to 319.

The YXS is the data that is ready for either the stacking or the reconstruction. See section 2.6 for the formation of the tomogram.

The total acquisition time was about 6 minutes (3 for fluorescence and 3 for the reflection) for a $3 \times 3 \times 3$ mm^3 tomogram, depending on how laterally wide the tomogram was.

The interface that the automation script coordinates with is described in appendix 1.

3.7 **Other measurement configurations**

In this thesis, aFLOT was implemented with a fixed angle configuration. Angled compounded configuration can be implemented and may perform as well as aFLOT. Figure. 17 shows a simulation comparing the performance among FLOT, 30° aFLOT,

and angle compounded FLOT. The evaluation metric is the singular value spectrum. A better set of configurations gives an evener (section 3.3). The comparison kept the same number of photons (or constant power) and the same number of measurement modes. Observations in Figure. 17 include

1. Conventional FLOT has the worst performance. The spectrum dropped significantly in the very beginning until index ~300.
2. Angle compounded FLOT performs slightly worse than 30° aFLOT, but it appeared to be more resilient to scattering than 30° aFLOT. As scattering increases, the spectrum of 30° aFLOT decreases dramatically.
3. 30° aFLOT performed the best, suggesting that the photon budget is wiser used in 30° aFLOT than other two systems.

Besides, rotational measurement configuration has been investigated. [12]

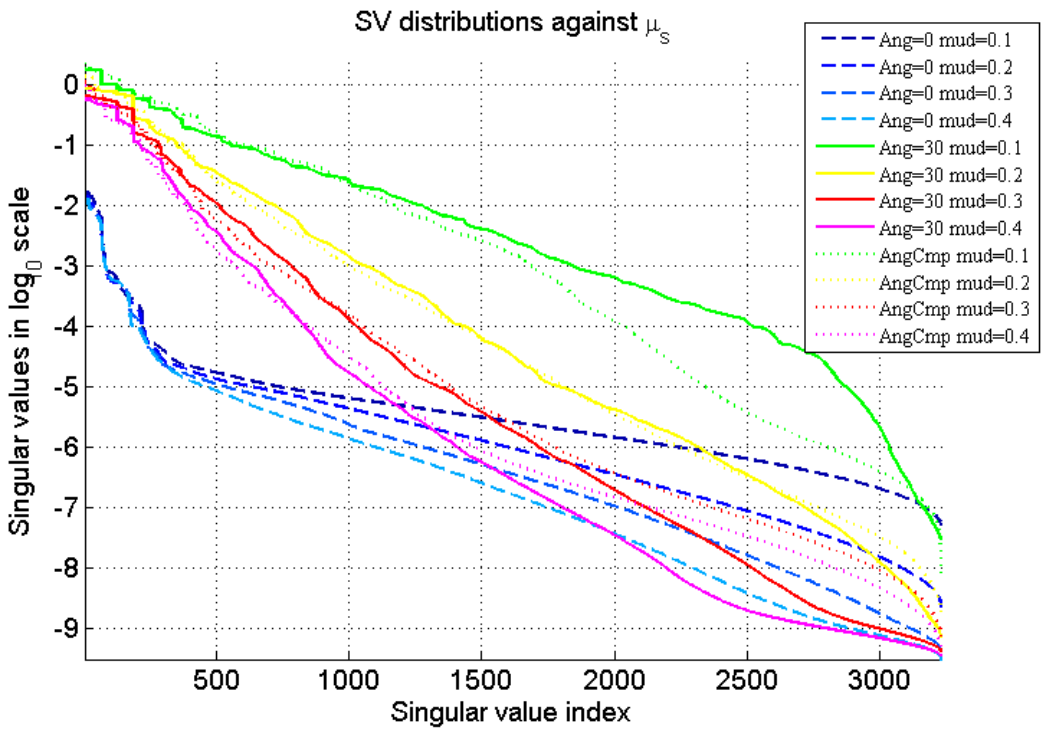

Figure. 17 30° configuration vs. 0° and angle compounding configurations.

The metric is singular value distribution. 0° configuration (dash line), as is FLOT, performed the worst. Angle compounding configuration (dot line) appeared resilient to scattering. 30° configuration (solid line) performed the best but appears vulnerable to scattering. mud is scattering coefficient normalized by mean free path. The compounded angle ranged from 0° to 60°, but the total number of measurement modes was kept the same for all systems for a fair comparison.

3.8 **Summary**

The oblique illumination/collection was introduced to the technology of FLOT. As a result, aFLOT provided better imaging for low scattering applications. Essentially, the oblique illumination/collection improved the resolution and the depth selectivity. SVA

and PSF simulation supported the statement. In sections 3.3 and 3.4, it was pointed out that there were two mechanisms of depth selectivity. Scattering discriminates the depth for regions where MFP>1. Because discriminating depths even when MFP>1 is possible, the mechanism increases the penetration depth, which is otherwise thought difficult for high scattering applications. Depth selectivity relied on scattering, which however requires the sample to be scattering. Oblique illumination and detection to intentionally intersect axes provides depth selectivity within MFP<1 where the photon path remains ballistic. aFLOT can therefore rely on both to infer the depth of fluorescence origins, completing this technology from high to low scattering applications.

4 Experimental Characterization of aFLOT

Calibrated phantoms were imaged using aFLOT. Because the size, geometry, and depth of the features in phantoms were well-defined, the resolution and penetration depth of aFLOT were able to be characterized.

Two aFLOT systems were characterized. In chapter 2, I explained that the oblique illumination was exclusively advantageous when the sample is low scattering. Therefore, for low scattering samples, the configuration of 45° illumination - 45° detection (45°-45°) was preferred (Figure. 16A). For high scattering samples, 45°-0° configuration was preferred (Figure. 16B). The simulation in section 3.4 supported such arguments. In physics, the reason is that each photon loses directionality when the sample is highly scattering. Therefore, 45°-0° and 45°-45° configurations were comparable. 45°-0° configuration was further preferred because of two other reasons. First, the measured image could not maintain in focus over a few millimeter FOV if EM-CCD was placed at 45^{o}. The out of focus aberration would become severe. Second, arranging the detector arm to be normal to the sample surface gave a greater depth of field[13] in the z direction. Indeed, improving the resolution in z should be emphasized. Plus, one has been able to use fine scanning of tight illumination point or line to achieve high resolution in lateral x, y directions. There is no need to "waste" depth of field in lateral directions.

---

[13] A region where the sharpness of features is comparable.

45°-45° configuration was characterized in sections 4.1 and 4.2. 45°-0° configuration was characterized in sections 4.3-4.6. The summary is in section 4.7.

4.1 Capillary tube phantom in 1% Intralipid: comparing aFLOT with FLOT

Following the same idea in section 1.3.1, the capillary tube phantom was imaged again. The capillary tube (110 μm in diameter) was filled with 1 μM fluorescent dye Rodamine 6G (Rd6G) and embedded at 1.2 mm deep inside 1% Intralipid. The excitation wavelength was 532nm and the emission wavelength of the filter was 605±15 nm. Figure. 18(A) shows the cross-section of the reconstructed capillary tube phantom using aFLOT. The depth of the capillary cross-section from the reconstructed image was ~1.14 mm. Independently, OCT dictated ~1.2 mm. As a comparison between angled and conventional FLOT systems, Figure. 18(B) shows the reconstruction using FLOT with normal incidence/detection. Figure. 18(C-D) illustrate the central depth profiles of the reconstructed capillary tube. Quantitatively, IQR was measured and compared. The measured IQR was 178.5 μm for the aFLOT system and was 450 μm for the conventional FLOT. This represents approximately 2.5-fold improvement in axial resolution.

One note is that the reconstruction in FLOT was SIRT, but the reconstruction in aFLOT was Tikhonov. Therefore, the origin of this 2.5-fold resolution improvement needs some clarification. One factor was the oblique illumination, and the other was the reconstruction scheme. According to Figure. 11, Tikhonov appeared to be slightly better than SIRT, but cannot sufficiently justify the 2.5-fold improvement. Therefore, I

conclude that this 2.5-fold resolution improvement resulted from both a better reconstruction scheme and the oblique illumination/detection.

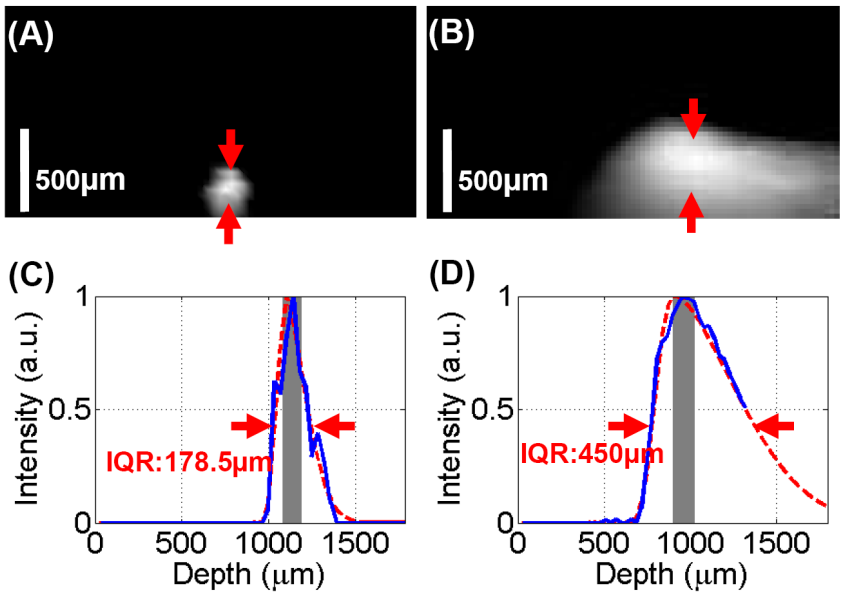

Figure. 18 Comparing the reconstructed capillary cross-section using aFLOT (A,C) and conventional FLOT (B,D). [5]

(A,B) cross-sectional reconstruction; (C,D) axial profile through the center of the object. Gray area denotes the true position and thickness of the capillary tube. IQR: Inter-quartile range. (B) the same result extracted from Figure. 2.

4.2 Capillary in homogeneous medium (Intralipid)

To obtain the penetration depth, the capillary tube (I.D=400 μm , Cat.1-000-800, Drummond Scientific Co.) was obliquely placed in a tank filled with intralipid. By changing the concentration of intralipid, different background scatterings were created. Specifically, the tank was filled with 72ml water in the beginning. Once the measurement

was acquired, 2ml from the tank was removed and 2ml 20% intralipid was added. Repeating the process gradually increased the amount of intralipid in the tank. The process was repeated until the volume concentration of intralipid reached 1.5%. Scattering coefficients were obtained by interpolating[14] the scattering coefficient of 10% intralipid [37]. The excitation wavelength and emission filter in this experiment were 532nm and 605 ± 15nm, according to the spectrum of the dye Rd6G.

Figure. 19 summarizes the cross-sections of the capillary at various depths and scattering coefficients. The cross-section was the stacking representation (because intensity would be saturated, disabling reconstruction. Discussion soon). All subplots are plotted in the same linear intensity scale. Because the capillary was placed obliquely, multiple depths can be acquired in one measurement. The columns in Figure. 19 only represent 6 depths at 0, 500, 1000, 1500, 2000, and 2500μm. The scattering coefficients acquired were from 0 to 9/mm. From low to high scattering, it can be observed that not only the intensity dropped, but the profile of the capillary cross-section became blurring. In terms of the same detectability, a red dashed curve is plotted. The curve empirically suggested the detection limit as a function of depth and scattering. For example, one can dictate that 2mm penetration depth was expected if the background scattering was 1/mm. This agreed with the theoretical predication. According to Beer's law, intensity would drop with a

[14] For example, the scattering coefficient of 1% intralipid was one-tenth of that of 10% intralipid.

factor 0.1353 ($= \exp(-penetration \times \mu_s) = \exp(-2)$). Given that our EM-CCD had a dynamic range of 12 bit, $2^{12} \times 0.1353 = 554$, comparable to our noise level.

However, penetration of only 2mm at scattering 1/mm still appeared to be shallow. This was caused by the constant short exposure time, the limited dynamic range and low gain of the EM-CCD across all subplots for a fair comparison. While increasing any factor would increase the detectability, another concern was the saturation of the EM-CCD. Keeping EM-CCD not saturated is critical. Expect stacking, any reconstruction schemes requiring description of sensitivity matrix need accurate (so not saturated) intensity distribution to perform reconstruction. Figure. 19 clearly shows that the dynamic range of the fluorescence intensity exceeded the 12 bit window of our EM-CCD. Therefore, using single constant exposure time and gain (as in this experiment), it appears impossible to keep EM-CCD not saturated for cases of low scattering and shallow regions while requiring the high detectability for cases of high scattering and deep regions at the same time.

Therefore, there is a dilemma in balancing non-saturation and detectability. This exposed a deficiency of the current (a)FLOT system. Due to the high dynamic range of fluorescence intensity from different depths, all fluorescence signals must be kept within the 12 bit window of the EM-CCD even at the image acquisition phase.

For future work, one idea can be to dynamically vary the exposure time and gain and to normalize the detected intensity by post processing. As the data precision can be 64 bit high in PC, it is therefore not necessary to be limited by the specification of the EM-

CCD. The idea virtually increases the effective dynamic range of the EM-CCD by sequentially shifting the 12 bit window to constitute the 64 bit data.

On the other hand, the current implementation of aFLOT still applies to simplified situations. For example, all the fluorescence signals come from comparable depths, not necessarily on the surface. Besides, if the scattering of the sample is low, the dynamic range of the fluorescence can be low as well. In either situation, a fixed exposure time and gain suffice.

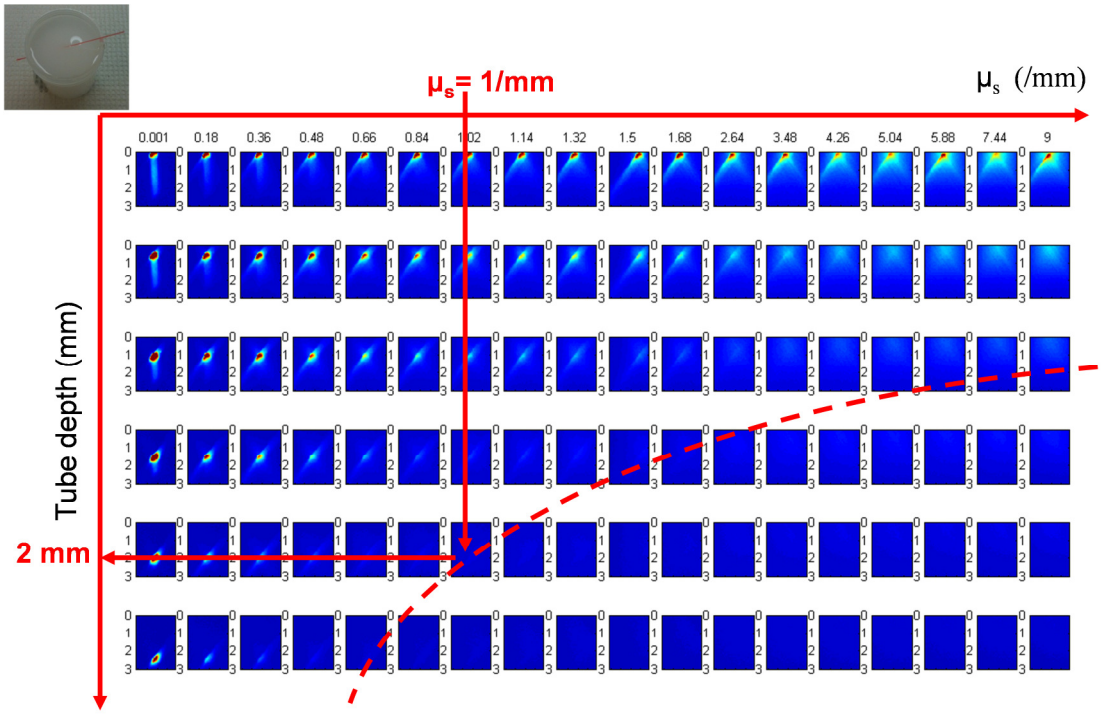

Figure. 19 detectability of the capillary cross-section vs. scattering and depth.

The top-left inset showed the imaged phantom, a capillary filled with Rd6G obliquely immersed in various concentrations of intralipid. Every subplot showed a cross-section of the capillary in a FOV deep to 3mm. Columns compare the detectability against depth. Rows compare the detectability against scattering. The red dashed curve may serve as a rule of thumb. For example, when the scattering $\mu_s = 1/\text{mm}$, one was able to detect the fluorescence down to 2mm deep.

4.3 **Layered PEG hydrogel**

To show the penetration depth can be longer in a low scattering environment, one 5-layered PEG hydrogel was fabricated. Layers with and without ICG 14.75 μM were alternatively fabricated. Each layer was about 3mm thick. Pure PEG hydrogel was almost transparent. The reduced scattering coefficient was $0.1/\text{mm}$. Figure. 20 shows the resulting image of the cross-section of the layered gel. Seeing the deepest interface of

layers suggested that 9 mm penetration was achieved. Again, low scattering is a prerequisite for long penetration. Because of low scattering, the dynamic range of fluorescence was kept narrow. The aFLOT measurement was therefore able to be free from saturation.

Besides, Figure. 20B also shows the effect of out of focus aberration. In the current implementation of aFLOT, the effect was considered as another deficiency. However, in appendix 2, I briefed an idea to take advantage of the aberration to improve the image quality. Therefore, in the future, the out of focus aberration is not necessarily inconvenient.

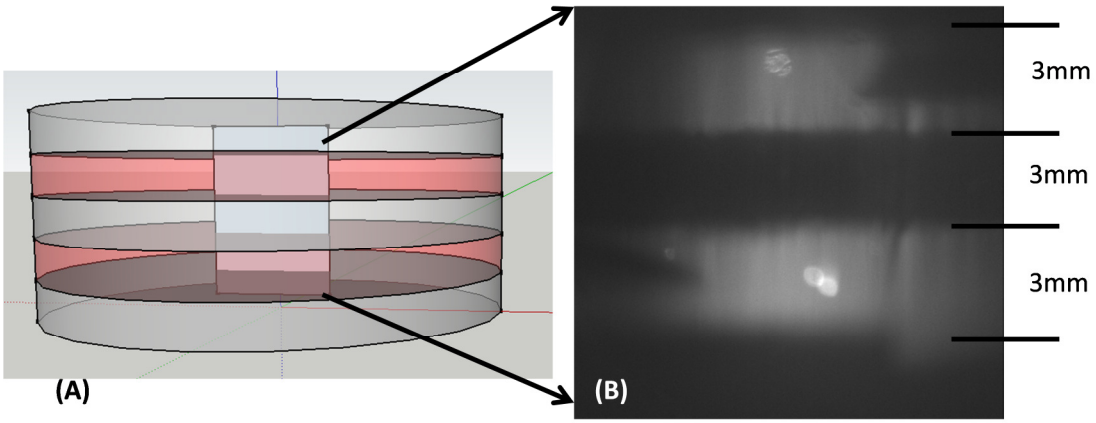

Figure. 20 Cross-section of a layered PEG hydrogel.

(A) Schematic of the layered hydrogel. Layers with and without ICG 14.75μM were alternating. Each layer was 3mm. (B) Acquired cross-section aFLOT image. Layers were clearly resolved. Out of focus aberration was also clear.

4.4 Capillary in homogeneous PEG

Similar to section 4.1, the capillary was imaged again. The difference was that the background medium was changed from intralipid to PEG hydrogel [38]. First, intralipid was liquid, difficult to control precision compared to solid phantoms. Crosslinked PEG was solid. Second, the transparency of PEG can be adjusted by the concentration of salt, NaCl. While it is possible to mix intralipid in PEG, intralipid is not soluble in either water or PEG. By contrast, salt is soluble in PEG. Therefore, using salt to control the transparency of PEG is ideal in the sense of maximizing the spatial homogeneity of opacity. Third, in the field of tissue engineering, PEG is a common model. Fourth, the system was switched from 45°-45° to 45°-0° configuration.

The capillary (I.D. = 62μm) was obliquely inserted into a solid crosslinked PEG hydrogel. The capillary was filled with 50μM (diluted in alcohol) indocyanine green (ICG). The reduced scattering coefficient of the PEG was $\mu_s' = 0.7\text{mm}^{-1}$ at 780 nm. Anisotropy was assumed 0.9. Index of refraction was assumed 1.35. With the above parameters, the scattering coefficient was $\mu_s = \frac{\mu_s'}{1-g} = 7/\text{mm}$.

Figure. 21 shows the result. OCT was co-registered to confirm the aFLOT reconstruction by Tikhonov. The co-registration was done by co-registering OCT tomogram and angled reflection measurement[15]. To facilitate the co-registration, fiducial markers were placed

[15] The reflection was acquired by removing the emission filter in aFLOT. See section 3.6.

on the sample surface. Here, a paper ruler was used, which can be seen in Figure. 21F. Generally, the co-registration was successful. The aFLOT reconstruction was therefore reliable.

One can draw more observations from Figure. 21A. First, the resolution degraded when the capillary went deeper. Even though it became worse, the reconstructed capillary maintained high contrast at 1mm. This suggested that aFLOT can further resolve deeper fluorescence signals. An OCT tomogram on the other hand had reached its penetration limit about 1mm. Second, the contrast mechanisms between OCT and aFLOT were different. OCT relied on the scattering of the glass wall of the capillary, and aFLOT relied on fluorescence. It is crucial to design a phantom that can provide contrasts for both systems. Third, the fluorescence was missing around depth 800μm. The instability of Tikhonov reconstruction suggested the erroneous mathematical description of the sensitivity matrix. A better reconstruction scheme to satisfy the hard constraint will be needed in the future work.

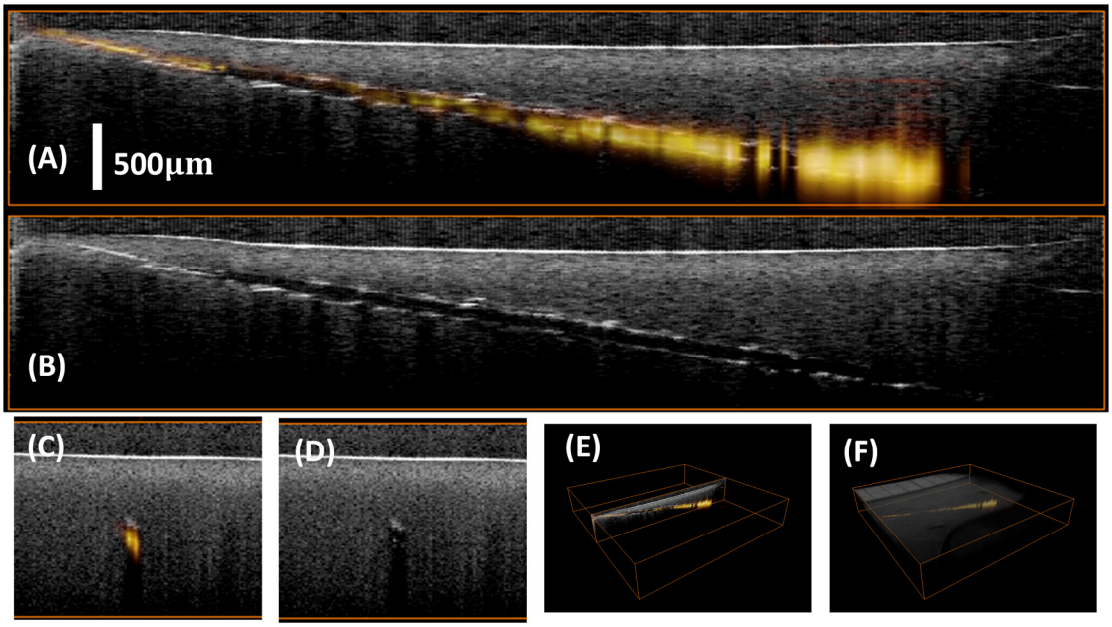

Figure. 21 Co-registration of OCT and line-scan aFLOT of a capillary tube filled with fluorescence dye ICG.

(A) Co-registered OCT/aFLOT YZ cross-section of the phantom. (B) OCT YZ cross-section. (C) Co-registered OCT/aFLOT XZ cross-section. (D) OCT XZ cross-section. (E) The slice where (A) was taken. (F) Perspective view. FOV = $8.7 \times 8.7 \times 1.53\ \text{mm}^3$

4.5 **Capillary in macroporous PEG**

In this thesis, the background medium was assumed homogeneous. The Monte-Carlo simulation didn't adapt the possibly spatially heterogeneous scattering of the background medium. Surprisingly, the reconstruction remained valid to certain degree. In this section, a capillary was again obliquely inserted into a macroporous PEG hydrogel [38]. The capillary profile was reconstructed at least down to 1mm using Tikhonov.

The capillary tube (62 μm in diameter) contained 50 μM (diluted in alcohol) ICG. The reduced scattering coefficient of the macroporous PEG hydrogel $\mu_s' = 1.1\text{mm}^{-1}$ at 780 nm, compared to 0.7mm^{-1} in homogeneous PEG in previous section.

Again, the aFLOT tomogram was co-registered with OCT. Figure. 22A shows XZ and YZ cross-sections. Because of even higher scattering, the penetration depth of OCT was reduced to 600μm. Yet, aFLOT resolved the capillary deep to 1.1mm. Figure. 22C gives a quantitative evaluation of the resolution against depths. The FWHM in x and z of the capillary cross-section and the depth of the capillary center can be derived in each XZ frame. The resulting dots were further least squares fitted. For example, FWHM $= 280, 520\mu\text{m}$ in x and z respectively at 1mm depth.

In this experiment, the capability of aFLOT imaging in heterogeneous macroporous PEG hydrogel was demonstrated. The success of the reconstruction was because the spatial scale of diffused fluorescence was much wider than the heterogeneity of the PEG. Again, while resolution degraded to half-millimeter, the contrast remained high. This suggested that it shall be possible to resolve deeper fluorescence signals.

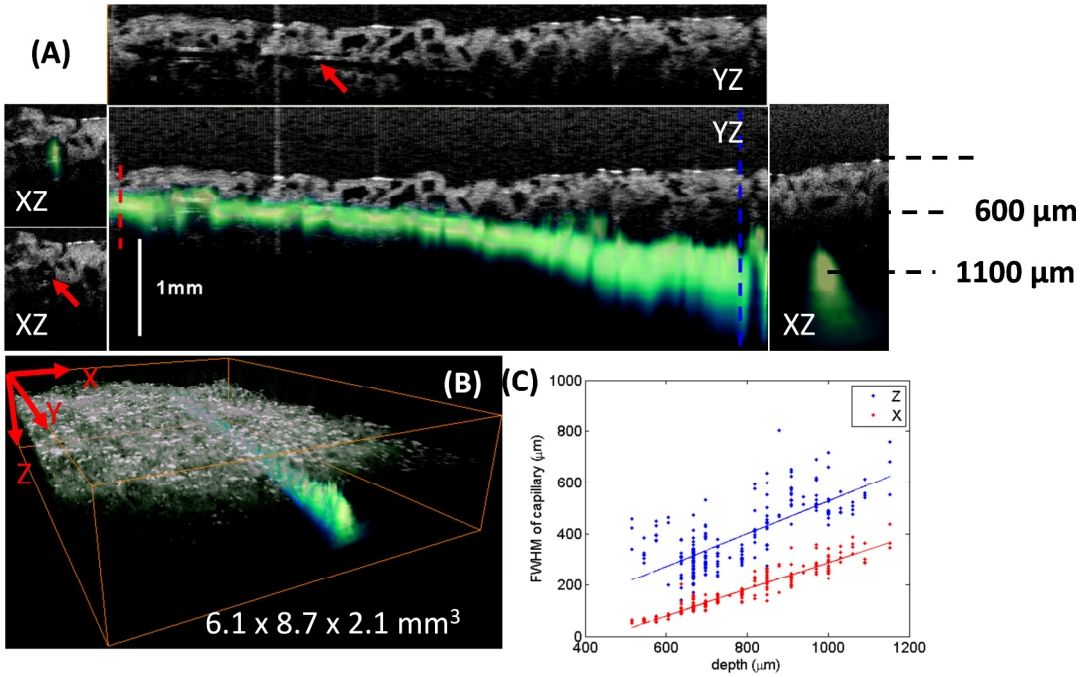

Figure. 22 Imaging capillary tube through heterogeneous PEG.

(A) XZ and YZ cross-sections of OCT/aFLOT tomogram. The red arrow indicates the position of the capillary. (B) Perspective view. (C) FWHM statistics of the capillary in each XZ cross-sections verses depths. (blue ×) is FWHM in z direction. (red •) is FWHM in x direction. Straight lines are linear least square fits.

4.6 **PSF phantoms**

PSF phantoms based on unstructured distributions of sub-resolution particles in a transparent matrix have proven effective for evaluating resolution and its spatial variation in optical coherence tomography (OCT) systems. [39]. Because the size of the particle is smaller than the tested imaging system, the image of the particle approximates the PSF of the imaging system. Imaging PSF phantoms therefore provides an approach to capture and evaluate the evolution of PSF along the depth. For example, plotting the FWHM of each individual PSF against their depth reveals the out of focus aberration of the system.

Following this idea, unstructured fluorescent microspheres (DG06M, Bangs Lab, Inc., IN) encapsulated in PEG hydrogels were fabricated and imaged using 45°-0° aFLOT. The microspheres were of size 8.31 μm. The excitation wavelength peak was at 480nm and the emission wavelength peak was at 520nm. Homogeneous PEG hydrogel was 6mm thick, enough to cover the useful penetration depth. Figure. 23 shows one aFLOT stacking image of the microsphere distribution. Quantitatively, in Figure. 24A, the FWHMs in x,y,z directions (the center panel) and the peak intensity (the right panel) of each PSF were plotted against the depth of the corresponding PSF. At the focus plane, which was at 1500μm, the resolution (FWHM) was 9, 9, 27.6 μm in x,y,z directions respectively. The effect of out of focus aberration was clear in the x direction. About +/- 800μm away from the focus plane, the resolution in x,y,z degraded to 40, 25, 100 μm respectively. The corresponding intensity evolution showed a clear Gaussian distribution. Lastly, for scales above 9mm, the diffraction factor in PSF should be safely neglected. PSFs in transparent medium in mesoscale was mainly influenced by the out of focus aberration only.

Figure. 24 also showed other 3 subplots. The purpose was to compare the effect of scattering and the iris opening on the resolution.

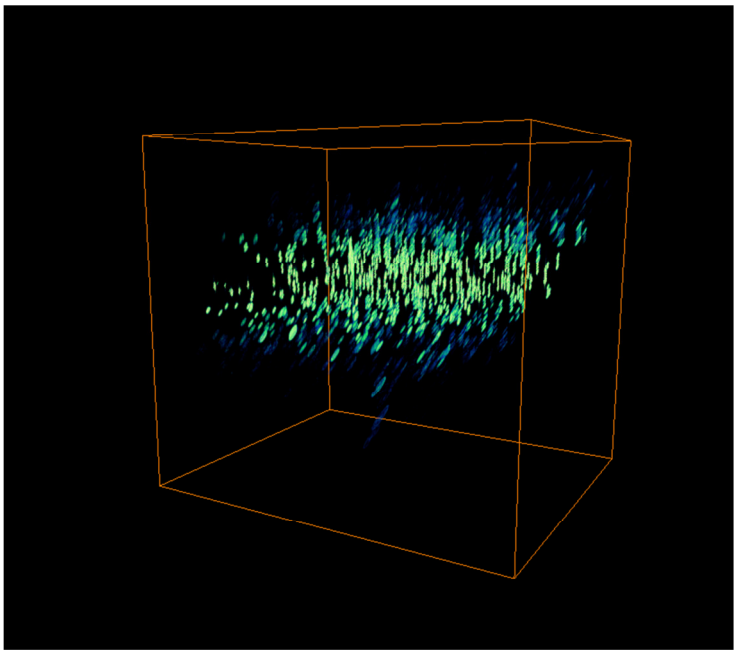

Figure. 23 Unstructured fluorescent microsphere distribution.

$\mathrm{FOV_{xyz}} = \ 2.75 \times 2.29 \times 2.51\ \mathrm{mm^3}$

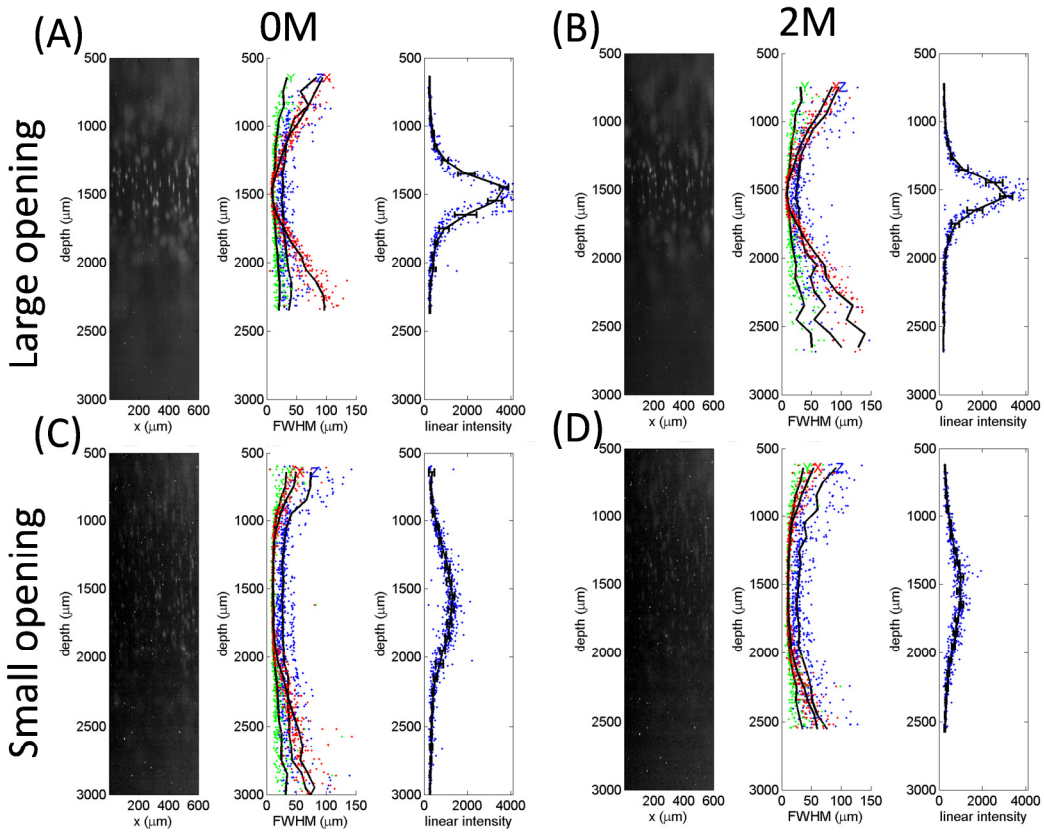

Figure. 24 Resolution (FWHM) and intensity vs. depth, scattering, and iris opening.

Unstructured micro Beads encapsulated in PEG hydrogel. The opacity of PEG was adjusted by the concentration of NaCl. The reduced scattering coefficient was 0.1/mm in (A,C) and 0.3/mm in (B,D). Resolution was modulated by the opening of iris in the detector arm. The iris was largely opened in (A,B) and smally opened in (C,D) Comparing (A,B) or (C,D), higher scattering rendered poorer resolution. Comparing (A,C) or (B,D), small opening of iris decreased

4.6.1 Scattering effect on resolution and intensity

Figure. 24B showed the evaluation of another PSF phantom with higher scattering ($\mu_s' = 0.3/\text{mm}$). The scattering was obtained by increasing the concentration of NaCl (2M) in the PEG hydrogel. Compared with Figure. 24(A,B), the effect of out of focus

aberration became more severe and the intensity of signal dropped. The resolutions were however comparable.

4.6.2 The effect of the iris opening on resolution and intensity

In an attempt to improve resolution, here I present another approach to improve the resolution. Instead of using a mathematical description of PSFs to perform post-reconstruction (section 2.3), I adjusted the opening of the iris in the detection arm. Controlling the opening of the iris appears to be a way to modulate the shape of PSFs. Historically studying the opening of iris was about apodization of light, which is considered as another aberration. It may however be interesting to see the interplay between the aberration of out of focus and apodization (Appendix 2).

Figure. 24(B, D) illustrate the effect of apodization on the resolution and intensity. Resulting from closing the iris, the effect of out of focus aberration was dramatically reduced. This is good because as a tomogram, resolution should be kept constant and small over the whole imaging volume. In Figure. 24B, the resolution in x,y,z at the focus plane degraded to 10.6, 10.6, 28.5 μm (compared to 9, 9, 27.6 μm in Figure. 24A). However, at +/-800 μm away from the focus plane, the resolution in x,y,z was kept to only 40, 20, 40 μm (compared to 40, 25, 100 μm in Figure. 24A).

The price for the reduced out of focus aberration was the reduced signal intensity. However, one future direction may be to combine the high intensity signal acquired using the large opening of iris and the sharp feature acquired using the small opening of the iris.

4.7 Summary

Table 1 summarizes the key parameters of the experiments described in chapter.

Table 1 Summary of characterization of aFLOT. Anisotropy was assumed 0.9. Index of refraction was 1.35.

section	4.1	4.2	4.3	4.4	4.5	4.6
configuration	45°-45°	45°-45°	45°-0°	45°-0°	45°-0°	45°-0°
date of experiment	2010.11.04	2011.09.24	2012.02.13	2012.01.17	2012.01.17	2012.10.19
μ_s'(/mm) at ex	1.1	0-0.9	0.1	0.7	1.1	0.1-0.2
ex (nm)	532	532	780	780	780	473
em filter (nm)	605±15	605±15	845±27.5	845±27.5	845±27.5	517±10
object	capillary	capillary	layered PEG	capillary	capillary	microsphere
background	1% IL	0-1.5% IL	PEG	salted PEG	salted PEG	PEG
fluorophore	Rd6G 1 μM	Rd6G	ICG 14.75μM	ICG 50 μM	ICG 50 μM	DG06M
size of feature (μm)	110	400	3000	62	62	8.31
depth of feature (mm)	1.2	0-2.4	9	0-1	0.5-1.1	0-6
reconstructed size of feature (μm)	178.5	>400	3000	60-400 in z	60-250 in x 210-600 in z	9 in x y 27.6 in z
reconstructed depth of feature (mm)	1.14	0-2.4	9	0-1	0.5-1.1	0-2.5

In section 4.1, I showed that a comparable phantom that was imaged previously using FLOT was imaged again using aFLOT. Because of the oblique illumination, the depth selectivity was improved. In section 4.2, the detectability of the fluorescing capillary

cross-section against depths and scattering was systematically studied. The high dynamic range of fluorescence intensity would necessitate the high dynamic range of measurements. It is critical not to saturation EM-CCD for quality reconstruction. High scattering samples fall into this situation. On the other hand, if samples are low scattering, I showed that penetration depth can be as deep as 9mm in section 4.3. Besides, out of focus aberration would become severe in such deep penetration. In sections 4.4 and 4.5, I showed that in high scattering materials, 1mm penetration was routinely achieved. Such penetration was a good match to OCT's, supporting the idea to combine these two modalities. In section 4.6, I imaged the PSF phantom, an emerging standard to characterize 3D imaging systems. The PSFs of aFLOT were strongly influenced by out of focus aberration. Yet, one may be able to modulate this aberration, thereby improving the image quality in the future.

To sum, current implementation of aFLOT was able to perform 1mm penetration and up to 9-400μm resolution in either low or high scattering medium ($\mu_s' = 0.1 - 1.1/\mathrm{mm}$).

5 Application of aFLOT: Tissue Engineering

Regenerative medicine has emerged as an important discipline which aims at introducing living cells or functioning tissues to repair injury or replace damaged tissues or organs which lose functions. Optimization of regenerative medicine strategies includes the design of biomaterials, cell-seeding methods, cell-biomaterial interactions, and molecular signaling within the engineered tissue. One challenge is to non-destructively observe and quantify the distribution and migration of seeded cells throughout the bulk scaffold. The development of tissue engineered products is limited by the lack of laboratory imaging techniques which are capable of non-destructive imaging of the three-dimensional morphology as well as the cell response of a tissue engineering scaffold. The current method for quantifying 3D cell distribution involves fluorescent confocal microscopy imaging of cryo-sectioned scaffolds followed by digital 3D image recompiling [40]. Although robust, this approach is destructive and time-consuming, and thereby may become a concern in longitudinal inspection of massive amount of samples.

In this chapter, aFLOT was used to resolve the distribution of human mesenchymal stem cells (hMSCs) embedded in or seeded on hydrogels.

5.1 hMSCs embedded in PEG

hMSC embedded in PEG hydrogel is a common construct of the engineered-tissue scaffold for bone regeneration. hMSCs are encapsulated in PEG during the crosslinking

of PEG[16]. hMSCs are a promising cell source for bone tissue engineering as they can be isolated from bone marrow and readily differentiated into osteoblasts [41]. In this experiment, a bi-layer model was fabricated. The bottom layer was pure PEG. The top layer was MSC-embedded PEG (cell density = 10^4 - 10^5 /mL). The thickness of the top layer was 0.5, 1, 2, and 3 mm (4 samples were prepared).

The fabrication of PEG hydrogel was mixed equal amount of PEGDA[17], 45mM APS[18], and 45mM TEMED[19] sequentially. The cross-linked PEG was homogeneous and almost transparent in visible wavelengths. For Monte-Carlo simulation and Tikhonov reconstruction, the measured reduced scattering coefficient was 0.1/mm. Anisotropy g = 0.9, refractive index = 1.33, and absorption coefficient of 0.01 mm^{-1} of PEG were assumed.

hMSCs were labeled with LIVE/DEAD assay (invitrogen), but only the LIVE part was imaged. Polyanionic dye calcein (the LIVE assay), retained within live cells, produces an intense uniform green fluorescence (ex/em 485/530 nm). In this experiment, the excitation was at 473nm and the emission filter was at $517 \pm 10\mathrm{nm}$.

---

[16] Crosslink is a reaction in which one polymer links to one another. Crosslink results in the change of the physical properties of the polymer. The crosslinking of PEG hydrogel changes the PEG from liquid to solid.

[17] poly(ethylene glycol) diacrylate

[18] ammonium persulfate

[19] N,N,N',N'-tetramethylethylenediamine

Figure. 25 shows the YZ projections and perspectives of the cell distribution. From the projections (A1-D1) and the histogram (F), the thicknesses of the top cell-contained layers were clearly distinguished. The estimated cell distribution depths were distinct and consistent with the nominal thickness of each sample during fabrication. From the histogram, the cut-offs were at 0.7mm, 1mm, 1.8mm, and 2.9mm, compared to the nominal thickness 0.5mm, 1mm, 2mm, and 3mm. Besides the clear cut-offs, the fluorescence intensity of the 2mm and 3mm samples gradually dropped toward deeper region. This should be because of the out of focus aberration. Lastly, it was consistently observed that all the cell-distributions patterns peaked at the bottom surface. This may be attributed to the condensation of cells or interface reflection.

This experiment demonstrates that aFLOT can resolve the depth-dependent cell distribution of in the weakly scattering PEG hydrogel. [5]

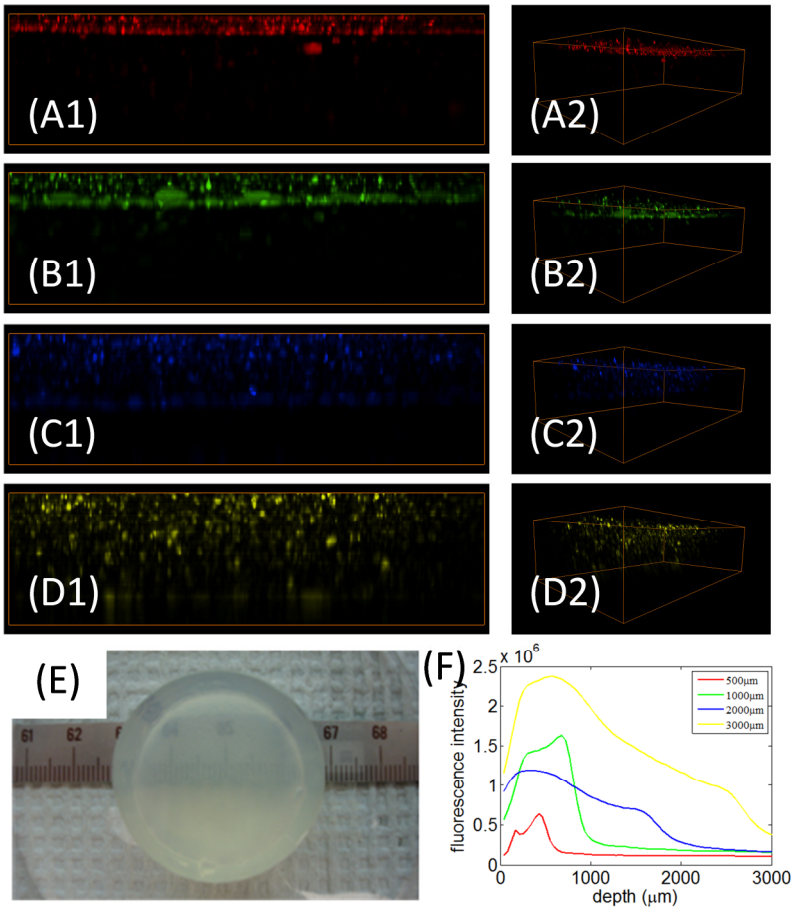

Figure. 25 3D aFLOT imaging of PEG hydrogels with stem cells embedded at top layers.

Cell layer thickness was nominally 0.5mm(A), 1mm(B), 2mm(C), and 3mm(D). (A1-D1) YZ projection. (A2-D2) Perspective. FOV = $10.6 \times 6.5 \times 2.9\text{mm}^3$. (E) Photo of a sample. Transparency indicates low scattering. (F) Histogram of the depth of cells.

Cell distributions were obtained by Tikhonov reconstruction.

5.2 hMSCs seeded on macroporous (heterogeneous) PEG

The PEG is hydrophilic. Small ions such as Na^+ and Cl^- can diffuse out from the PEG.

Using this property, Salt, or NaCl, has been used as the porogen, to create pores inside

PEG. Because of the pores, MSCs can be seeded after PEG is cross-linked. (In the previous model, MSCs was mixed with PEG during the cross-linking.) Macroporous PEG maintains mechanical sustainability for MSCs to grow within. More, it facilitates the behavior of MSCs, such as migration. (In the model in the previous section where MSCs were encapsulated in PEG, MSCs may mainly perform proliferation, but not migration.)

Using salt as the porogen changed the transparency of PEG. The opacity of PEG depended on the concentration of NaCl. To create pores inside PEG, during cross-linking, saturated salt solution was used to prevent NaCl crystal from dissolving. From Table 1, the reduced scattering coefficient of macroporous PEG was 1.1/mm. Therefore, 1.1/mm should be the maximal reduced scattering coefficient that salted PEG can be.

NaCl was however lethal to MSCs. Therefore, once the PEG was cross-linked, it was immersed in a tank of water for 3 days for NaCl to dissolve and diffuse out from the PEG, leaving only pores inside. After NaCl had been sufficiently leached, MSCs were seeded. In this experiment, 180K cells were seeded on the macroporous PEG.

The fluorescence of hMSCs was from quantum dots whose emission was peaked at 665nm. (QD665, Ocean Nano Tech.) The excitation was at 473nm. The quantum dot had exclusively high quantum yield. However, there was no particular reason to switch from the LIVE/DEAD assay to QD665.

Again, the cell distribution was of interest. Figure. 28 (A,B) compares the stacking representation and Tikhonov reconstruction. Tikhonov reconstruction de-convoluted the

PSFs of the aFLOT, giving better quality of the image of the cells. (C) is co-registration of the structural macroporous PEG. In addition, for comparison, images acquired by white light and fluorescence microscope are shown in (D) and (E). The image acquired by two photon microscope is shown at (F).

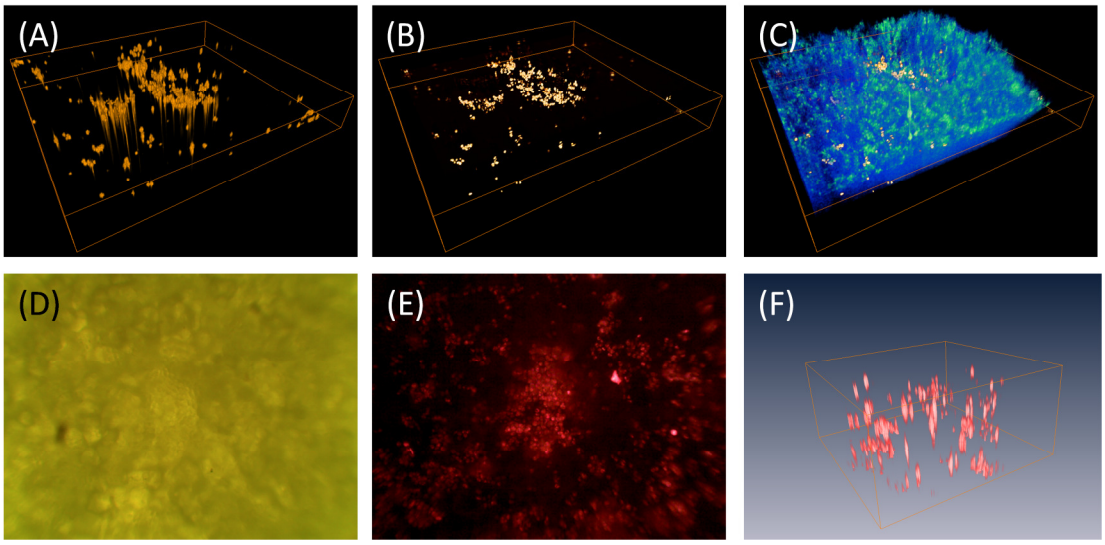

Figure. 26 hMSCs on the macroporous PEG.

(A) Stacking representation. PSF convoluted image of cells had long tails in z direction. (B) Tikhonov reconstruction. De-convolution of PSF made the image of cells tighter. (C) Co-registration with the structural image of macroporous PEG. FOV in (A-C) was $2.1 \times 2.3 \times 0.3\text{mm}^3$. (D) Image of the sample under full field white light illumination. (E) Image of the sample under full field blue light illumination. Red fluorescence was collected. (F) Two photon image of the sample. FOV=$0.8 \times 0.8 \times 0.389\text{mm}^3$

5.3 hMSCs sandwiched between two macroporous (heterogeneous) PEGs

While cells may take advantage of the pores to migration or infiltrate into PEG, to demonstrate that aFLOT can see through the PEG, a thin 0.2mm layer of another

macroporous PEG was piled onto the cell-seeded macroporous PEG. In other words, MSCs were sandwiched between two macroporous PEGs. During the handling, few hMSCs were still on the top surface of the PEG. However, major portion of MSCs were sandwiched.

It is worthwhile to look at one example of the raw measurement image. In Figure. 27, besides the central cloud of fluorescence representing the sandwiched cell clusters, two other individual cells labeled as c1 and c2 are of interest. C1 and c2 represents one single cell that was on the surface and in the matrix (0.2mm below the surface), respectively. During the scanning, the image of c1 appeared brightly and sharply while the image of c2 never did so even if adjusting the focal plane. The comparable depths ruled out the effect of the out of focus aberration. The nature that c2 always appeared dim and blur concluded that c2 was the fluorescence diffused by the scattering of the macroporous PEG.

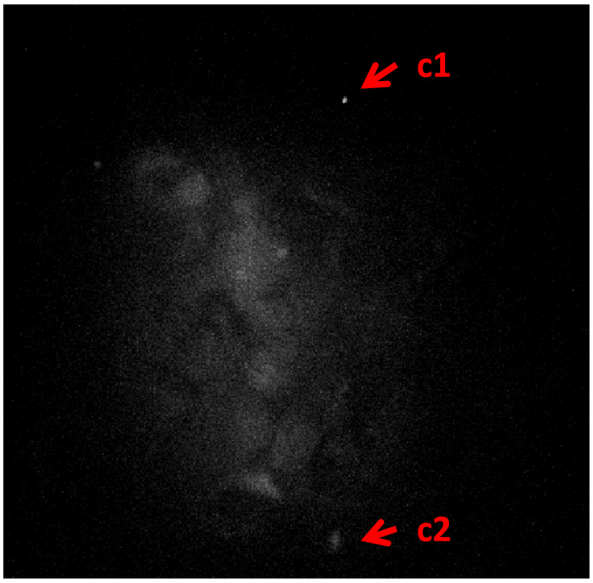

Figure. 27 Diffused fluorescence.

C1 was fluorescence emitted from cell#1 on the matrix surface. It was sharp and bright. C2 was from cell #2 in the matrix. Fluorescence was diffused because of the scattering of the matrix. It was dim and blur.

Figure. 28 shows the result. From both the stacking (A) and the Tikhonov reconstruction (B), the resolved cells appeared larger due to scattering, which diffused the fluorescence. The image quality of Tikhonov reconstruction was still better than that of stacking.

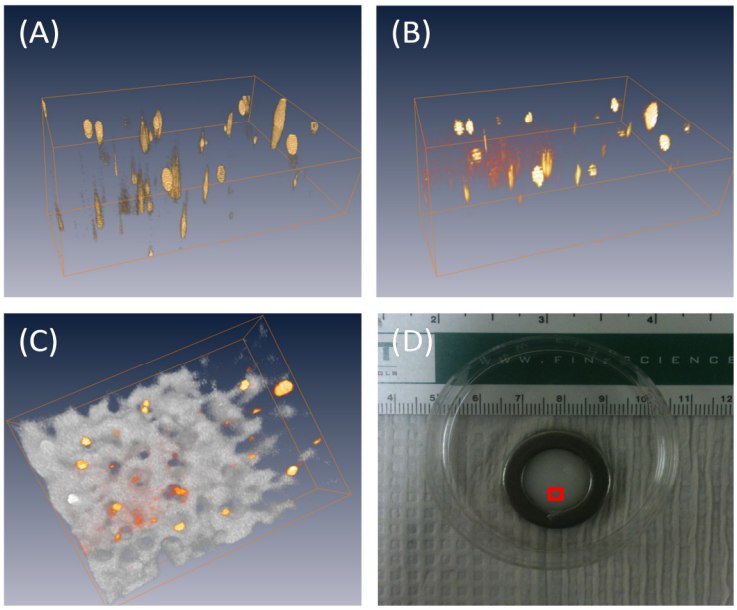

Figure. 28 hMSCs sandwiched between two macroporous PEGs.

(A) Stacking representation. (B) Tikhonov reconstruction. (C) Co-registration with the structural image of macroporous PEG. FOV in (A-C) was $2.3 \times 2.9 \times 0.8\text{mm}^3$. (D) Photo of the sample.

5.4 hMSCs in alginate beads

One present difficulty in tissue engineering is the inability to successfully culture a large, clinically relevant 3D construct in vitro. Often, a scaffold is constructed in its final shape and seeded with cells. The largeness of the scaffold however limits the later homogeneous cell proliferation and matrix deposition. Even when cells are cultured in the bioreactor, central oxygen concentration in the construct is low and therefore cells cannot remain viable [42].

Alginate bead is the small-scale building block, each of which can be cultured individually before being assembled into the large final construct. This will allow for the

in vitro development of tissue engineering constructs on size scales not easily possible with aforementioned methods [41].

A model like alginate bead is suitable for aFLOT imaging, as the size of cells is relevant to the resolution of aFLOT (10-100 μm) and the size of the bead is relevant to the penetration of aFLOT (2-4 mm). The ability that aFLOT can monitor in situ the cell proliferation in the construct provides a powerful tool for optimizing the tissue engineering strategy.

In this section, the experiment involved the culture of hMSCs in alginate beads in the tubular perfusion bioreactor. After culturing, the bead was labeled with the LIVE assay and imaged under aFLOT. The hMSCs were encapsulated in alginate, a natural biomaterial derived from algae that is frequently used in bone tissue engineering [43, 44]. First, hMSCs were mixed in the alginate solution. Second, a droplet of such alginate cell solution was ejected from the syringe needle tip into the calcium chloride solution. The calcium ionically crosslinks and therefore gels the alginate solution. The culture medium was pumped and perfused by the bioreactor, which has been shown to support the growth and osteoblastic differentiation of hMSCs [1].

The uncultured bead at day 0 and the bead cultured bead for 21 days were labeled with the LIVE assay. Both beads were imaged under aFLOT afterwards.

Figure. 29 shows the summary, comparing the hMSC distributions in alginate beads at day 0 and day 21. At day 0, hMSCs were homogeneously distributed (XYc_0). During fabrication, hMSCs were evenly mixed in alginate solution before the cross-linking.

Therefore, a homogeneous cell distribution can be expected. After culturing for 21 days in the perfusion bioreactor, the constantly refreshing medium kept cells at the peripheral of the bead viable. By contrast, cells in the center of the bead underwent hypoxia. Therefore, after the labeling of the LIVE assay, viable cells can only be seen at the peripheral area (XYc_{21}). Besides, during the 21 day culturing, calcification produced by the cells turned the alginate bead from transparent to semi-opaque (PB_0 vs. PB_{21}). The semi-opacity didn't prevent aFLOT from seeing through the other side. That a full cell distribution around the bead was captured indicates that the illumination fully penetrated the bead. No fluorescence emitted from the center of the bead was because of no viable cells, but not because the opacity blocked the light. However, more solid evidence can be established by using the DEAD assay. The DEAD assay (ex/em 530/645nm) is rejected by the intact membrane of viable cells and can only enter the nucleus of dead cells. In our case, red fluorescence should appear in the center of the day 21 bead.

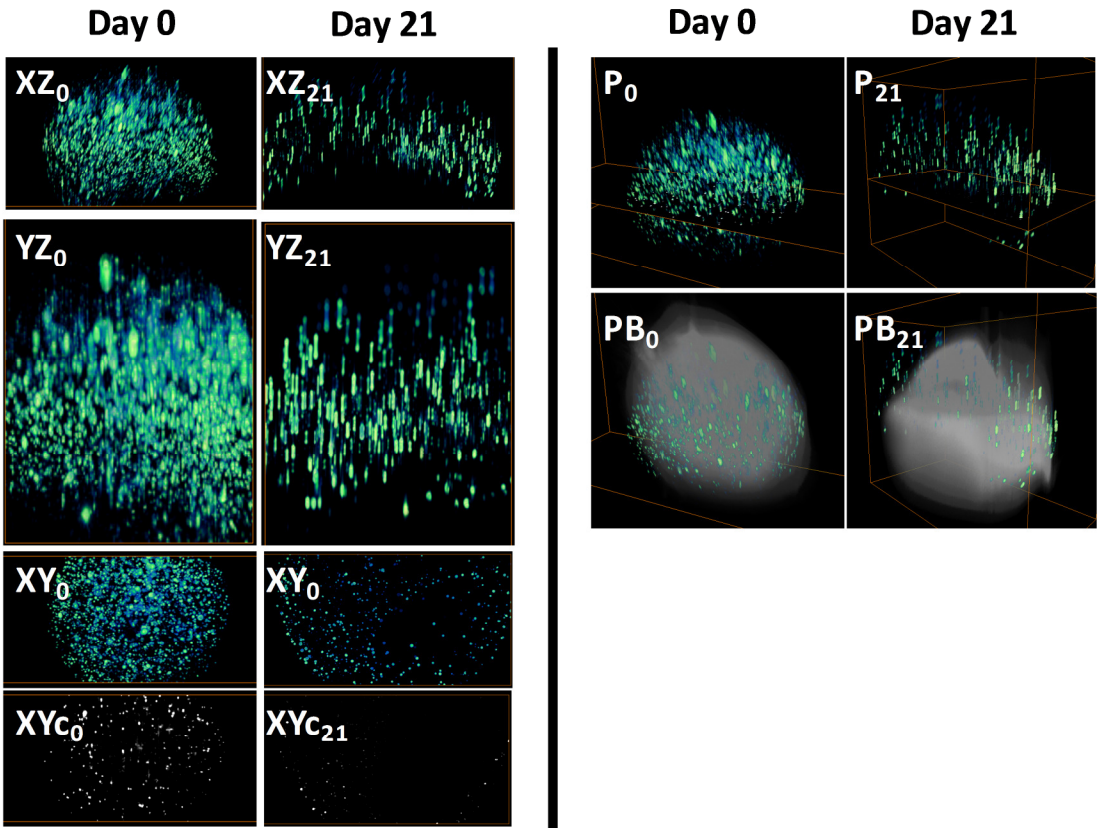

Figure. 29 Alginate beads at day 0 and day 21

XZ, YZ, XY are projections of the stacking representation. XYc is one cross-section in the center of the bead. P is perspective. The position of the cross-section was also shown. PB is the perspective with bead profile co-registered.

FOV of the day 0 bead was $4.4 \times 1.6 \times 2.56\text{mm}^3$. FOV of the day 21 bead was $4.6 \times 2.3 \times 3.7\text{mm}^3$.

Figure. 30 is a direct comparison between full field fluorescence microscopy and aFLOT. The former is non-destructive, almost real time, and gives planar or projected information of cell distribution. The latter is non-destructive too. The tomogram can be acquired and rendered in 3 minutes, giving 3D information.

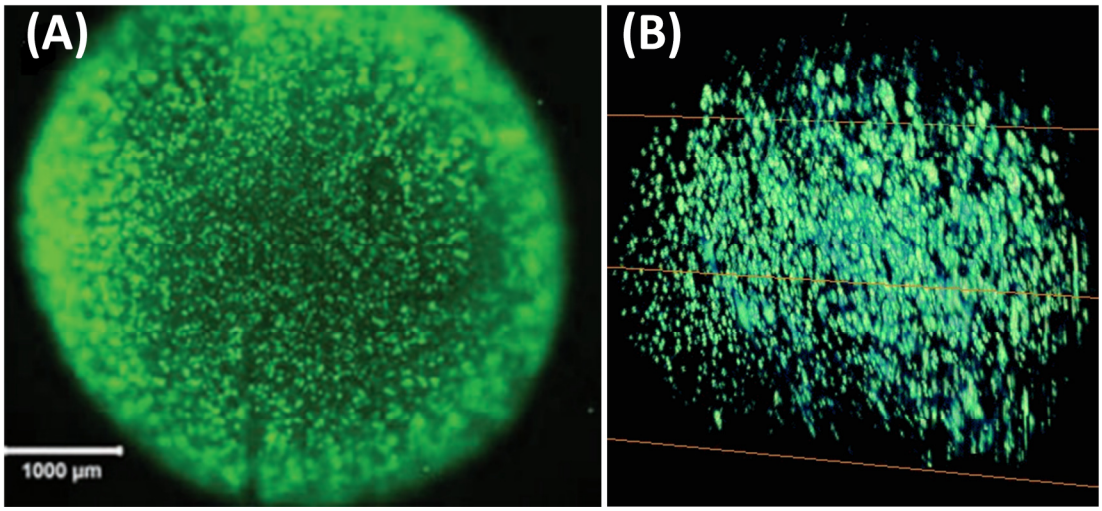

Figure. 30 compare the image by fluorescence microscopy (A) and aFLOT (B). (A) from [1] (B) the same day 0 bead in Figure. 29. FOV=$4.4 \times 1.6 \times 2.56\text{mm}^3$

5.5 **Summary**

The results in chapter show that aFLOT is a promising imaging technique to resolve *in situ* and quantify the information of depth-resolved fluorophore distributions in several common engineered tissue constructs. As investigating cell-scaffold interactions is a routine task in tissue engineering studies, yet cryo-sectioning and histology are still the laborious tools, the advent of aFLOT would provide another powerful tool for tissue engineering. Several key advantages are repeated. First, aFLOT performs non-destructive imaging. The merit of *in situ* imaging is preserved. Second, aFLOT performs 3D imaging. A global full picture of the sample reveals cell-cell or cell-scaffold interactions, which is not the emphasis of either microscopy or macroscopy. Third, the non-destructive imaging nature usually guarantees the high speed imaging. As a comparison, acquiring

histological results at 4 to 5 discrete time points (for example, at day 1, 7, 14, 21, 28) is standard. With aFLOT, a denser sampling can be achieved. The convenience also saves one from additional histological staining.

6 Conclusion

6.1 A unified system

A new system capable of non-invasive, three-dimensional fluorescence imaging is described. The system, termed angled fluorescence laminar optical tomography (aFLOT), fills the gap between microscopy and macroscopy, offering a balance of penetration and resolution designed to provide quality images of biological structures whose sizes and locations fall somewhere between the typical ranges of microscopy and macroscopy.

aFLOT non-invasively resolved three-dimensional images of the distribution of fluorophore-labeled, live stem cells growing in either low or high scattering environments, facilitating research in regenerative medicine.

Simulations and experiments demonstrated that introducing the angular degree of freedom improved the depth selectivity. Oblique illumination is not itself a novel idea. For example, in the regime of microscopy, both SPIM and CTM take advantage of oblique illumination. While successful, the main limitations of these techniques are that the sample has to be small and transparent. Small size is required because of the configuration of the instrument. Transparency is required because they fail to pass the optical properties of opaque tissues to mathematic system required for post-processing. As a result, a clearer feature cannot be resolved for tissues with high scattering coefficients.

When an opaque sample is of interest, aFLOT overcomes the limitations by borrowing the knowledge from FLOT to recover the underlying fluorophore distribution. The image quality depends not only on the instrument itself, but also on the imaged subject. Therefore, transferring additional information about the optical properties of the subject enables us to further improve the image quality. While the advantage of oblique illumination diminishes with increasing scattering, the Monte-Carlo simulation showed that aFLOT still outperformed FLOT.

In a sense, aFLOT unifies several optical systems. First, when transparent samples are imaged, aFLOT is similar to mesoscopic SPIM. Second, when opaque samples are imaged, aFLOT is similar to FLOT. Third, by removing the emission filter, the reflection mode is the same as LOT. Fourth, oblique illumination as in the reflectometry enables one to derive the reduced scattering coefficient from measured light distributions.

6.2 **Contribution**

1. The thesis is the first study that introduces the angular degree of freedom into FLOT technology. Oblique illumination improved both the resolution and depth selectivity.
2. Oblique illumination also enables the stacking representation. Avoiding the reconstruction simplified the aFLOT data processing.
3. The thesis pointed out that there were two mechanisms of depth selectivity. When photons remain to travel ballistically (MFP<1), one obtains the depth selectivity through oblique illumination/detection. On the other hand, when photons are

multiple scattered (MFP>1), one obtains the depth selectivity through the scattering. aFLOT can use both mechanisms to enhance the depth selectivity.

6.3 **Future work**

In chapter 2, a mesh-based reconstruction scheme was discussed to ease the intensive computation of the reconstruction process. In the special low scattering application, the stacking is one approach to avoid the reconstruction. To further improve the resolution in stacking, an idea of modulating PSFs of aFLOT through changing the size of iris was mentioned in section 2.3.5, 3.5, and 4.3. The idea was primitively elaborated in appendix 2.

In section 4.2, the high dynamic range in scattered fluorescence intensities necessitates the implementation of a high dynamic range detection. As a result, one can resolve deeper fluorophores, further increasing penetration.

In section 4.4, random erroneous Tikhonov reconstruction that led to missing fluorescence was seen. In the present approach to satisfy the hard constraint by simply replacing negative values with zeros, the analytical algorithm takes an unreasonably long time to search the legitimate solution. This demanded a better reconstruction process.

Appendix

1 Interface of aFLOT data acquisition

Several applications are used and synchronized. CamWare is the application interfacing EM-CCD. ESP 300 is the motor controller that controls Newport's actuator CMA-25CCCL to translate the sample. ESP-Util is the application interfacing ESP 300. Sikuli[20] is an application that executes a user-defined script so that synchronization between ESP-Util and CamWare is achieved.

CamWare. User specifies the electronic gain, exposure time, and the number of frames being recorded here. The total acquisition time can therefore be derived by multiplying the number of frame with exposure time per frame. For example, 500 frames and 0.2s per frame render 100s.

ESP-Util. This application supports scripting to control ESP300. aFLOT only need 3 commands: 2VA0.05, 2PA0, and 2PA6. The first number 2 indicates it is axis 2 that is under control. 2VA0.05 sets axis 2's scanning speed 0.05mm/s. 2PA0 moves axis 2 to absolute position 0mm. 2PA6 moves axis 2 to absolute position 6mm. Note however that the absolute position is not in the memory once ESP300 is turned off. ESP300 always regards the current physical position as 0mm when turning on. Therefore, before turning off ESP300, it is always a good practice to send 2PA0. 6mm was a typical scanning

[20] http://sikuli.org/

distance. Using the above example, 100s are the total acquisition time and the speed of scanning is 0.05mm/s, the stage would accordingly move 5mm<6mm. The 1mm buffer distance is required because the actuator starts moving before EM-CCD acquires images and stops moving after EM-CCD finishes acquisition.

2 Achieving tomographic imaging through out of focus aberration and apodization

2.1 Motivation

During the development of aFLOT instrumentation, both illumination and detection arm are implemented using 4f configuration. One main advantage of 4f configuration is its insensitivity to path length between 2 lenses as long as the detector (EM-CCD) or light source and specimen are placed in the focal plane of the corresponding lens. This simplifies the design of optics. Besides, magnification is simply the focal length ratio between two lenses. Lastly, one gains the access to manipulate spatial frequencies of light that travels between the 2 lenses.

To achieve tomographic imaging, one related parameter should be depth of field (DoF), which is defined as a region within which every feature is with comparable sharpness. If short DoF is used, the tomography may severely suffer from out-of-focus aberration. To alleviate the effect, quoted from Jeff Conrad's concise statement, "*Controlling DoF ultimately is quite simple—the aperture stop controls the size of the blur spot, and the focus determines the position of the DoF,*" one can simply reduce the aperture size to increase DoF. Therefore, by inserting one iris in the middle of the 4f configuration, we may study how to manipulate the aperture size to take fully advantage of long DoF, achieving a tomography in which everywhere is with comparable sharpness. It is worthwhile to note that the iris inserted in the 4f configuration can be thought of as a

spatial light modulator which controls how high frequency the sample's angular spectrum can pass through.

During implementation, I added an iris in between 2 face-to-face AC-254-60-B (Thorlabs). Because the 2 lenses are face-to-face, the 4f configuration is symmetric. The effect of different DoF was strong: What is focused remains focused. What is out-of-focused can become in focus as well. Features that are far from focus plane suffer from out-of-focus effect most, but the rate of getting in focus is also the fastest when reducing aperture.

This appendix explores see the interplay between the out-of-focus aberration and the apodization through changing the aperture size, but only the coherent illumination was investigated.

2.2 **Physics understanding**

The more open the iris is, the larger the aperture is, the more diverse directions of light the lens can capture, the richer the sample object's angular spectrum is perceived. As a result, the object in focus plane can be perceived with better resolution. What's compromised is the object other than in focus plane now becomes blurring. A vivid example is to change the objectives in a common microscope. High NA objective resolves finer feature, but the working distance is shorter than low NA objective. What causes blurring is counter-intuitively by overwhelmed information in angular spectrum. The signal from the focus plane is so strong that it overwhelms signals from other planes. Signals are perceived, but not accessible.

On the other hand, when iris closes, the aperture rejects light from large angle. This is especially profound for near field. The same object, when placed at near field, requires light from larger angle than when placed at far field. Since light from near field is rejected, one can better perceive object in the far field. Note however that the lens still independently determines where to focus. What is changed is DoF.

As a result, if continuously reducing the size of aperture, one can see that objects other than in focus plane gradually become in focus. The rate of becoming in focus is faster for object farther away from focus plane, as object in focus plane barely changes.

By playing the trick of changing aperture, one may additionally use the rate of changing PSF size to determine the distance of signal from the focus plane, therefore achieving tomographic imaging.

2.3 **Mathematics formulation**

This section attempts to formulate the mathematic foundation to recover depth resolved tomogram from measurements. The measurements here are a series of 2D images, each of which is acquired using different opening of aperture. More, each such image by nature is a lumped-sum of information at different depths. The key idea is that the weighting among different depths is able to be manipulated through different opening of aperture. As a result, one can manipulate measurements by matrix inversion to bring back depth-resolved tomogram.

The mathematics here describes the coherent, mono-chromatic wavelength case. I start from Huygens-Fresnel principle. Fresnel approximation will be assumed immediately. Then we investigate the field that propagates d_o, encounter a thin symmetric lens with focal length f and finite aperture ϵ, and propagates another d_i to reach the detector.

Based on Huygens-Fresnel principle, if propagating in free space, two fields separated by distance z are related as

*Equ.*15 $$U(x_1, y_1) = \frac{1}{j\lambda} \iint dx_0 dy_0 \, U(x_0, y_0) \frac{e^{jkr_{01}}}{r_{01}} cos(\theta)$$

Where λ is the wavelength of light, θ is the angle between the optical axis direction $\vec{n}$ and $\overrightarrow{r_{01}}$ so that $cos(\theta) = \frac{z}{r_{01}}$, and $r_{01} = \sqrt{z^2 + (x_0 - x_1)^2 + (y_0 - y_1)^2}$. $U(x, y)$ is the linear polarized complex field. To relate to physical electrical or magnetic field, use $EM(x, y, t) = Re[U(x, y)e^{-jwt}]$ where EM fields satisfy $\nabla^2 EM(x, y, t) - \frac{1}{c^2}\frac{\partial^2}{\partial^2 t} EM(x, y, t)$=0.

Under Fresnel approximation, $r_{01} \approx z + \frac{1}{2z}[(x_0 - x_1)^2 + (y_0 - y_1)^2] \approx z$. Equ . 15 becomes

*Equ.*16 $$U(x_1, y_1) = \frac{e^{jkz}}{j\lambda z} \iint dx_0 dy_0 U(x_0, y_0) e^{j\frac{k}{2z}[(x_0 - x_1)^2 + (y_0 - y_1)^2]}$$

This integral is space-invariant. As an application, without loss of generality, consider a single plane object $U_o(x, y; z = 0)$. After propagating d_o, field U_l is

*Equ.*17 $$\boldsymbol{U_l(\xi,\eta) = \frac{e^{jkd_o}}{j\lambda d_o}\iint dxdyU_o(x,y)e^{j\frac{k}{2d_o}[(x-\xi)^2+(y-\eta)^2]}}$$

A thin symmetrical finite lens adds a factor $p(\xi,\eta)e^{-j\frac{k}{2f}[\xi^2+\eta^2]}$ to U_l, where $p(\xi,\eta)$ is the pupil function that controls the aperture and $e^{-j\frac{k}{2f}[\xi^2+\eta^2]}$ is because of the lens. Again, by propagating another d_i to reach the image plane, the final field $U_i(u,v;z=d_o+d_i)$ on the detector is

*Equ.*18 $$U_i(u,v) = \frac{e^{jkd_i}}{j\lambda d_i}\iint d\xi d\eta U_l(\xi,\eta)e^{-j\frac{k}{2f}[\xi^2+\eta^2]}e^{j\frac{k}{2d_i}[(u-\xi)^2+(v-\eta)^2]}$$

To focus on the relation between initial field U_o and final field U_i, substitute Equ.(17) into Equ.(18). After simplification,

*Equ.*19
$$\begin{cases} U_i(u,v) = K(d_i;u,v)\iint_{x,y} dxdyU_o(x,y)K(d_o;x,y)\,P(x,y;u,v;d_o,d_i;\epsilon) \\ P(x,y;u,v;d_o,d_i;\epsilon) = \frac{-1}{d_o d_i}F\left\{p_\epsilon(\lambda\xi,\lambda\eta)e^{j\pi\Delta\lambda(\xi^2+\eta^2)}\right\}\left(\frac{x}{d_o}+\frac{u}{d_i},\frac{y}{d_o}+\frac{v}{d_i}\right) \\ K(d;x,y) = e^{jkd+j\frac{k}{2d}[x^2+y^2]} \\ \boldsymbol{\Delta = \frac{1}{d_o}+\frac{1}{d_i}-\frac{1}{f}} \end{cases}$$

All above has been well developed. From now on, I attempt to elaborate more on P. I call $P(x,y;u,v;d_o,d_i;\epsilon)$ pupil modulation function. $F\{\cdot\}$ is 2D Fourier transform, transforming argument (ξ,η) to spatial frequency $(s_\xi,s_\eta) = (\frac{x}{d_o}+\frac{u}{d_i},\frac{y}{d_o}+\frac{v}{d_i})$. Despite P depends on many parameters, it appears that P should weakly depend on $(x,y;u,v)$ if in far field. This is because if in far field, both d_o and d_i are sufficiently large. Therefore,

$\left(\frac{x}{d_o}+\frac{u}{d_i},\frac{y}{d_o}+\frac{v}{d_i}\right)\approx(0,0)$. If so, it is reasonable to approximate $P(x,y;u,v;d_o,d_i;\epsilon)\approx P(d_o,d_i;\epsilon)$. As a result,

$$U_i(u,v)=K(d_i;u,v)\iint_{x,y}dxdyU_o(x,y)K(d_o;x,y)\,P(d_o,d_i;\epsilon)$$

This expression indicates what is seen using aperture ϵ if a single plane object U_o is placed. Now we generalize this expression by adding object at different depths. This can be done by replacing $U_o(x,y)K(d_o;x,y)$ with $\sum_{n=1}^{N}U_n(x,y)K(d_n;x,y)$. U_n is the field representing the slice of object at depth d_n. In order to resolve individual $U_n(x,y)K(d_n;x,y)$, it looks feasible by varying the aperture size ϵ because P depends on d_o. Assuming M different apertures are used, U_{im} is the image under aperture ϵ_m, then

$$U_{im}(u,v)=K(d_i;u,v)\iint_{x,y}dxdy\sum_{n=1}^{N}P(d_n,d_i;\epsilon_m)\,U_n(x,y)K(d_n;x,y)$$

Or

$$[U_{im}(u,v)]_{M\times1}=K(d_i;u,v)\iint_{x,y}dxdy\,[P]_{M\times N}\,[U_n(x,y)K(d_n;x,y)]_{N\times1}$$

Matrix inversion brings back$U_n(x,y)K(d_n;x,y)$

2.4 Examples

2.4.1 Verify the prediction of geometric optics.

If the lens is infinitely large and no aperture, $p(x,y)=1$. Besides, the position of object and image follows $\Delta=\frac{1}{d_o}+\frac{1}{d_i}-\frac{1}{f}=0$, then $P=\frac{-1}{d_o d_i}\delta\left(\frac{x}{d_o}+\frac{u}{d_i},\frac{y}{d_o}+\frac{v}{d_i}\right)$.

$$U_i(u,v)=K(d_i;u,v)\iint_{x,y}dxdyU_o(x,y)K(d_o;x,y)\,P$$
$$=K(d_i;u,v)K\left(d_o;-\frac{d_o}{d_i}u,-\frac{d_o}{d_i}v\right)\times-\frac{d_o}{d_i}U_o(-\frac{d_o}{d_i}u,-\frac{d_o}{d_i}v)$$
$$=e^{jkd_i+j\frac{k}{2d_i}[u^2+v^2]}e^{jkd_o+j\frac{k}{2d_o}\left(\frac{d_o}{d_i}\right)^2[u^2+v^2]}\times-\frac{d_o}{d_i}U_o\left(-\frac{d_o}{d_i}u,-\frac{d_o}{d_i}v\right)\equiv U_{i0}(u,v)$$

Geometric optics predicts $-\frac{d_o}{d_i}U_o(-\frac{d_o}{d_i}u,-\frac{d_o}{d_i}v)$. Fourier optics further predicts two additional quadratic phase terms. Let's denote the resulting field $U_{i0}(u,v)$.

In this example, we can imagine that under practical large aperture, P would not be away from δ functional. It is this δ functional that gets rid of the double integral.

2.4.2 Out-of-focus aberration and sufficiently large aperture

If the aperture is sufficiently large, same as no aperture, $p(x,y)=1$ everywhere. One the other hand, the out-of-focus aberration is characterized by Δ. Using the identity:

$$F\left\{e^{j\pi\lambda\Delta(\xi^2+\eta^2)}\right\}(x,y)=-\frac{1}{j\lambda\Delta}e^{-\frac{j\pi}{\lambda\Delta}(x^2+y^2)}=-\frac{1}{j\lambda\Delta}e^{-\frac{jk}{2\Delta}(x^2+y^2)}$$

Therefore,

$$P(x,y;u,v;d_o,d_i;\epsilon)=\frac{-1}{d_o d_i}F\left\{e^{j\pi\Delta\lambda(\xi^2+\eta^2)}\right\}\left(\frac{x}{d_o}+\frac{u}{d_i},\frac{y}{d_o}+\frac{v}{d_i}\right)$$
$$=-\frac{1}{j\lambda\Delta}e^{-\frac{j\pi}{\lambda\Delta}\left[\left(\frac{x}{d_o}+\frac{u}{d_i}\right)^2+\left(\frac{y}{d_o}+\frac{v}{d_i}\right)^2\right]}$$

Equ.(19) can be summarized in a convolution form:

$$U_i(u,v)=U_{i0}(u,v)\ **-\frac{1}{j\lambda\Delta \mathrm{d}_\mathrm{o}^2}e^{-\frac{j\pi}{\lambda\Delta \mathrm{d}_\mathrm{o}^2}\left[\left(-\frac{d_o}{d_i}u\right)^2+\left(-\frac{d_o}{d_i}v\right)^2\right]}$$

$**$ means 2D convolution. It can be seen that the out-of-focused image is the focused image convoluted with the out-of-focus kernel. It should be noted that in $U_{i0}(u,v)$, only $K\left(d_o;-\frac{d_o}{d_i}u,-\frac{d_o}{d_i}v\right)\times-\frac{d_o}{d_i}U_o(-\frac{d_o}{d_i}u,-\frac{d_o}{d_i}v)$ participates the convolution. $K(d_i;u,v)$ is a constant.

2.4.3 Fourier transform pair (in sufficiently large aperture)

If $d_i=d_o=f$, $U_i(u,v)=\frac{e^{j2kf}}{j\lambda f}F\{U_o(x,y)\}(\frac{u}{\lambda f},\frac{v}{\lambda f})$. Therefore, U_i and U_o can be seen as a Fourier transform pair. Equivalently, U_i is also resulting from Fraunhofer diffraction. One can find Equ.(16) gives a very similar form if dropping the quadratic phase terms, which is the condition of Fraunhofer approximation.

Besides, as a mathematical manipulation, one can proof that

$$F\{U(x,y)\}(f_x,f_y)=\frac{1}{a^2}F\left\{U\left(\frac{x}{a},\frac{y}{a}\right)\right\}\left(\frac{f_x}{a},\frac{f_y}{a}\right),\forall a\in R.$$

If choosing $=\frac{1}{\lambda f}$, $U_i(u,v)=-j\lambda f e^{j2kf}F\{U_o(\lambda f x,\lambda f y)\}(u,v)$.

2.4.4 4f configuration with sufficiently large aperture. Planar object in focus.

This is to cascade 2.4.3 twice.

$$U_i(\xi,\eta) = \frac{e^{j2kf}}{j\lambda f} F\left\{\frac{e^{j2kf}}{j\lambda f} F\{U_o(x,y)\}\left(\frac{u}{\lambda f},\frac{v}{\lambda f}\right)\right\}\left(\frac{\xi}{\lambda f},\frac{\eta}{\lambda f}\right)$$
$$= \frac{e^{j2kf}}{\underbrace{j\lambda f}_{cancel}} F\left\{-\underbrace{j\lambda f}\, e^{j2kf} F\{U_o(\lambda f x, \lambda f y)\}(u,v)\right\}\left(\frac{\xi}{\lambda f},\frac{\eta}{\lambda f}\right)$$
$$= e^{j4kf} \times -U_o(-\xi,-\eta)$$

Note that $F\{F\{U(x,y)\}\} = U(-x,-y)$

2.4.5 4f configuration with finite aperture. Planar object in focus

$$\boldsymbol{U_i(\xi,\eta) = -e^{j4kf} \iint_{x,y} dxdy U_o(x,y) F\{p(\lambda f u, \lambda f v)\}(x+\xi, y+\eta)}$$

One can see that if $p_\epsilon = 1\ everywhere$, $\boldsymbol{U_i(\xi,\eta)}$ degenerates to 2.4.4.

2.4.6 4f configuration with sufficiently large aperture. Planar object out-of-focus

Let $d_i = f$ and remain the freedom of d_o. The first lens transforms U_o into U_p:

$$U_p(u,v) = \frac{e^{jk(f+d_o)}}{j\lambda d_o} F\left\{U_o(x,y) e^{j\frac{\pi}{\lambda d_o}\left(1-\frac{f}{d_o}\right)(x^2+y^2)}\right\}\left(\frac{u}{\lambda d_o},\frac{v}{\lambda d_o}\right)$$
$$= -j\lambda d_o e^{jk(f+d_o)} F\left\{U_o(\lambda d_o x, \lambda d_o y) e^{j\pi\lambda d_o\left(1-\frac{f}{d_o}\right)(x^2+y^2)}\right\}(u,v)$$

U_p is the field where the aperture is going to be applied soon in 2.4.7.The second lens transforms U_p into U_i:

$$U_i(\xi,\eta) = \frac{e^{j2kf}}{j\lambda f} F\{U_p(u,v)\}\left(\frac{\xi}{\lambda f},\frac{\eta}{\lambda f}\right)$$
$$= e^{jk(3f+d_o)} \times -\frac{d_o}{f} U_o\left(-\frac{d_o}{f}\xi,-\frac{d_o}{f}\eta\right) e^{j\frac{\pi}{\lambda f}\left(\frac{d_o}{f}-1\right)(\xi^2+\eta^2)}$$

2.4.7 4f configuration with finite aperture. Planar object out-of-focus

Assume symmetric aperture, $P_\epsilon(u,v) = P_\epsilon(-u,-v)$. Note $F^{-1}\{F(A)F(B)\} = A ** B$. Apply a finite aperture $P_\epsilon(u,v)$ at $U_p(u,v)$ in 2.4.6,

$$U_i(\xi,\eta) = \frac{e^{j2kf}}{j\lambda f} F\{U_p(u,v)P_\epsilon(u,v)\}(\frac{\xi}{\lambda f},\frac{\eta}{\lambda f})$$
$$= e^{jk(3f+d_o)} \times -\frac{d_o}{f} U_o\left(-\frac{d_o}{f}\xi,-\frac{d_o}{f}\eta\right) e^{j\frac{\pi}{\lambda f}\left(\frac{d_o}{f}-1\right)(\xi^2+\eta^2)} ** F\{P_\epsilon(u,v)\}(\frac{\xi}{\lambda f},\frac{\eta}{\lambda f})$$

As can be seen, if $p_\epsilon = 1\ everywhere$, $F\{p_\epsilon\} = \delta$, 2.4.7 degenerates to 2.4.6. If $d_o = f$, 2.4.7 degenerates to 2.4.5.

2.4.8 Two point objects at different depths

On the other extreme, if $p(x,y) = \delta(\mathrm{x},\mathrm{y})$

Assume there are two point objects at different depths: $U_o = A_1\delta(x-x_1, y-y_1, z-d_1) + A_2\delta(x-x_2, y-y_2, z-d_2)$, and two different apertures are used: ϵ_1 and ϵ_2. We obtain

$$\begin{cases} \begin{pmatrix} U_{i1}(u,v) \\ U_{i2}(u,v) \end{pmatrix} = K(d_i;u,v) \begin{bmatrix} P_{11} & P_{12} \\ P_{21} & P_{22} \end{bmatrix} \begin{pmatrix} A_1K(d_1;u,v) \\ A_2K(d_2;u,v) \end{pmatrix} \\ P_{mn} = P(x_n,y_n;u,v;d_n,d_i;\epsilon_m) \end{cases}$$

Of course, one may use more than two apertures to solve the matrix equation. This result suggests that one can resolve $A_1K(d_1;u,v)$ and $A_2K(d_2;u,v)$ separately.

2.4.9 Useful formula

$$F\{P(\lambda x, \lambda y)\} = F\left\{circ\left(\frac{\lambda}{\epsilon} r\right)\right\} = \frac{\epsilon}{\lambda}\frac{J_1\left(2\pi\frac{\epsilon}{\lambda}s\right)}{s} \quad , s^2 = s_x^2 + s_y^2$$

$$jinc(x) = \frac{J_1(\pi x)}{2x}, jinc(0) = \frac{\pi}{4}$$

2.5 Conclusion

Common practice of using aperture is to choose a best size for purposes. A dilemma often follows: while reducing aperture decreases out-of-focus aberration (therefore increases resolution), it also reduces SNR. It should be possible to modulate PSF through changing aperture sizes. As a result, one can maintain high SNR as well as high resolution in tomographic imaging.

Bibliography

1. Yeatts, A.B. and J.P. Fisher, *Tubular perfusion system for the long-term dynamic culture of human mesenchymal stem cells.* Tissue Eng Part C Methods, 2011. **17**(3): p. 337-48.
2. Intes, X., et al., *In vivo continuous-wave optical breast imaging enhanced with Indocyanine Green.* Med Phys, 2003. **30**(6): p. 1039-47.
3. Pfefer, T.J., A. Agrawal, and R.A. Drezek, *Oblique-incidence illumination and collection for depth-selective fluorescence spectroscopy.* J Biomed Opt, 2005. **10**(4): p. 44016.
4. Chen, C.W. and Y. Chen, *Optimization of Design Parameters for Fluorescence Laminar Optical Tomography.* Journal of Innovative Optical Health Sciences, 2011. **4**(3): p. 309-323.
5. Chen, C.W., et al. *Three-dimensional imaging of stem cell distribution within tissue engineering scaffolds using angled fluorescent laminar optical tomography (aFLOT)*. in *Photonics Conference (PHO), 2011 IEEE*. 2011. IEEE.
6. Wang, L. and S.L. Jacques, *Use of a laser beam with an oblique angle of incidence to measure the reduced scattering coefficient of a turbid medium.* Appl Opt, 1995. **34**(13): p. 2362-6.
7. Chen, Y., et al., *Integrated Optical Coherence Tomography (OCT) and Fluorescence Laminar Optical Tomography (FLOT).* IEEE J. Selected Topics in Quantum Electronics 2010. **16**(4): p. 755-766.
8. Yuan, S., et al., *Three-dimensional coregistered optical coherence tomography and line-scanning fluorescence laminar optical tomography.* Opt Lett, 2009. **34**(11): p. 1615-7.
9. Tanbakuchi, A.A., A.R. Rouse, and A.F. Gmitro, *Monte Carlo characterization of parallelized fluorescence confocal systems imaging in turbid media.* J Biomed Opt, 2009. **14**(4): p. 044024.
10. Zhang, H.F., et al., *Functional photoacoustic microscopy for high-resolution and noninvasive in vivo imaging.* Nat Biotechnol, 2006. **24**(7): p. 848-51.
11. Vonesch, C., et al., *The colored revolution of bioimaging.* Signal processing magazine, IEEE, 2006. **23**(3): p. 20-31.
12. Deliolanis, N., et al., *Free-space fluorescence molecular tomography utilizing 360 degrees geometry projections.* Opt Lett, 2007. **32**(4): p. 382-4.
13. Bjorn, S., V. Ntziachristos, and R. Schulz, *Mesoscopic epifluorescence tomography: reconstruction of superficial and deep fluorescence in highly-scattering media.* Opt Express, 2010. **18**(8): p. 8422-9.
14. Dunn, A. and D. Boas, *Transport-based image reconstruction in turbid media with small source-detector separations.* Opt Lett, 2000. **25**(24): p. 1777-9.
15. Hillman, E.M., et al., *Laminar optical tomography: demonstration of millimeter-scale depth-resolved imaging in turbid media.* Opt Lett, 2004. **29**(14): p. 1650-2.
16. Yuan, B., et al., *A system for high-resolution depth-resolved optical imaging of fluorescence and absorption contrast.* Rev Sci Instrum, 2009. **80**(4): p. 043706.

17. Wang, Z.G., et al., *Fluorescence guided optical coherence tomography for the diagnosis of early bladder cancer in a rat model.* J Urol, 2005. **174**(6): p. 2376-81.
18. Hillman, E.M., et al., *Depth-resolved optical imaging of transmural electrical propagation in perfused heart.* Opt Express, 2007. **15**(26): p. 17827-41.
19. Thiel, E., *Introduction to Fluorescence Spectroscopy, A. Sharma and S. G. Schulman John Wiley & Sons, Chichester, 1999; price £38.95 173 pp.* Magnetic Resonance in Chemistry, 2001. **39**(5): p. 299-299.
20. Per Christian Hansen, J.G.N., Dianne P. O'Leary, *Deblurring images: matrices, spectra, and filtering*. 2006: SIAM.
21. Hansen, P.C. and D.P. O'Leary, *The use of the L-curve in the regularization of discrete ill-posed problems.* SIAM Journal on Scientific Computing, 1993. **14**(6): p. 1487-1503.
22. Huisken, J., et al., *Optical sectioning deep inside live embryos by selective plane illumination microscopy.* Science, 2004. **305**(5686): p. 1007-9.
23. Crilly, R.J., et al., *Forward-adjoint fluorescence model: Monte Carlo integration and experimental validation.* Appl Opt, 1997. **36**(25): p. 6513-9.
24. Fang, Q. and D.A. Boas, *Monte Carlo simulation of photon migration in 3D turbid media accelerated by graphics processing units.* Opt Express, 2009. **17**(22): p. 20178-90.
25. Boas, D., et al., *Three dimensional Monte Carlo code for photon migration through complex heterogeneous media including the adult human head.* Opt Express, 2002. **10**(3): p. 159-70.
26. Fang, Q., et al., *Combined optical imaging and mammography of the healthy breast: optical contrast derived from breast structure and compression.* IEEE Trans Med Imaging, 2009. **28**(1): p. 30-42.
27. Joshi, A., et al., *Radiative transport-based frequency-domain fluorescence tomography.* Phys Med Biol, 2008. **53**(8): p. 2069-88.
28. Stelzer, E.H.K. and S. Lindek, *Fundamental reduction of the observation volume in far-field light microscopy by detection orthogonal to the illumination axis: confocal theta microscopy.* Optics communications, 1994. **111**(5): p. 536-547.
29. Zhu, C.F., Q. Liu, and N. Ramanujam, *Effect of fiber optic probe geometry on depth-resolved fluorescence measurements from epithelial tissues: a Monte Carlo simulation.* Journal of Biomedical Optics, 2003. **8**(2): p. 237-247.
30. Pfefer, T.J., A. Agrawal, and R.A. Drezek, *Oblique-incidence illumination and collection for depth-selective fluorescence spectroscopy.* Journal of Biomedical Optics, 2005. **10**(4): p. 044016.
31. Nieman, L., et al., *Optical sectioning using a fiber probe with an angled illumination-collection geometry: evaluation in engineered tissue phantoms.* Applied Optics, 2004. **43**(6): p. 1308-1319.
32. Liu, Q. and N. Ramanujam, *Experimental proof of the feasibility of using an angled fiber-optic probe for depth-sensitive fluorescence spectroscopy of turbid media.* Opt Lett, 2004. **29**: p. 2034-2036.

33. Skala, M.C., et al., *Investigation of fiber-optic probe designs for optical spectroscopic diagnosis of epithelial pre-cancers.* Lasers in Surgery and Medicine, 2004. **34**(1): p. 25-38.
34. Dwyer, P.J., C.A. DiMarzio, and M. Rajadhyaksha, *Confocal theta line-scanning microscope for imaging human tissues.* Applied optics, 2007. **46**(10): p. 1843-1851.
35. Culver, J.P., et al., *Optimization of optode arrangements for diffuse optical tomography: A singular-value analysis.* Optics Letters, 2001. **26**(10): p. 701-703.
36. Graves, E.E., et al., *Singular-value analysis and optimization of experimental parameters in fluorescence molecular tomography.* Journal of the Optical Society of America a-Optics Image Science and Vision, 2004. **21**(2): p. 231-241.
37. Flock, S.T., et al., *Optical properties of Intralipid: a phantom medium for light propagation studies.* Lasers Surg Med, 1992. **12**(5): p. 510-9.
38. Chen, C.W., et al., *Macroporous Hydrogel Scaffolds and Their Characterization By Optical Coherence Tomography.* Tissue Eng Part C Methods, 2010. **17**(1): p. 101-112.
39. Agrawal, A., et al., *Three-dimensional characterization of optical coherence tomography point spread functions with a nanoparticle-embedded phantom.* Opt Lett, 2010. **35**(13): p. 2269-71.
40. Thevenot, P., et al., *Method to analyze three-dimensional cell distribution and infiltration in degradable scaffolds.* Tissue Eng Part C Methods, 2008. **14**(4): p. 319-31.
41. Yeatts, A.B., C.N. Gordon, and J.P. Fisher, *Formation of an aggregated alginate construct in a tubular perfusion system.* Tissue Eng Part C Methods, 2011. **17**(12): p. 1171-8.
42. Volkmer, E., et al., *Hypoxia in static and dynamic 3D culture systems for tissue engineering of bone.* Tissue Eng Part A, 2008. **14**(8): p. 1331-40.
43. Ueng, S.W., et al., *Development of a biodegradable alginate carrier system for antibiotics and bone cells.* J Orthop Res, 2007. **25**(1): p. 62-72.
44. Wang, L., et al., *Evaluation of sodium alginate for bone marrow cell tissue engineering.* Biomaterials, 2003. **24**(20): p. 3475-81.